Double Diffraction Dissociation at Large Momentum Transfer

Brian Cox

October 1998

THE UNIVERSITY
of MANCHESTER

High Energy Group
Department of Physics and Astronomy

A thesis submitted to The University of Manchester for the degree of
Doctor of Philosophy in the Faculty of Science and Engineering

Contents

Abstract

Photoproduction events which have two or more jets with transverse energy $E_T >$ 4.5 GeV have been studied in the γp centre of mass energy range 158 GeV $< W <$ 247 GeV with the H1 detector at HERA. The fraction $f(\Delta\eta)$ of events with a rapidity gap between the two highest E_T jets is measured as a function of the rapidity separation $\Delta\eta$ between the jet axes. A gap is defined as the absence between the jets of any particle with energy $E > 400$ MeV. The gap fraction is observed to fall exponentially up to $\Delta\eta < 3.5$. An excess of events with a large rapidity gap, over what would be expected from standard photoproduction processes, is observed for $\Delta\eta > 3.5$. The excess can be interpreted as the result of the exchange of a strongly interacting colour singlet object.

A new approach to the investigation of diffraction at high momentum transfer is presented in which the double dissociation process $\gamma p \to XY$ is studied. The systems X and Y are separated by the largest rapidity gap in the event with all particles on the photon side of the gap ascribed to the system X. It is shown that a measurement of the cross section $\mathrm{d}\sigma/\mathrm{d}x_{I\!P}$, where $x_{I\!P} = (M_X^2 - t)/W^2$, allows a direct determination of the energy dependence of the diffractive process, and hence provides a stringent test of theories of high $|t|$ diffraction.

The double dissociation photoproduction cross section for the process $\gamma p \to XY$ is measured for the first time at large 4-momentum transfer squared $|t| > 20\mathrm{GeV}^2$ using the H1 detector at HERA. Cross sections are measured differentially in $x_{I\!P}$, for $y_{I\!P} = (M_Y^2 - t)/W^2 < 0.018$. In the range $0.0007 < x_{I\!P} < 0.0040$, the shape of the measured $x_{I\!P}$ distribution is compared to predictions for standard photoproduction processes and to a model based on the exchange of a strongly interacting colour singlet object at large $|t|$.

No portion of the work referred to in this thesis has been submitted in support of an application for another degree or qualification of this or any other institute of learning.

This work was supported financially by the Particle Physics and Astronomy Research Council (P.P.A.R.C.) between October 1995 and October 1998.

Chapter 1

Introduction

Diffraction in electron-proton [1] scattering processes at HERA, and the closely related physics of the proton structure function at low x, provide a unique opportunity to study the transition from short to long distance physics. For almost 40 years, Regge theory has successfully parameterised our ignorance about the underlying dynamics of the strong interaction in long distance processes (i.e. the bulk of total hadronic cross sections). In contrast, perturbative QCD (pQCD), whilst outstandingly successful at describing short distance physics, has as yet been unable to "explain" Regge behaviour, as it must if it is to be regarded as the complete theory of the strong interaction. We are therefore faced with the unsatisfactory situation of having two theoretical frameworks, each describing the strong interaction in different kinematic regimes. Since in Regge phenomenology, the pomeron, which in modern language has come to mean any strongly interacting colour singlet object with vacuum quantum numbers, is the object responsible for the high energy behaviour of total hadronic cross sections, a natural first step towards a QCD understanding of Regge theory would seem to be a pQCD understanding of the pomeron.

[1] The HERA collider can run with either electrons or positrons. For the physics presented in this thesis, no distinction need be made between the two, and the lepton beam will be referred to as the electron beam.

The structure of this thesis is as follows; chapter 2 contains a description of the H1 detector at HERA, the world's first electron-proton collider, focusing on the detector components used in the measurements presented in chapters 4 and 6. In chapter 3 a review of the physics which motivated this thesis is presented, including an introduction to Regge theory, HERA kinematics, proton and photon structure, DGLAP and BFKL evolution and diffractive physics at HERA. Chapter 4 describes the observation of dijet events in photoproduction with a rapidity gap between the two jets, which is interpreted as evidence for colour singlet exchange at large momentum transfer, the first such observation at H1. Chapter 5 contains a new approach to the investigation of high momentum transfer diffractive events, and an investigation into the relationship between the cross section for such events measured at HERA and the underlying parton level dynamics of the scattering process within the leading logarithmic approximation of BFKL [2]. Chapter 6 contains the measurement at H1 of the double diffraction dissociation cross section in photoproduction suggested in chapter 5.

[2]This work was carried out in collaboration with J. Forshaw and has been published in Physics Letters B [1]

Chapter 2

The H1 Experiment at HERA

2.1 The HERA Accelerator

The HERA accelerator is the world's first electron-proton collider. Two storage rings, each of 6.3 km in circumference, contain an electron beam of 27.6 GeV and a proton beam of 820 GeV, which are brought into collision at 4 interaction points. The centre of mass energy in the ep collision is equivalent to a 50 TeV electron beam incident on a fixed target. Two multi-purpose detectors, H1 and ZEUS, are located at the North and South interaction points respectively. They both provide near-hermetic coverage, and are optimised to detect the scattered electron in the electron, or backward, direction, and high multiplicity hadronic final states in the proton, or forward, direction. Both detectors are asymmetric about the beam direction, since the final state is boosted along the proton direction due to the asymmetric beam energies. Two fixed target experiments, HERMES and HERA-B, are located in the East and West experimental halls respectively. HERMES uses the polarised HERA electron beam, in collision with a polarised hydrogen, deuterium or ^{3}He target to study the spin structure of the proton and neutron. HERA-B uses fixed wire targets in the proton beam as a 'B' factory, primarily to investigate CP violation in the B

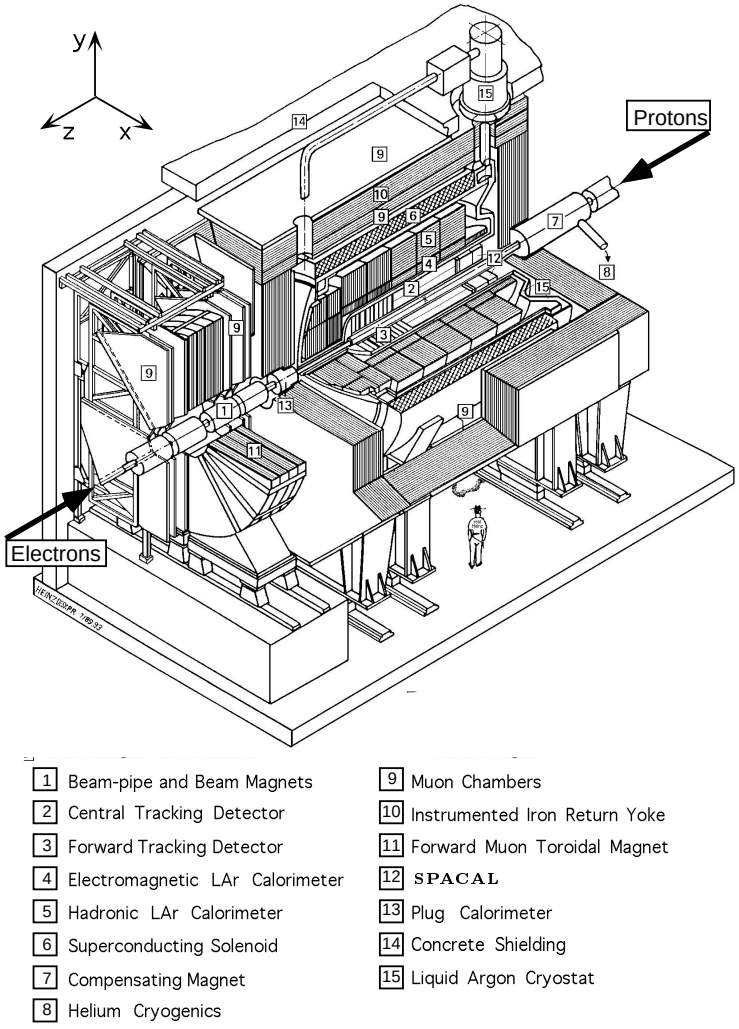

Figure 2.1: The H1 Detector

system through the process $B^0 \to \mathrm{J}/\psi K^0_S$.

2.2 Overview of the H1 Apparatus

The H1 apparatus [2] is shown in figure 2.1. The incoming proton beam defines the positive z direction in the right handed Cartesian coordinate system (x, y, z) [1]. A

[1]The z axis is defined with reference to the central tracker

spherical coordinate system (r, θ, ϕ) is defined such that $\theta = 180^0$ corresponds to the direction of the incoming electron beam. The H1 design philosophy is based on the precise measurement of the scattered electron and full containment of the hadronic final state. This is achieved by the near-hermetic coverage of the 4 main calorimeters, the Liquid Argon Calorimeter (LAr), the backward SPACAL calorimeter, the Plug and the Instrumented Iron, coupled with a tracking system in a 1.16 T magnet field. A multi-level triggering system is implemented to distinguish ep collision events from the very large background of beam gas and beam wall collisions.

2.3 Calorimetry

The analyses presented in this thesis use only the two main H1 calorimeters, the LAr and the SPACAL. They provide full coverage in the polar angle range $4^0 < \theta < 177.5^0$, corresponding to a laboratory pseudorapidity [2] coverage of $3.35 < \eta < -3.82$. The plug calorimeter closes the gap between the forward edge of the LAr and the beam pipe. It consists of nine 7.5 cm layers of copper absorbing plates, with eight sampling layers of silicon. The iron return yoke of the magnet is instrumented with limited streamer tubes to detect particles which are not absorbed in the main calorimeters. Its main function is the detection of muons.

2.3.1 The Liquid Argon Calorimeter

The Liquid Argon Calorimeter [3] covers the pseudorapidity range $3.35 < \eta < -1.43$. It is required to make energy measurements of the hadronic final state and to detect DIS electrons in the high Q^2 (≥ 100 GeV^2) range. It is divided into two components, an electromagnetic and hadronic section. Both are contained in a single cryostat to minimise the amount of dead material before the active sections of the calorimeters.

[2] pseudorapidity is defined as $\eta = -\frac{1}{2} \ln \left(\tan \frac{\theta}{2} \right)$

The electromagnetic section uses lead plates of thickness 2.4 mm to initiate showers, which are sandwiched in between layers of liquid argon of a similar thickness. Argon atoms are ionized by the particles in the shower, and the resulting charge is collected by rectangular cathode pads typically a few centimeters in size. The total thickness of the electromagnetic section varies from $\sim$ 30 radiation lengths in the forward direction to $\sim$ 20 radiation lengths in the backward region, reflecting the fact that higher energy particles are expected in the outgoing proton direction. The hadronic section has thicker absorbing plates of 16 mm stainless steel, reflecting the longer distance taken for hadronic showers to develop in a medium. The Liquid Argon cells are 5 mm thick. The total thickness varies from 8 interaction lengths in the forward region to 4.5 interaction lengths in the backward region.

The LAr has $\sim 45,000$ readout channels. This high degree of segmentation enables electronic noise to be eliminated by removing signals from isolated cells. This is crucial for the analysis in this thesis, which relies on the identification of rapidity gaps in the hadronic final state. The LAr is a non-compensating hadronic calorimeter. This results in losses at the 30% level in the measurement of hadrons, which are corrected using an energy dependent software re-weighting technique [4]. This technique uses the fine segmentation of the calorimeter to distinguish between electromagnetic and hadronic showers based on the details of the shower profiles. The e/π separation is less than 1 part in a thousand. From test beam measurements [3], the energy resolution of the electromagnetic section is $\frac{\sigma_E}{E} \simeq \frac{0.12}{\sqrt{E}} \oplus 0.01$ and the resolution of the hadronic section is $\frac{\sigma_E}{E} \simeq \frac{0.50}{\sqrt{E}} \oplus 0.02$ for charged pions, with E in GeV. The overall electromagnetic energy scale is determined by comparing tracking and energy measurements of the scattered electron in DIS, and is known to 3%. The hadronic energy scale is determined using p_T balance in DIS events, and is known to 4%.

2.3.2 The SPACAL Calorimeter

The SPACAL calorimeter [5] was installed during the HERA shutdown prior to the 1995 data taking period. It replaces the BEMC calorimeter, and is designed to provide much better hadronic measurements in the backward region, covering the pseudorapidity range $-1.43 < \eta < -3.82$, and to improve the energy measurement of the scattered electron. It is the introduction of this calorimeter which makes the rapidity gaps between jets analysis described in chapter 4 possible at H1. The backward region of the H1 detector is shown in figure 2.2. In common with the LAr, the SPACAL is divided into electromagnetic and hadronic sections. Both sections consist of scintillating fibres inserted into a lead matrix. The electromagnetic section has an active volume which is 250 mm deep, corresponding to 28 radiation lengths, and has 1192 readout channels. The hadronic section adds 1 interaction length to the electromagnetic section, which is itself 1 interaction length deep, and has 136 readout channels. Readout of the scintillation light is by photomultiplier tubes, which provide the 1 ns time resolution necessary for up-stream beam gas background rejection. (see section 2.8.3). From test beam measurements, the energy resolution of the electromagnetic section is $\frac{\sigma_E}{E} \simeq \frac{0.7}{\sqrt{E}} \oplus 0.01$ and the resolution of the hadronic section is $\frac{\sigma_E}{E} \simeq \frac{0.56}{\sqrt{E}} \oplus 0.03$ for hadrons and $\frac{\sigma_E}{E} \simeq \frac{0.13}{\sqrt{E}} \oplus 0.036$ for electrons with E in GeV.

2.4 Tracking

The H1 tracking system is a combination of four distinct components. The forward tracker [6] covers the region in polar angle $7^0 < \theta < 25^0$. It consists of three 'supermodules' comprising layers of multi-wire proportional chambers (MWPCs), transition radiators and radial and planar drift chambers. The central region, $15^0 < \theta < 165^0$, is covered by a combination of MWPCs and drift chambers collectively

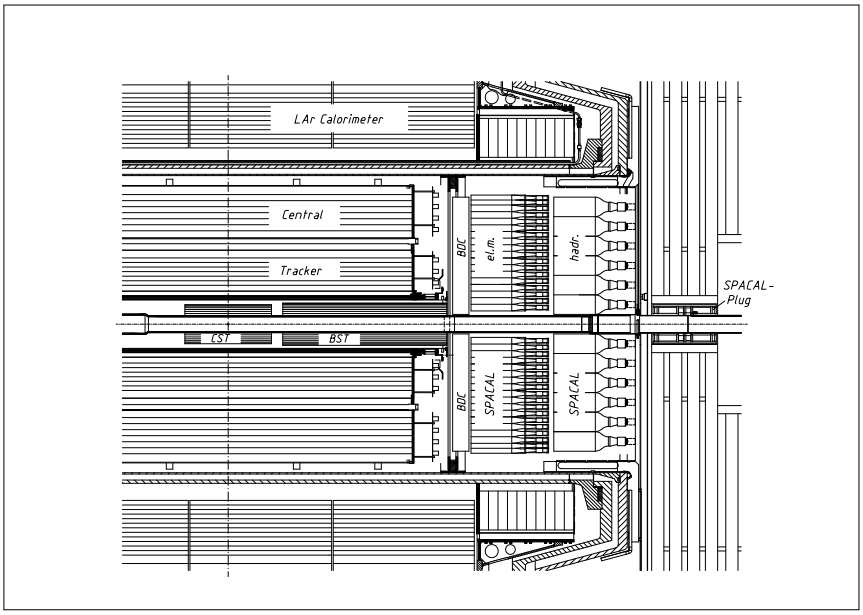

Figure 2.2: The backward region of H1, including the SPACAL and backward tracking detectors.

known as the central tracker. Charged particles in the backward region are detected in the backward drift chamber (BDC) attached to the front face of the SPACAL. Also installed during the 1995 shutdown were two silicon trackers, the CST and BST. The central and backward areas are shown in figure 2.2. Only the central tracker is used in the analyses presented in this thesis.

2.4.1 The Central Tracker

A cross section through the central tracker is shown in figure 2.3. The two large concentric drift chambers, CJC1 and CJC2 [7], form the bulk of the detector. A drift chamber consists of a number of individual gas filled cells, each containing a set of 'sense' wires (anodes), field wires (cathodes) and field shaping wires or plates, positioned such that the electric field is almost uniform across the cell. When a charged particles enters the cell, electrons produced in the ionisation of the gas drift

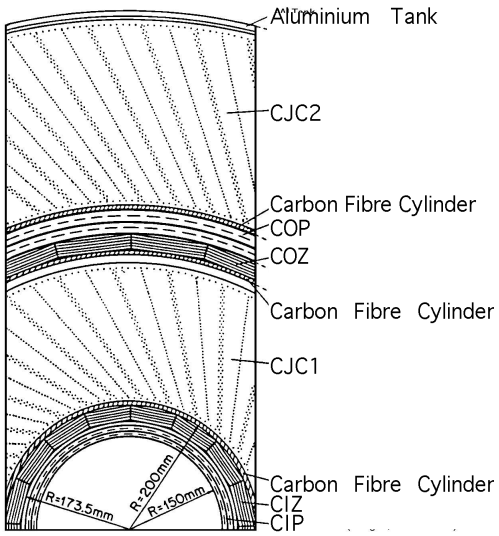

Figure 2.3: A section in the $r - \phi$ plane through the central tracking detector.

with a constant (known) velocity in the field towards the sense wires. When the electrons reach the vicinity (< 1 mm) of the sense wire the field strength increases rapidly, causing an avalanche of electrons and ions to be formed. The ions then move away from the sense wire, inducing a current in the wire which is recorded by the readout system. The time taken for the primary electrons to reach the sense wires is a simple function of the distance from the wire, allowing the distance of closest approach of the incident particle to each sense wire in the cell to be determined from the timing of the current pulses, usually to an accuracy of a few hundred μm. The difference in arrival time of the pulses at each end of a wire allows an estimate of the distance along the wire that the avalanche occurred, to an accuracy of a few cm. Together, both methods provide a series of points of closest approach to each sense wire in a chamber, allowing the path of the incident particle, or 'track', to be reconstructed. Because the central tracker is situated inside a high magnetic field, the charged particle tracks are bent into helical orbits. The curvature of the tracks allows the particles' momentum to be determined. Furthermore, the

amount of charge deposited in the chamber is related to the incident velocity of the particle, allowing particle identification in combination with the momentum measurement ($\mathrm{d}E/\mathrm{d}x$ measurement). The CJC cells are tilted at an angle of 30^0 from the radial direction, so that the drift direction for high momentum tracks is always close to being perpendicular to the track direction, improving the $r-\phi$ resolution of the trackers. The CJC chambers are therefore optimised to give precise $r-\phi$ measurements of a track, since this is given by the drift time, whilst the z coordinate must be derived from charge division measurements. In order to provide the best positional measurement in z, two smaller drift chambers, the Central Inner Z chamber (CIZ) and Central Outer Z chamber (COZ) [8], are used. These chambers have sense wires running perpendicular to the beam-pipe, and have drift field arranged such that the drift time provides the z measurement, whilst charge division gives the $r-\phi$ coordinate.

Whilst drift chambers provide accurate positional measurements of charged particle tracks, they do not deliver a signal fast enough for timing critical applications such as triggering. For this reason, another type of tracking chamber, the Multi Wire Proportional Chamber (MWPC) is employed. These chambers work on a similar principle to the drift chambers, except that there are no drift regions. Instead, the wires are placed very close together so that the avalanche regions overlap. This limits the spacial resolution to the wire separation distance, typically a few mm. In this type of chamber there is essentially no drift time, so readout is much faster. The central tracker has two MWPCs, CIP and COP [9], which are used principally for the z-vertex trigger, which will be described in section 2.8.1.

2.5 The Luminosity System

The H1 detector has three detectors placed at 8 m, 33 m and 44 m along the beam line in the outgoing electron direction, and a photon detector at 103 m. The

photon tagger and the 33 m electron tagger comprise the H1 luminosity system. The 33 m electron tagger is also used to measure the energy of low Q^2 electrons in photoproduction. The 8 m and 44 m taggers are not used in this thesis.

2.5.1 The Electron Tagger and the Photon Detector

The electron tagger is a crystal calorimeter made up of 49 units with a combined thickness of 22 radiation lengths. Electrons scattered at low angles are deflected into the tagger by the HERA beam magnets, and hence the acceptance is critically dependent on the HERA beam optics and the position of the interaction point, and varies from run to run.

The photon tagger is placed at the point where the beam lines begin to curve at $z = -103$ m. It consists of a lead filter to remove synchrotron radiation, a water Cerenkov detector and a 25 unit crystal calorimeter of the same design as the electron tagger, also covering 22 radiation lengths.

2.5.2 The Luminosity Measurement

The luminosity is calculated from the measured rate of the process $ep \to ep\gamma$, which, in the small angle approximation, is calculable within QED (the Bethe-Heitler formula [10]) and is known with a theoretical uncertainty of $\sim 0.5\%$. On-line, the measurement is made by counting events with coincidence signals in the electron and photon taggers. A relatively pure bremsstrahlung signal can be achieved by requiring that the energies of the detected photon and electron lie within $\sim$ 3 GeV of the electron beam energy. A more accurate off-line procedure involves corrections for bremsstrahlung of electrons off beam gas particles using pilot bunch information. Pilot bunches are non-colliding proton and electron bunches; any event which originates from such a non-colliding bunch must be a background event and

hence the overall background rate can be estimated. The error on the luminosity determined by this method is $\sim 4\%$, which comes mainly from the uncertainty in the electron tagger acceptance due to the beam optics. To avoid these complications, a further method based solely on the detection of photons is also used. The average luminosity is then given by

$$\mathcal{L} = \frac{\mathcal{N}_{data}(\Delta t) - \mathcal{N}_{back}(\Delta t)}{\mathcal{A}_{BH}\Delta t} \tag{2.1}$$

where $\mathcal{A}_{BH}$ is the acceptance for the Bethe-Heitler process of the particular method used, calculated from a detailed Monte Carlo simulation of the detectors and HERA beam optics, $\mathcal{N}_{data}(\Delta t)$ is the number of detected events in a time interval Δt, and $\mathcal{N}_{back}$ is the number of background events estimated from the pilot bunch information as described above.

2.6 Scintillation Detectors

The main veto for beam gas and beam wall interactions is provided by the Time Of Flight system (TOF) [11]. This consists of a layer of scintillation detectors, used because of their good time resolution, placed between the SPACAL and backward iron endcap, (backward TOF) and next to the forward muon toroid (forward TOF). Particles produced from an ep collision will arrive at the scintillators at different times to particles produced up-stream or down-stream from beam-gas or beam-wall interactions. This system results in a reduction of $\sim 99\%$ in the background rate.

A further set of scintillators, the 'Veto Wall' is situated backward of the iron return yoke. It is used primarily to veto 'beam-halo muons', which arrive with the proton beam.

In the forward direction, at $z = 26$ m, the proton remnant tagger (PRT) surrounds the beam pipe. It is a two layer scintillation device, surrounded by lead shielding. It can detect particles resulting from proton fragmentation at pseudo-

rapidities in the range $6 \leq \eta \leq 8$, and is used mainly for low momentum transfer diffractive analyses.

2.7 Muon Detectors

H1 is surrounded by limited streamer tubes situated within the iron return yoke, whose purpose is to detect muons which pass through the inner detectors. In the forward direction, further coverage is provided by the forward muon detector, consisting of drift chambers and a toroidal magnet. The toroidal field improves the momentum resolution of muons at low polar angles, which have little transverse motion with respect to the field lines in the main solenoidal field of H1. The forward muon detector [12] has been used not only to detect muons, but also as a method of tagging proton dissociation products at very large positive rapidities [13]. As such it has become an integral part of all low t diffractive measurements at H1.

2.8 Triggering and Readout

The HERA beams are split into short segments or 'bunches' which cross at the interaction points every 96 ns (This corresponds to a bunch separation of 28.8 m). This time interval is far shorter than the typical readout time of H1 detector components, which is $\sim 1\mu$s. Furthermore, for each event there are $270,000$ channels to be read out and stored. The solution employed at H1 is to implement a pipelined trigger and readout system, shown schematically in figure 2.4.

Each of the major H1 detector components has a trigger system which typically provide an 8-bit 'trigger element' to the central trigger (CTL1) [14] at each bunch crossing. There are approximately 200 trigger elements currently sent to CTL1. CTL1 must make a decision on whether to readout an event within $\sim$ 24 bunch

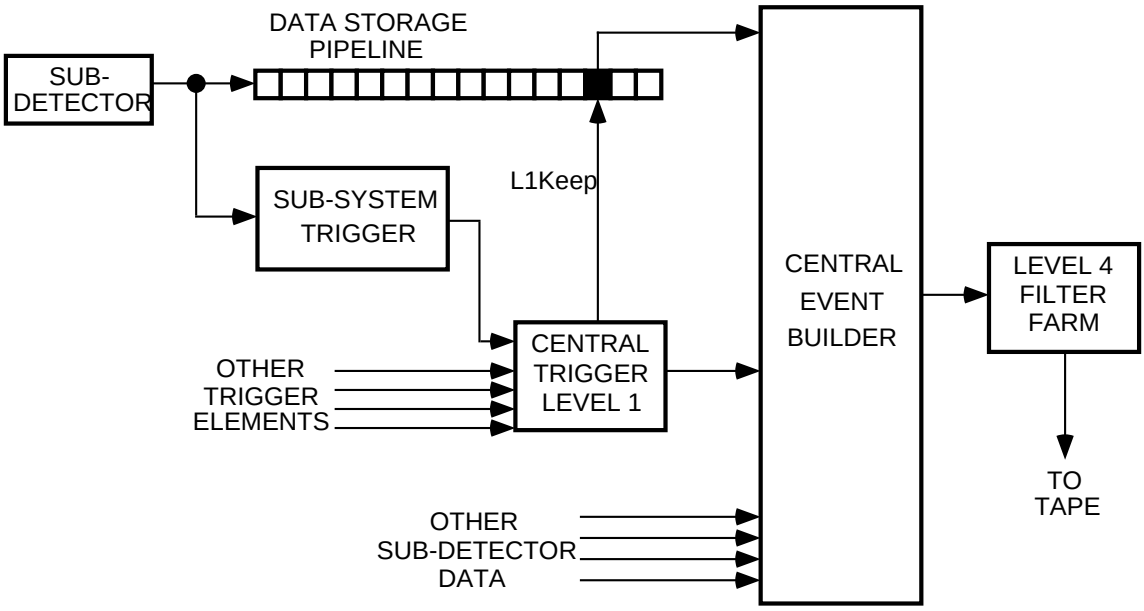

Figure 2.4: The H1 trigger and readout system

crossings, and the data from all 270,000 channels must therefore be stored in the pipeline for at least this long. The CTL1 decision is based on combinations of trigger elements known as 'subtriggers'. If a particular subtrigger condition is satisfied, the event may be read out, or, if the subtrigger has a particularly high rate, a counter is incremented and only a certain fraction of the events are read out (the subtrigger is then said to be 'prescaled'). If CTL1 decides to keep an event, an L1-keep signal is sent which freezes all pipelines, and the data from each detector is sent to the Central Event Builder (CEB). During this process, which extends for ~ 2 ms, H1 misses any further *ep* events that may occur, and this period is known as 'dead time'. CTL1 manages to reduce a background rate of ~ 10 kHz to an event rate of ~ 40 Hz by this procedure. The CEB pieces together the information from each detector component, and passes the data to the Level 4 filter farm for detailed processing. Level 4 rejects the overwhelming majority of background events remaining, reducing the event rate to approximately 5-10 Hz. Events passing Level 4 are written to tape. Each event is around 120 kBytes in size. A further off-line processing procedure,

known as Level 5, reduces the data available for physics analysis still further, based on stricter conditions than those applied at Level 4.

The trigger elements used in this thesis will be described in detail in the following three sections.

2.8.1 The z-Vertex Trigger

The most efficient method of rejecting non-ep background is to require a vertex in the interaction region. The MWPCs of the CIP and COP, plus a further MWPC mounted in the first supermodule of the forward tracker, are used for the fast track reconstruction necessary to provide a level one trigger element. Hits in any two of the three MWPCs are used to define 'rays' which are extrapolated in a straight line to r=0. The detector is divided into 16 segments in ϕ, which are further divided into 16 bins of 5.4 cm in z about the nominal interaction point. The number of rays which fall into each bin is entered into a histogram, and the ϕ histograms are combined into a single histogram. This process is shown schematically in figure 2.5 for one ϕ segment. For a genuine ep event, the resulting histogram will contain a peak at the true z-vertex position, and a lower background from mis-identified rays. If there is at least one entry in the histogram, the $T0$ trigger bit is set. This bit is used by most subtriggers for bunch crossing identification. On-line peak significance analysis provides stricter z-vertex requirements, which are combined to form the z-vertex subtrigger used in the double dissociation cross section analysis of Chapter 6.

2.8.2 The DCRΦ Trigger

The DCRΦ ($DCRPh$) trigger is a track based trigger, using drift time data from CJC1 and CJC2. In order to achieve dead-time free operation, track reconstruction is based on ten thousand look-up tables which relate the drift time data to the

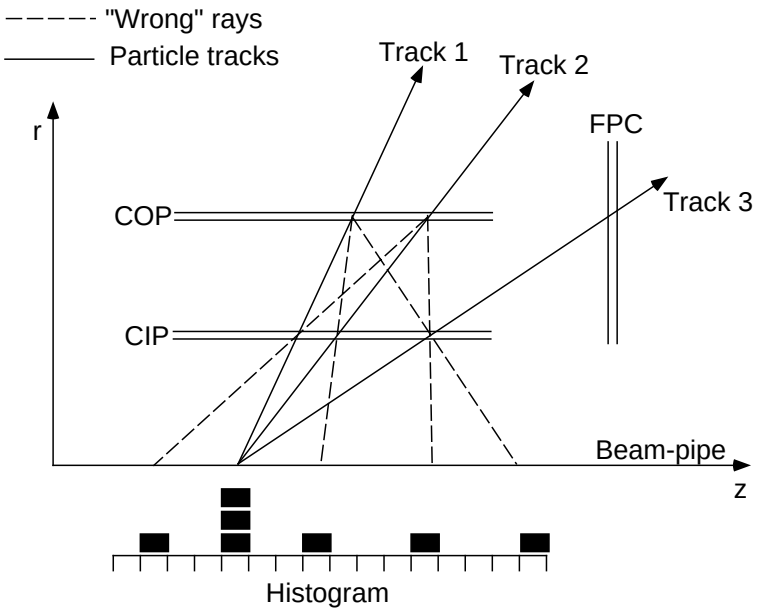

Figure 2.5: A schematic representation of the z-vertex trigger element for a single ϕ segment

momentum and position of tracks [3]. The DCRΦ trigger provides several trigger elements, each with different tracking requirements and timing information from the $T0$ bit, based on the number of reconstructed tracks and the sign of the charge of the tracks.

2.8.3 The SPACAL Inclusive Electron Trigger

The SPACAL Inclusive electron trigger ($SPCLe$) requires an energy deposit in the electromagnetic SPACAL within the 'Time Of Flight' window for an ep interaction. A series of trigger elements are sent to CTL1, each with different E_T thresholds, energy cluster positions and timing requirements.

[3]Note that the drift time is sufficiently small in the CJC that dead time free operation of the trigger can be achieved.

Chapter 3

Diffraction and Low x Physics at HERA

3.1 Regge Theory

Regge theory was developed in the late 1950's when no fundamental understanding of the underlying dynamics of the strong interaction was available. It is based solely on some very general assumptions about the scattering process, and should hold irrespective of the nature of the underlying dynamical theory. For this reason, Regge theory has rightly been called one of the great truths of particle physics [15], and its predictions must act as a constraint on the high energy properties of QCD [16].

3.1.1 The S-Matrix

In the real world, interactions at the microscopic level are never observed. The experimentalist only has (usually two) non-interacting beam particles at the beginning of a scattering experiment, and any number of non-interacting final state particles in the detector a macroscopically long time and distance after the interaction has

taken place. S-Matrix theory is concerned only with these 'observable' states, and the properties of the transition matrix elements between them. It has nothing to say about the details of the interaction itself, and this is the reason why Regge theory, which evolves from this approach, does not 'know' or need to know about the underlying dynamics.

The S matrix is defined as the matrix whose ab^{th} element is

$$S_{ab} = \langle b_{out} | a_{in} \rangle \tag{3.1}$$

where $|a_{in}\rangle$ is the free particle state, or 'in' state, as time $\rightarrow -\infty$, i.e. well before the interaction, and $|b_{out}\rangle$ is the free particle state, or 'out' state, as time $\rightarrow +\infty$, i.e. well after the interaction. It is related to the more familiar scattering amplitude (as calculated for example in pQCD) by

$$S_{ab} = \delta_{ab} + i(2\pi)^4 \delta^4(\sum_a p_a - \sum_b p_b) A_{ab} \tag{3.2}$$

where δ_{ab} represents the 'nothing happened' case and the i multiplying the 4-momentum conserving delta function is just convention. The scattering amplitude A_{ab} is usually written as a function of the Mandelstam variables s, t, and u, which in the case of 2-particle to 2-particle scattering,

$$a + b \rightarrow c + d, \tag{3.3}$$

are defined by

$$s = (p_a + p_b)^2 \quad t = (p_a - p_c)^2 \quad u = (p_a - p_d)^2 \tag{3.4}$$

where s is the square of the total centre of mass energy of the system and t is the square of the four-momentum transfer between particles a and c. In fact, conservation of momentum means that u is not an independent variable, and so (neglecting the particle masses) the scattering amplitude can be written as $A(s,t)$. This amounts to the reasonable assumption that the S matrix is Lorentz invariant.

3.1.2 The Unitarity of the S-Matrix and the Optical Theorem

Since the S Matrix connects the complete set of all physical states, it must be unitary:

$$SS^{\dagger} = S^{\dagger}S = I. \tag{3.5}$$

This is simply a statement of conservation of probability, i.e. the probability for an in-state to end up in a particular out-state, summed over all possible out-states, must be unity. Applying equation (3.5) to equation (3.2), and imposing time reversal symmetry, leads immediately to a relationship between the imaginary part of an amplitude and the scattering amplitudes of the incoming and outgoing states into all possible intermediate states:

$$2\Im m A_{ab} = (2\pi)^4 \delta^4 (\sum_a p_a - \sum_b p_b) \sum_c A_{ac} A^{\dagger}_{cb}. \tag{3.6}$$

This result, known as the Cutkosky rules [17], has an important special case, the Optical Theorem. Applying equation (3.6) to the forward elastic scattering amplitude $A_{aa}(s, t = 0)$,

$$2\Im m A_{aa}(s, 0) \propto \sum_n |A_{a \to n}|^2 = F \sigma_{tot} \tag{3.7}$$

where F is a flux factor, which is $\simeq 2s$ for $s \gg$ the masses in the process. The meaning of this result will be discussed in the context of HERA physics in section 3.1.6.

3.1.3 Crossing Symmetry

The aim of Regge theory is to isolate the high energy behaviour of the scattering amplitude $A(s, t)$ in the 'Regge limit', $s \to \infty$, $s \gg |t|$. In order to do this, a further assumption about the amplitudes must be made; that they are analytic functions

of the Mandelstam variables (regarded as complex variables) s, t and u [1]. This assumption leads to a powerful property of the amplitudes; crossing symmetry.

Consider the scattering process of equation (3.3). The scattering amplitude for this process can be written as $A_{ab\to cd}(s,t)$ where, in the physical kinematic region $s > 0$ and $t < 0$ (as should be clear from equation (3.4)). This is known as the s-channel process. The amplitude $A(s,t)$ can now be analytically continued into the unphysical region $t > 0$, $s < 0$. This is, however, the physical region for the 'crossed' t-channel process

$$a + \bar{c} \to \bar{b} + d \tag{3.8}$$

where $\bar{b}$ and $\bar{c}$ are the antiparticles of b and c respectively (again, this is clear from equation (3.4)). In other words, particles c and b have swapped places and been exchanged for their anti-particles and s and t have been interchanged. By crossing symmetry, these two very different physical processes will have the same scattering amplitude (and therefore physical cross section):

$$A(s,t) = A_{ab\to cd}(s,t), \qquad s > 0, \;\; t < 0 \tag{3.9}$$

$$A(s,t) = A_{a\bar{c}\to\bar{b}d}(t,s), \qquad s < 0, \;\; t > 0 \tag{3.10}$$

As an example, consider the case of pion - nucleon scattering shown in figure 3.1. If the resonance production process $\pi^-\pi^0 \to \bar{p}n$ is considered as the s-channel process, then by crossing symmetry the scattering process $\pi^- p \to \pi^0 n$ is described by the same amplitude.

3.1.4 The Scattering Amplitude in the Regge Limit

As mentioned in the previous section, crossing symmetry allows the high energy behaviour of the scattering amplitude to be isolated. A brief overview of this remarkable result will be given here. More detail can be found in the literature [15].

[1] It can be shown that this assumption is in fact a consequence of causality [15]

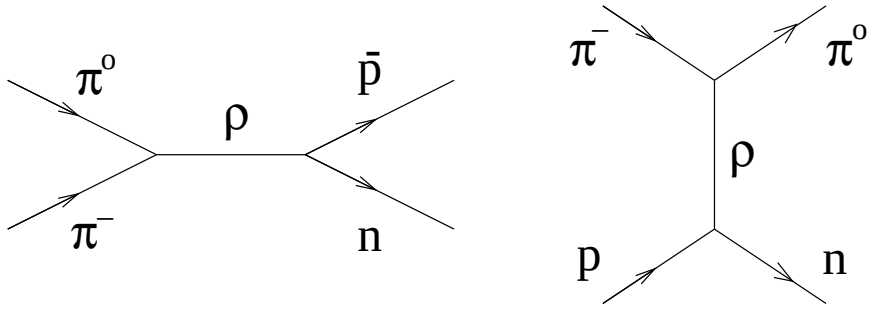

Figure 3.1: Pion - nucleon scattering

Consider the scattering process $a + \bar{c} \to \bar{b} + d$. In the physical region, i.e. $s > 0$, $t < 0$, the scattering amplitude can be expanded as a series in Legendre polynomials $P_l(\cos\theta)$ where θ is the centre of mass frame scattering angle, related to s and t by $\cos\theta = 1 + \frac{2t}{s}$;

$$A(s,t) = \sum_{l=0}^{\infty}(2l+1)a_l(s)P_l(1+\frac{2t}{s}) \tag{3.11}$$

The expansion coefficients $a_l(s)$ are known as the partial wave amplitudes. Crossing symmetry allows an analytic continuation into the unphysical region (which is the physical region for the crossed process $a + b \to c + d$);

$$A(s,t) = \sum_{l=0}^{\infty}(2l+1)a_l(t)P_l(1+\frac{2s}{t}) \tag{3.12}$$

The next step is a purely mathematical one, known as the Sommerfeld-Watson transformation [18]. The sum in the above equations is rewritten as a contour integral in the complex l plane;

$$A(s,t) = \frac{(-1)^l}{2i}\oint_C \mathrm{d}l(2l+1)\frac{a(l,t)}{sin\pi l}P(l,1+\frac{2s}{t}) \tag{3.13}$$

where the contour C is shown in figure 3.2. The Legendre polynomials and the partial wave amplitudes have each been analytically continued in l, giving the analytic functions $P(l,z)$ and $a(l,z)$ respectively. It should be clear that equations (3.13) and (3.12) are equivalent. The integral around C only picks up contributions from

the poles on the real l axis, that is for integral values of l, and the discrete sum of equation (3.12) is recovered. The contour C may now be deformed to the contour C' which runs parallel to the imaginary axis, shown in figure 3.2 [2]. In doing this, the residue of any poles that the functions $a(l,z)$ may have in the complex l plane, labelled as α_n in figure 3.2 are picked up, and equation (3.13) becomes [3]

$$A(s,t) = \frac{1}{2i}\int_{-\frac{1}{2}-i\infty}^{-\frac{1}{2}+i\infty} \mathrm{d}l \left[\frac{2l+1}{\sin\pi l} a(l,t) P(l, 1+\frac{2s}{t})\right] + \sum_n \frac{\tilde{\beta}_n(t)}{\sin\pi\alpha_n(t)} P\left(\alpha_n(t), 1+\frac{2s}{t}\right) \tag{3.14}$$

where the simple poles $\alpha_n(t)$ are the Regge Poles and $\tilde{\beta}_n(t)$ are the residues of the poles multiplied by $\pi(2\alpha_n(t)+1)$.

Now recall the physical motivation behind this mathematical manipulation. The behaviour of the scattering amplitude in the 'Regge region' $s \to \infty$, $s \gg |t|$ is the goal. In this limit, the Legendre polynomials are dominated by their leading terms:

$$P_l\left(1+\frac{2s}{t}\right) \to \left(\frac{s}{2t}\right)^l \tag{3.15}$$

and so the contribution from the integral along the contour C' vanishes and it is necessary only to consider the contribution from the Regge pole with the largest value of the real part of $\alpha_n(t)$, i.e. the Regge pole furthest to the right in figure 3.2. Equation (3.14) in the Regge limit therefore reduces to

$$A(s,t) \to \beta(t) s^{\alpha(t)}. \tag{3.16}$$

This expression is the heart of Regge phenomenology. Its meaning is the following; consider again the scattering process $a + \bar{c} \to \bar{b} + d$, shown in figure 3.3. The amplitude can be viewed as the exchange of an object of 'angular momentum' $\alpha(t)$. This object is known as a reggeon. It is, of course, not a particle in the usual sense, since it does not have integer or half integer angular momentum (and its 'angular

[2] It may be shown that the contribution from the semi-circular arc at infinity can be neglected.

[3] In order to simplify matters, the signature factors have been omitted from the above equations. This is a technical issue related to the uniqueness of the functions $a(l,t)$. For a full derivation see for example [19]. The possibility of the presence of cuts in the l plane has also been neglected.

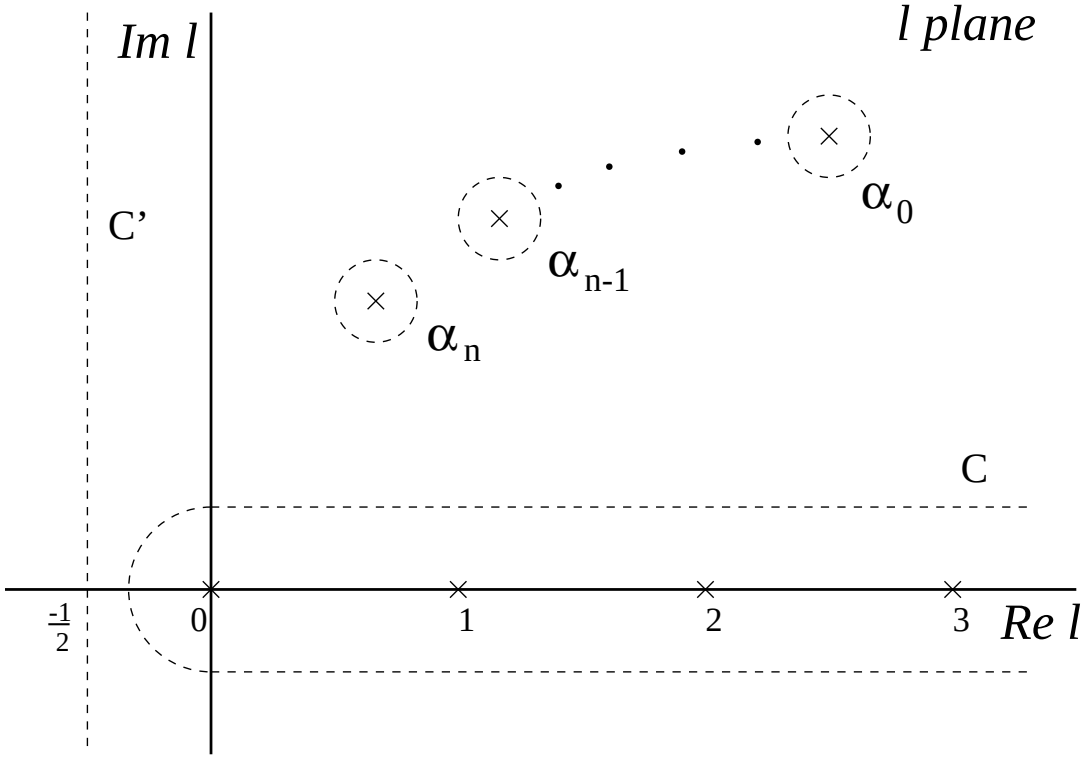

Figure 3.2: The complex angular momentum plane

momentum' is a function of t). The amplitude is more like a superposition of all possible amplitudes, that is the exchanges of all particles with the correct quantum numbers, for a particular scattering process.

3.1.5 Regge Trajectories

The predictive power of the Regge approach is realised only when the above mathematical result is coupled with a startling experimental one. Consider again the process $\pi^- p \to \pi^0 n$ shown in figure 3.1. For t positive, i.e. $\pi^- \pi^o \to \bar{p} n$, the amplitude will have poles corresponding to the production of physical particles, in this case the family of mesons with the quantum numbers of the ρ, i.e. the ω, f_2 etc, of spin J_i and mass m_i, where $\alpha(m_i^2) = J_i$. Chew & Frautschi [20] plotted the spins of these mesons against their squared masses. Their famous plot is shown in figure 3.4.

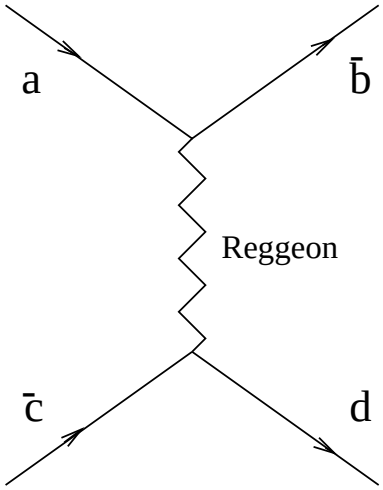

Figure 3.3: The t channel scattering process, viewed as the exchange of a reggeon

The mesons are seen to lie on a straight line. That is, at least for t positive,

$$\alpha(t) = \alpha(0) + \alpha' t \tag{3.17}$$

From figure 3.4, $\alpha(0) = 0.55$ and $\alpha' = 0.86$ GeV^2. The prediction from Regge Theory is that the amplitude for the crossed process $\pi^- p \to \pi^0 n$, using equations (3.17) and (3.16) should be

$$A(s,t) \simeq s^{(\alpha(0)+\alpha' t)} \tag{3.18}$$

and hence, since

$$\frac{\mathrm{d}\sigma}{\mathrm{d}t} \simeq \frac{|A(s,t)|^2}{s^2} \tag{3.19}$$

$$\frac{\mathrm{d}\sigma}{\mathrm{d}t} \simeq s^{2\alpha(0)+2\alpha' t-2} \tag{3.20}$$

The experimental data, taken in the pion energy range $20.8 - 199.3$ GeV [21] are shown in figure 3.5. The Regge prediction is shown as the solid line, and is seen to describe the data well over the measured energy range.

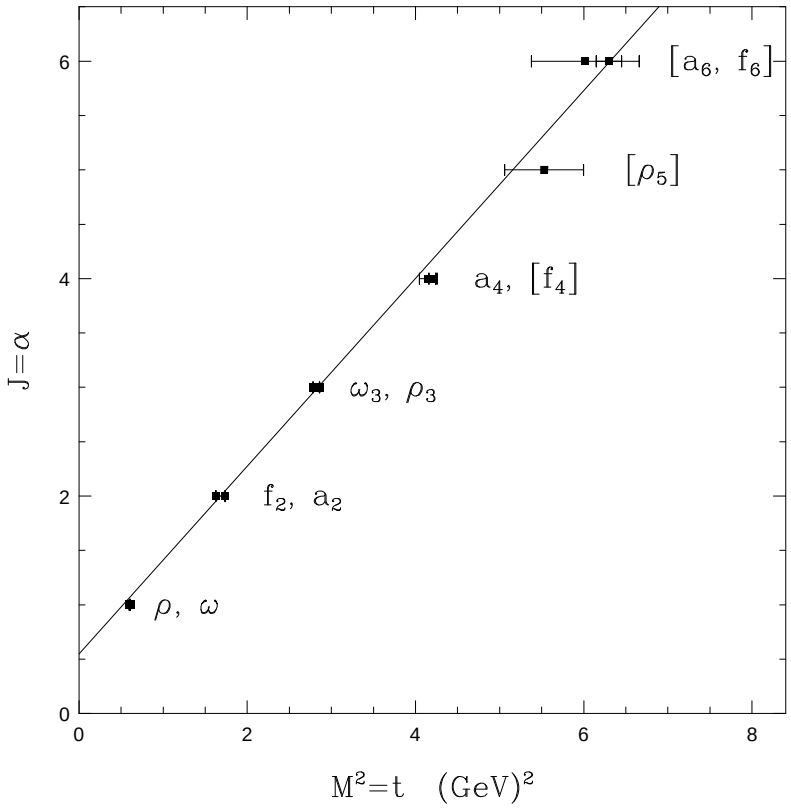

Figure 3.4: The Chew-Frautschi plot

3.1.6 The Optical Theorem and Total Cross Sections

The true predictive power of the Regge approach becomes apparent when it is coupled with the Optical Theorem. Recall equation (3.7)

$$\frac{\Im m A(s,0)}{s} = \sigma_{tot}. \tag{3.21}$$

The prediction from Regge theory for the total cross section is therefore, from equations (3.18) and (3.21),

$$\sigma_{tot} \simeq s^{\alpha(0)-1}, \tag{3.22}$$

where $\alpha(0)$ is the intercept of the appropriate Regge trajectory, that is the trajectory which involves the exchange of the correct quantum numbers. So, for example, for

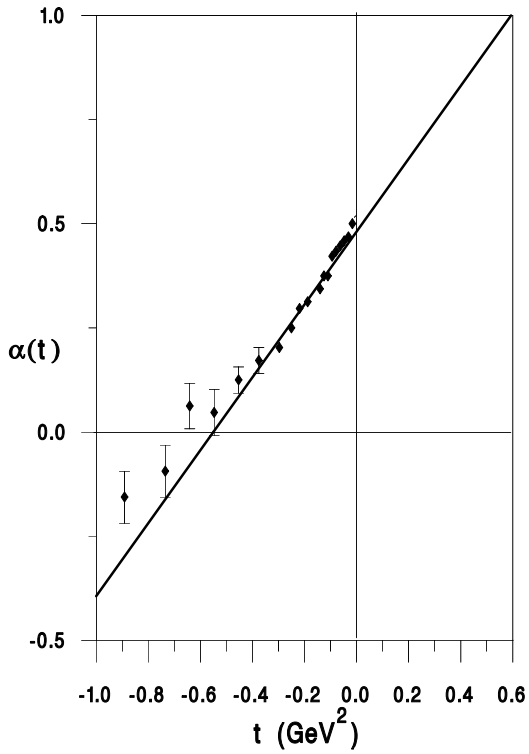

Figure 3.5: $\alpha(t)$ obtained from $\pi^- p \to \pi^o n$ scattering data [21]. The straight line is obtained by extrapolating the Regge trajectory of 3.4 using equation 3.20

processes which involve the ρ trajectory described in the previous section, σ_{tot} will fall as $s^{-0.45}$. In fact, in 1956, Pomeranchuk and Okun proved that for any scattering process in which there is charge exchange, σ_{tot} vanishes as $s \to \infty$ [22]. This result is known as the Pomeranchuk Theorem. In 1963 Foldy & Peierls applied this logic in reverse [23], and showed that any scattering process for which σ_{tot} does not vanish as $s \to \infty$ must be dominated by the exchange of vacuum quantum numbers. That is to say, this process involves the exchange of a Regge trajectory with intercept $\alpha(0) \geq 1$. Although no physical bound states are known which would lie on such a trajectory, it is an experimental fact that all total cross sections rise slowly with

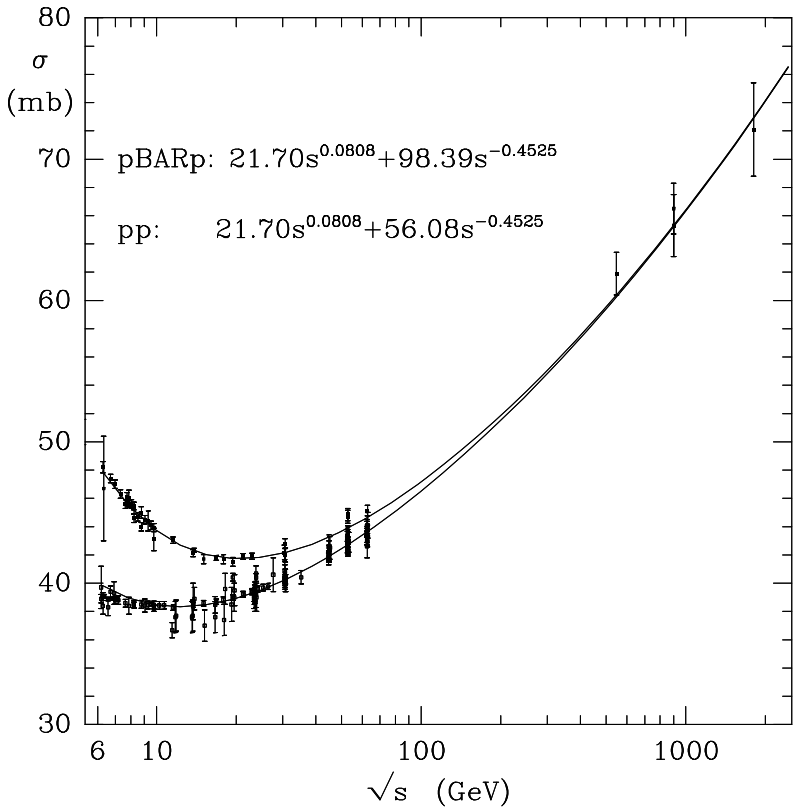

Figure 3.6: The proton-proton and proton-antiproton total cross sections, together with Regge fits by Donnachie & Landshoff

increasing s at todays energies. This trajectory is called the pomeron, after its inventor Pomeranchuk [24]. Figure 3.6 shows the total proton-proton and proton-antiproton cross sections, together with a fit by Donnachie and Landshoff [25] using two trajectories. The first term in the fits is the pomeron contribution, with intercept 1.08. This term is common to both cross sections, as it should be since the pomeron carries vacuum quantum numbers and is therefore unable to distinguish between particles and anti-particles. The second term is the contribution of the ρ trajectory, of intercept 0.55, described in section 3.1.5. This trajectory can of course have different couplings to particles and anti-particles. The difference between the two

fits vanishes at high energy, as expected from the Pomeranchuk theorem. It should be noted that these fits were made before the highest three points were measured at the Tevatron collider.

3.2 Dynamics at Different Scales

The HERA experiments revitalised the field of diffraction, and began the study of proton structure at low x, when they started taking data in 1992. The two closely related subjects will be discussed in the following sections, beginning with proton structure and scaling violations. The idea of investigating the pomeron structure in 'DIS off the pomeron', unique to HERA, is presented in section 3.5. In both cases, the virtuality of the photon provides a hard scale which delineates the boundary between Regge phenomenology and QCD; as the photon becomes more off-shell, the energy dependence of the cross sections is observed to steepen, which may be interpreted as a steady rise in an 'effective pomeron intercept'. The word 'effective' should be stressed here. A simple pole in the complex l plane cannot give rise to a trajectory which varies with Q^2, or any other scale. The experimental fact that the pomeron trajectory appears to vary with Q^2 signals that a more complex singularity structure is present. This evolution of the parameters of the effective pomeron trajectory is also observed in diffractive vector meson production, where the meson mass enters as a further scale. This is discussed in section 3.6.1. The remaining hard scale is the momentum transfer across the rapidity gap, the investigation of which is the subject of this thesis.

3.3 HERA Kinematics

Figure 3.7 defines the kinematics of the generic neutral current (NC) HERA scattering process $ep \to eX$, where X represents the hadronic final state, i.e. anything.

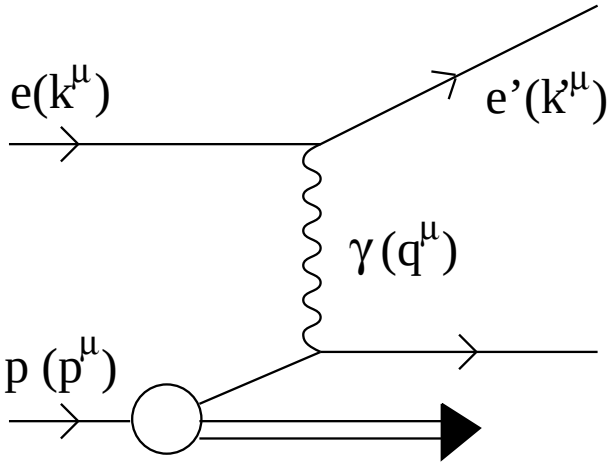

Figure 3.7: The neutral current DIS scattering process via photon exchange.

The square of the 4-momentum transfer Q^2 (i.e. the virtuality of the exchanged photon) [4] is

$$Q^2 = -q^2 = -\left(k - k^{'}\right)^2 \tag{3.23}$$

The ep centre of mass energy,

$$s = (k + p)^2 \tag{3.24}$$

is 90200GeV^2 for the 1996 running period, when HERA collided 27.6 GeV positrons and 820 GeV protons. The dimensionless Bjorken scaling variable x is defined as

$$x = \frac{Q^2}{2p.q} \tag{3.25}$$

and can be interpreted as the fraction of the protons' momentum carried by the struck parton in the limit that the parton is massless and carries no transverse momentum (this statement is explained further in section 3.4). A second scaling variable, y, which in the target rest frame is the fraction of the electron energy taken by the exchanged photon, is given by

$$y = \frac{p.q}{p.k}. \tag{3.26}$$

[4] In all but the very highest accessible Q^2 range at HERA, the exchanged electroweak boson is a photon, and Z^0 and W exchange can be neglected.

The invariant mass of the hadronic final state W is

$$W^2 = (q+p)^2 \tag{3.27}$$

Neglecting the masses of the incoming beam particles, the above kinematic variables are related by

$$Q^2 = sxy \tag{3.28}$$

$$W^2 = Q^2\left(\frac{1-x}{x}\right). \tag{3.29}$$

3.4 The Proton Structure Function

The cross section for the process $ep \to eX$ may be written quite generally in terms of two structure functions, $F_1(x,Q^2)$ and $F_2(x,Q^2)$, which parameterise the structure of the proton as seen by the virtual photon;

$$\frac{\mathrm{d}^2\sigma_{ep\to eX}}{\mathrm{d}x\mathrm{d}Q^2} = \frac{4\pi\alpha_{em}^2}{xQ^4}\left[xy^2F_1(x,Q^2) + (1-y)F_2(x,Q^2)\right] \tag{3.30}$$

that is, all the QED structure has been factorised. In fact, the structure functions F_1 and F_2 are related to the cross sections for the scattering of longitudinally and transversely polarised photons, σ_L and σ_T respectively;

$$\sigma_L = \frac{4\pi^2\alpha_{em}}{Q^2}(F_2 - 2xF_1) \tag{3.31}$$

$$\sigma_T = \frac{4\pi^2\alpha_{em}}{Q^2}2xF_1 \tag{3.32}$$

The total DIS cross section may therefore be written

$$\frac{\mathrm{d}^2\sigma_{ep\to eX}}{\mathrm{d}x\mathrm{d}Q^2} = \frac{4\pi\alpha_{em}^2}{xQ^4}\left(1 - y + \frac{y^2}{2[1+R(x,Q^2)]}\right)F_2(x,Q^2) \tag{3.33}$$

where the photo-absorption ratio

$$R(x,Q^2) = \frac{\sigma_L(x,Q^2)}{\sigma_T(x,Q^2)} \tag{3.34}$$

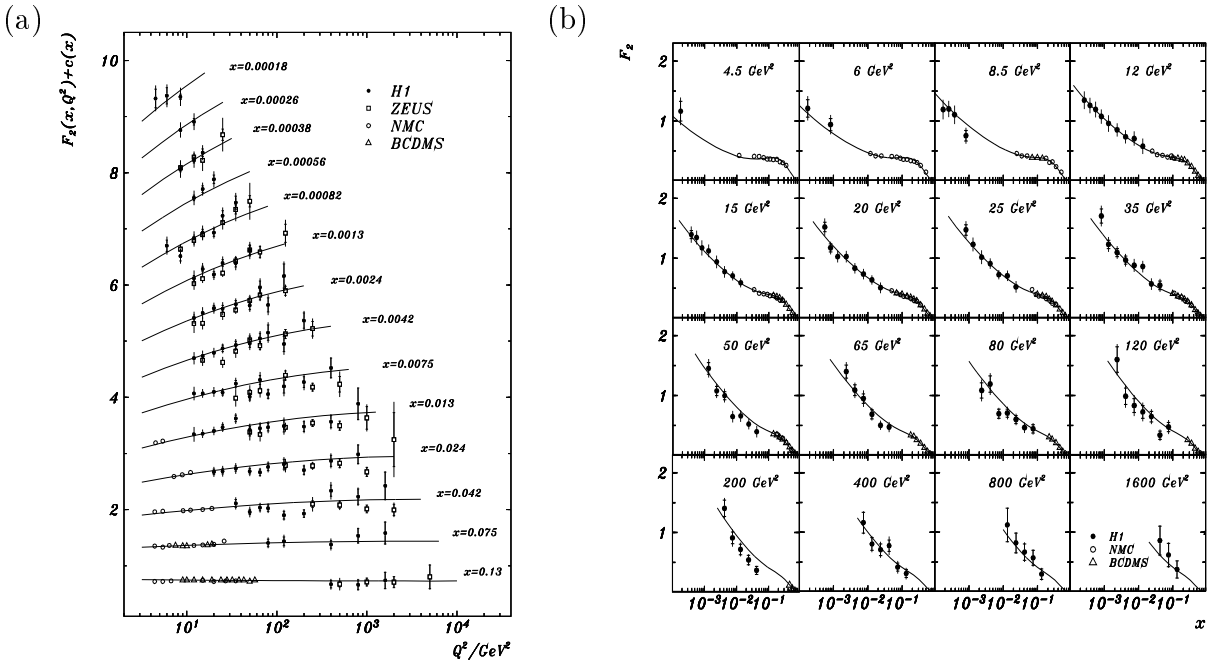

Figure 3.8: $F_2(x, Q^2)$ as measured at HERA, and in fixed target experiments, as a function of Q^2 (a) and x (b). The curves are a phenomenological fit performed by H1 [26]. $c(x)$ is an arbitrary vertical displacement added to each point in (a) for visual clarity, where $c(x) = 0.6(n - 0.4)$, n is the x bin number such that $n = 1$ for $x = 0.13$.

is known from low energy data to be negligible in comparison to F_2 [5]. To a very good approximation, therefore, the total DIS cross section is described by the single structure function F_2. The H1 measurement of the structure function F_2 is shown in figure 3.8, as a function of Q^2 (a) and x (b). The most striking feature is that, certainly at high x, the structure function is almost independent of Q^2. This behaviour, known as scaling, is at once suggestive that scattering is occurring not off the extended proton, but off point-like constituents within the proton. That is to say there is no length scale present in the problem. An intuitive way to examine the

[5]This statement is equivalent to the Callen-Gross [27] relation, to be discussed in this section in the context of the Quark-Parton model. Indeed, the experimental observation that the photo-absorption ratio is small can be taken as evidence of the spin $\frac{1}{2}$ nature of quarks.

structure functions is provided by the Quark Parton model (QPM), in which the proton is considered to be made up of a number of point-like constituents termed 'partons'. In the infinite momentum frame of the proton, the virtual photon 'sees' a time dilated 'frozen' parton distribution, i.e. parton-parton interactions are negligible on the time scale of the γ^*-parton interaction, and the cross section can be written as a sum over cross sections for elastic electron-parton scattering

$$\frac{\mathrm{d}^2\sigma}{\mathrm{d}x\mathrm{d}Q^2} = \sum_i \int_0^1 \mathrm{d}\zeta\, f_i(\zeta) \frac{\mathrm{d}^2\sigma}{\mathrm{d}\zeta\mathrm{d}Q^2}(\mathrm{e_i} \to \mathrm{e_i}) \tag{3.35}$$

where $f_i(\zeta)\mathrm{d}\zeta$ is the number of partons of type i carrying fraction ζ of the proton momentum, and the sum is over the partons of type i with charge e_i. Putting the scattered parton on shell gives

$$(q + \zeta p)^2 = 0 \tag{3.36}$$

and hence

$$\zeta = \frac{Q^2}{2q.p} \tag{3.37}$$

In other words, ζ is none other than the Bjorken scaling variable x of equation (3.25). The elastic cross section $\frac{\mathrm{d}^2\sigma}{\mathrm{d}\zeta\mathrm{d}Q^2}(\mathrm{e_i} \to \mathrm{e_i})$ is easily calculable in QED;

$$\frac{\mathrm{d}^2\sigma}{\mathrm{d}\zeta\mathrm{d}Q^2} = e_i^2 \frac{4\pi\alpha_{em}^2}{\zeta Q^4}\left[\frac{y^2}{2} + (1-y)\right]\delta(\zeta - x) \tag{3.38}$$

where it has been assumed that the partons are spin $\frac{1}{2}$, i.e. quarks[6] , and the on shell constraint has been applied. Equations (3.35), (3.37) and (3.38) therefore lead to

$$\frac{\mathrm{d}^2\sigma}{\mathrm{d}x\mathrm{d}Q^2} = \frac{4\pi\alpha_{em}^2}{xQ^4}\sum_i e_i^2 f_i(x)\left[\frac{y^2}{2} + (1-y)\right] \tag{3.39}$$

Comparison with equation (3.30) yields the two key results

$$F_2(x, Q^2) = \sum_i e_i^2 f_i(x) \tag{3.40}$$

and

$$2xF_1(x) = F_2(x) \tag{3.41}$$

[6]photons do not of course couple directly to gluons

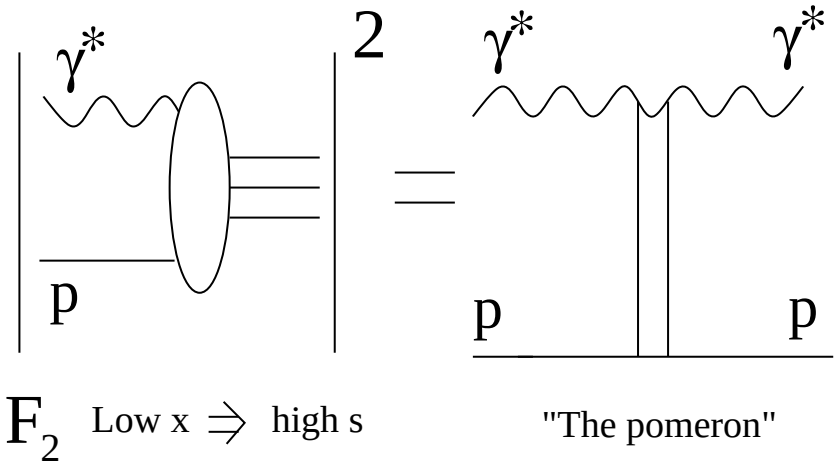

Figure 3.9: The total $\gamma^* p$ cross section, related to the elastic cross section by the optical theorem

Equation (3.40) follows directly from the assumption of point-like non-interacting constituents inside the proton, and is known as Bjorken scaling. Equation (3.41) is known as the Callen-Gross relation, and is a consequence of the assumption that the elastic scattering of the electron is off spin $\frac{1}{2}$ partons.

3.4.1 The Total DIS Cross Section and Regge Theory

The structure function F_2 can be thought of as the total virtual-photon proton cross section. It is interesting to note that, since the square of the photon-proton centre of mass energy is given by equation (3.29), the Regge limit $W^2 \gg Q^2$ is satisfied for sufficiently low x processes. That is, F_2 might be expected to have a $1/x$ to a power dependence, at fixed Q^2, similar to the s to a power dependence of the total cross section; in other words, driven by pomeron exchange. This is shown schematically, via the optical theorem, in figure 3.9. The prediction from Regge theory is, therefore, that at low Q^2

$$F_2(x, Q^2) \sim x^{-0.08} \tag{3.42}$$

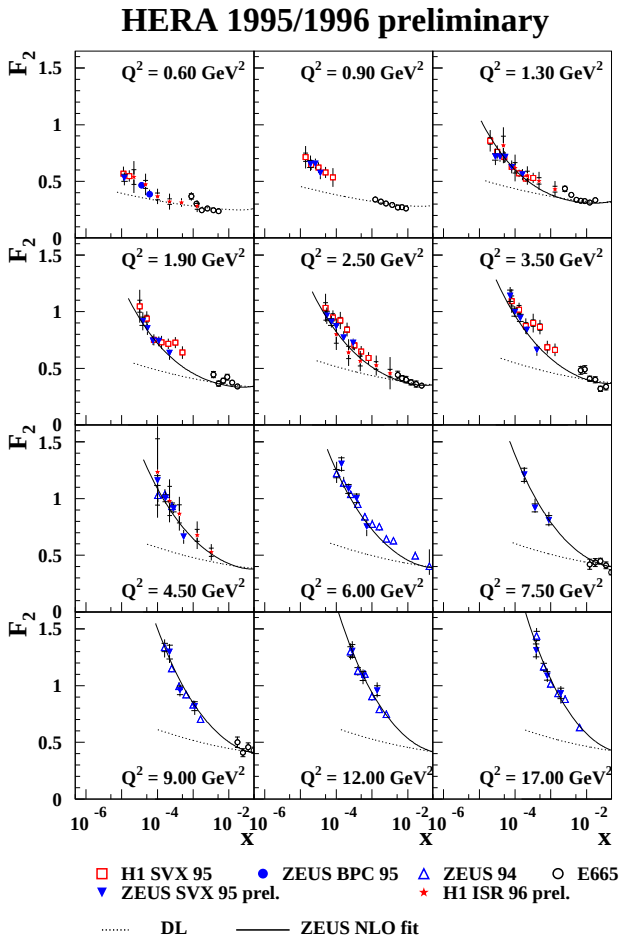

Figure 3.10: $F_2(x, Q^2)$ plotted against x for various Q^2 values. The dashed curve is the naive Regge prediction. The solid curve is the NLO DGLAP prediction.

Figure 3.10 shows all the available HERA data in the low Q^2 range up to the end of 1996. As Q^2 increases, the energy dependence of F_2 clearly steepens. The soft pomeron prediction is the dashed line labelled 'DL' in the figure. This is the first signal of the onset of pQCD corrections to the Regge picture described above. In the low x, high Q^2 regime, calculations using the BFKL [29] approach become possible, and lead to the prediction that F_2 should behave like $x^{-\omega_0}$, where ω_0 is observed to be around 0.3 for $Q^2 \sim 100\text{GeV}^2$, and is directly calculable within the BFKL formalism. This is discussed in more detail in the following section.

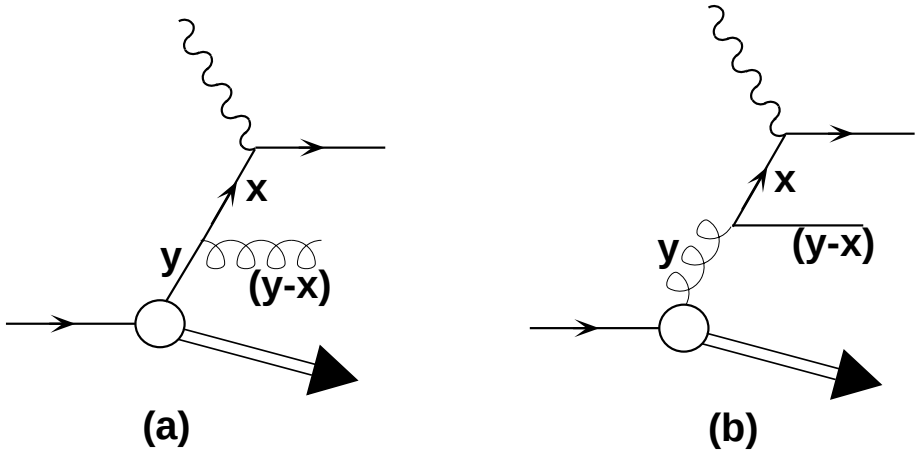

Figure 3.11: The Alterelli-Parisi splitting functions $P_{qq}(x/y)$ (a) and $P_{qg}(x/y)$ (b). The quark coupling to the photon with momentum fraction x originates from a quark or gluon carrying momentum fraction y of the proton.

3.4.2 Scaling Violations

Whilst the most striking gross feature of the data shown in figure 3.8 is scaling, it is also clear that at low x, F_2 does vary with Q^2. These 'scaling violations' signal the onset of pQCD corrections to the simple Quark-Parton model, and are indicative of the fact that, even at large Q^2, partons should be regarded as weakly interacting, not free, objects. For example, a struck quark may radiate a gluon, before or after its interaction with the virtual photon, or a gluon in the proton may split into a $q\bar{q}$ pair, which may then interact with the photon. These processes, shown in figure 3.11 are $\mathcal{O}(\alpha\alpha_s)$ contributions to the structure function (the leading contribution is $\mathcal{O}(\alpha)$). Such processes result in logarithmic corrections to the structure functions of the form $\alpha_s \log Q^2$ and $\alpha_s \log \frac{1}{x}$. Multiple gluon emissions and splittings lead to ladder diagrams such as that shown in figure 3.12. The logarithmic terms arise from the loop integrals in the amplitude. Consider the particular loop denoted by L in figure 3.12. The four momentum of the parton at the i^{th} rung k_i can be written as a linear superposition of the proton and virtual photon four momenta in the frame

collinear with the incoming proton and photon, and a transverse component $k_{\perp i}$;

$$k_i = \alpha_i p + \beta_i q^{'} + k_{\perp i} \tag{3.43}$$

where

$$q^{'} = q + x_{bj} p, \tag{3.44}$$

p is the four-momentum of the incoming proton, q is the four-momentum of the incoming photon and x_{bj} is the scaling variable of section 3.4. ($q^{'}$ is used because $q^{'2} = 0$, as is easily verified). This is known as the Sudakov decomposition of the four-vector k_i [7]. The loop integral will therefore have the form

$$\mathrm{L} \sim \int \frac{\mathrm{d}^4 k_i}{k_i^2} \sim \int \frac{\mathrm{d}\alpha_i \mathrm{d}\beta_i \mathrm{d}^2 k_{\perp i}}{\alpha_i \beta_i s - k_{\perp i}^2} \times f(\alpha_i, \beta_i, k_{\perp i}) \tag{3.45}$$

The β integral is removed by the on shell conditions across the cut line (this is an application of the Cutkosky Rules), and in certain kinematic regimes L becomes a logarithmic integral in either $k_{\perp i}$ or α_i. Of course, the full QCD calculation of an n rung ladder is intractable. In order to progress further, the dominant logarithmic terms in a particular regime are summed. For a large part of the phase space in which pQCD is applicable at HERA the leading $\log Q^2$ approximation is found to be sufficient, i.e. $\alpha_i \beta_i s \ll |k_{\perp i}^2|$. This corresponds to keeping only those terms in the perturbative expansion of the form $\alpha_s^n \log^n(Q^2)$, which lead to the DGLAP equations [28] for the quark and gluon densities;

$$\frac{\partial q_i(x,Q^2)}{\partial \log(Q^2/\Lambda^2)} = \frac{\alpha_s(Q^2)}{2\pi} \int_x^1 \frac{\mathrm{d}y}{y} \left[P_{qq}\left(\frac{x}{y}\right) q_i(y,Q^2) + P_{qg}\left(\frac{x}{y}\right) g(y,Q^2) \right] \tag{3.46}$$

$$\frac{\partial g_i(x,Q^2)}{\partial \log(Q^2/\Lambda^2)} = \frac{\alpha_s(Q^2)}{2\pi} \int_x^1 \frac{\mathrm{d}y}{y} \left[\sum_i P_{gq}\left(\frac{x}{y}\right) q_i(y,Q^2) + P_{gg}\left(\frac{x}{y}\right) g(y,Q^2) \right] \tag{3.47}$$

where, for example, $P_{qq}(x/y)$ is the 'splitting function' describing the probability of a struck quark of momentum fraction x having been originated by the gluon bremsstrahlung process (figure 3.11(a)) from a quark with momentum fraction y.

[7] The Sudakov decomposition is introduced here partly because of its use in the development of the double diffractive dissociation phenomenology presented in chapter 6

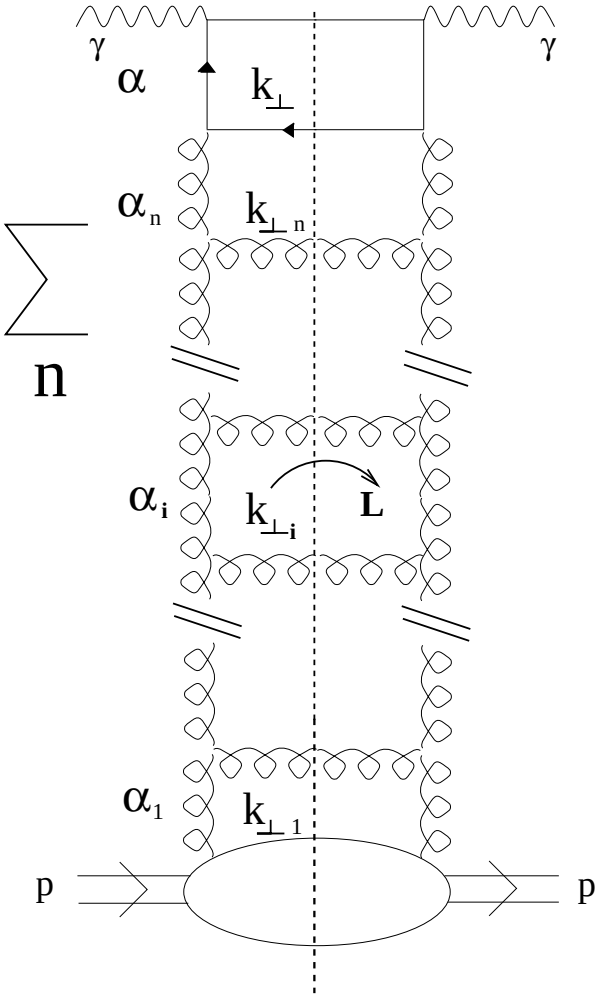

Figure 3.12: The ladder diagram representing the squared amplitude for multiple gluon emissions and splittings.

The terms $q_i(y, Q^2)$ and $g(y, Q^2)$ are the gluon and quark densities, of flavour i, in the proton at some scale Q^2. The diagrams which contribute to this summation have the longitudinal momenta ordered along the chain $\alpha_i > \alpha_{i+1}$ and the transverse momenta strongly ordered $k^2_{\perp i} \ll k^2_{\perp i+1}$. The way to visualise the evolution is to notice that, to a good approximation, α at the top of the ladder is x_{bj}, whilst $k^2_\perp$ is $\mathcal{O}(Q^2)$, the virtuality of the incoming photon. So essentially, the DGLAP equations allow a parton density known at a particular scale Q^2_0, where Q^2_0 is large enough for pQCD to be applicable, to be 'evolved' to give the parton density at some other

higher scale Q^2. The splitting functions have been calculated up to next to leading order in QCD, and solving the DGLAP equations leads to the logarithmic corrections to the structure functions seen in the data.

At very low x (possibly outside the HERA range) the DGLAP formalism will fail because the $\log \frac{1}{x}$ terms become dominant. In the leading logarithmic approximation (LLA) at low x, only those graphs which contain gluon loops with a strong ordering of the longitudinal momenta up the ladder, $\alpha_i \gg \alpha_{i+1}$, need be considered, since only these graphs contribute the maximal number of logs, i.e. terms of the form $\alpha_s^n \log^n(1/x)$. These terms are summed by the BFKL equation [29]. At leading log, the P_{gg} splitting term is the only one that need by considered because terms involving quark loops (involving the P_{qg} term) are suppressed by $\log(1/x)$. Within the next to leading log approximation (NLLA), such terms do enter, however. These corrections to the BFKL summation have recently been completed [30]. Cross sections using the BFKL formalism in this thesis have been calculated within the LLA. Notice that summing the leading $\log \frac{1}{x}$ terms is in fact equivalent to summing the leading $\log(s)$ contributions, since in the limit $s \gg Q^2$, $x \sim Q^2/s$ and so $\log(1/x) \sim \log(s/Q^2)$ (as discussed in section 3.4.1). The BFKL equation therefore gives the leading $\log(s)$ behaviour of the scattering amplitude in the Regge limit in QCD, that is the QCD pomeron. Within the LLA, the QCD coupling α_s is treated as a constant term [8] (i.e $\alpha_s(Q^2) = \alpha_0$), and the BFKL equation can be solved analytically to give the QCD pomeron intercept;

$$\alpha_{I\!P} = 1 + \omega_0 = 1 + N_c 4 \ln 2 \frac{\alpha_s}{\pi} \tag{3.48}$$

where N_c is the number of colours participating at the relevant scattering energy, 3 at HERA. It is a measurement of ω_0 which is the goal of Chapters 5 and 6.

[8] At next to leading log, however, terms involving 'bubble graphs' which run the coupling do enter, and the scale dependence of α_s returns

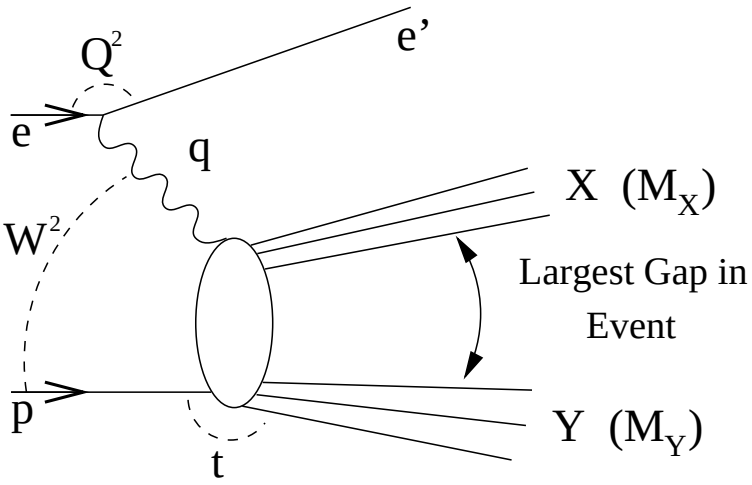

Figure 3.13: The Diffractive DIS process at HERA

3.5 Diffractive DIS

When the HERA experiments began taking data in 1992, a class of events in which there was a large rapidity gap between the proton direction and the forward edge of the hadronic system X was observed [31]. Such events can be interpreted as the result of the highly virtual photon probing the structure of a colour singlet object, which will here be visualised as a pomeron, 'offered up' out of the proton, as shown in figure 3.13. Given this topological decomposition of the hadronic final state, a further set of invariant quantities may be defined;

$$t = (p - Y)^2 = (q - X)^2 \tag{3.49}$$

$$x_{I\!P} = \frac{q.(p - Y)}{q.p} \tag{3.50}$$

$$\beta = \frac{Q^2}{2q.(p - Y)} \tag{3.51}$$

The process may then be described, by analogy with the definition of the proton structure function (equation (3.4)), by a structure function $F_2^{D(4)}$;

$$\frac{\mathrm{d}^4\sigma^D(ep \to epX)}{\mathrm{d}\beta \mathrm{d}Q^2 \mathrm{d}x_{I\!P} \mathrm{d}t} = \frac{4\pi\alpha_{em}^2}{\beta Q^2}\left(1 - y + \frac{y^2}{2}\right) F_2^{D(4)}(\beta, Q^2, x_{I\!P}, t) \tag{3.52}$$

If the above picture is to be useful, it might be assumed that $F_2^{D(4)}$ should be factorisable into two terms involving the variables associated with the upper and lower ends of the diffractive exchange;

$$F_2^{D(4)}(\beta, Q^2, x_{I\!P}, t) = f_{I\!P}/p(x_{I\!P}, t) F_2^{I\!P}(\beta, Q^2) \tag{3.53}$$

where $f_{I\!P}/p(x_{I\!P}, t)$ is a pomeron flux factor which, at low t, should be described by Regge theory, and $F_2^{I\!P}(\beta, Q^2)$, the pomeron structure function, is associated with the hard interaction between the pomeron and the virtual photon. The prediction from Regge theory for $f_{I\!P}/p(x_{I\!P}, t)$ can be obtained by using equation (3.20) for the process $ep \to (e + X)p$. At fixed M_{eX}

$$\frac{\mathrm{d}^2\sigma}{\mathrm{d}t\mathrm{d}M_{eX}^2} \sim \left(\frac{s}{M_{eX}^2}\right)^{2\alpha(t)-2} \tag{3.54}$$

where M_{eX}^2 provides a scale. [9] Since $x_{I\!P} \sim M_{eX}^2/s$, equation (3.54) may be written

$$\frac{\mathrm{d}^2\sigma}{\mathrm{d}t\mathrm{d}x_{I\!P}} \sim \left(\frac{1}{x_{I\!P}}\right)^{2\alpha(t)-1} \tag{3.55}$$

The pomeron flux can therefore be parameterised as

$$f_{I\!P}/p(x_{I\!P}, t) \sim f(t) \left(\frac{1}{x_{I\!P}}\right)^{2\alpha(t)-1} \tag{3.56}$$

Because of the difficulty in determining t from the hadronic final state, both the H1 and ZEUS collaborations have in fact measured the quantity $F_2^{D(3)}(\beta, Q^2, x_{I\!P})$ [13, 32], integrated over some t range. The H1 measurement is shown in figure 3.14. The fits shown on the plot are in fact a combination of a pomeron term and a sub-leading meson term

$$F_2^{D(3)} = f_{I\!P/p}(x_{I\!P}) F_2^{I\!P}(\beta, Q^2) + f_{I\!R/p}(x_{I\!P}) F_2^{I\!R}(\beta, Q^2) \tag{3.57}$$

where the flux factors $f_{I\!P/p}(x_{I\!P})$ and $f_{I\!R/p}(x_{I\!P})$ are parameterised as

$$f_{I\!P/p}(x_{I\!P}) = \int_{t_{cut}}^{t_{min}} \frac{e^{\beta_{I\!P}(t)}}{x_{I\!P}^{2\alpha_{I\!P}(t)-1}} \tag{3.58}$$

[9] There is of course a scale associated with equation (3.20). This is typically taken to be 1 GeV^2 and was omitted for simplicity

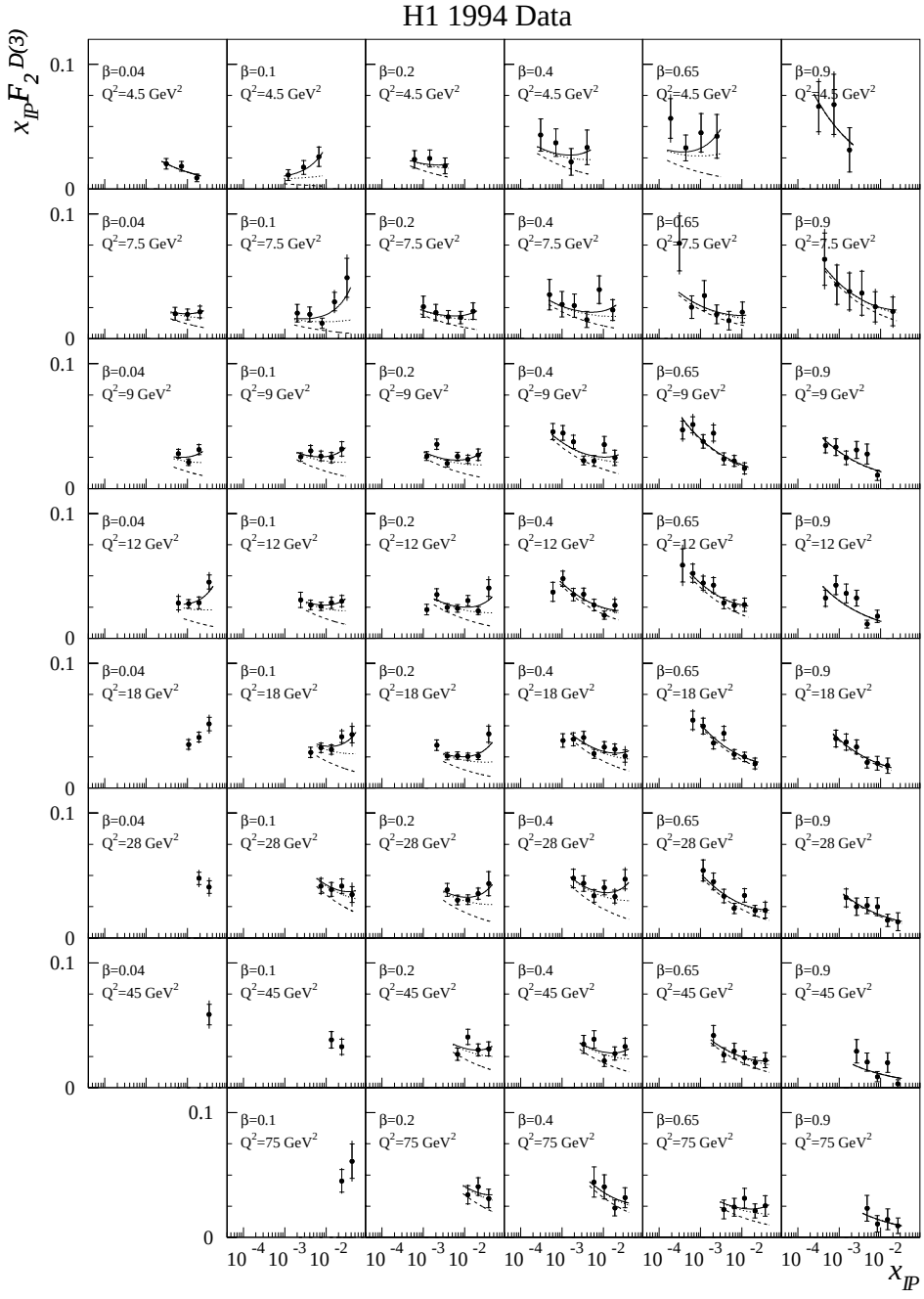

Figure 3.14: $x_{I\!P} F_2^{D(3)}(x_{I\!P}, \beta, Q^2)$ plotted against $x_{I\!P}$ for various β and Q^2 values. The solid curve shows the results of the Regge fit described in the text. The dashed curve is the contribution from the pomeron alone. Further details can be found in [13]

$$f_{I\!R/p}(x_{I\!P}) = \int_{t_{cut}}^{t_{min}} \frac{e^{\beta_{I\!R}(t)}}{x_{I\!P}^{2\alpha_{I\!R}(t)-1}} \tag{3.59}$$

$\beta_{I\!P}$, $\beta_{I\!R}$, $\alpha'_{I\!P}$ and $\alpha'_{I\!R}$ are taken from hadron-hadron scattering data and $\alpha_{I\!P}(0)$, $\alpha_{I\!R}(0)$, $F_2^{I\!P}(\beta, Q^2)$ and $F_2^{I\!R}(\beta, Q^2)$ are left free in the fit. The fits yield an intercept for the pomeron of $\alpha_{I\!P}(0) = 1.203 \pm 0.020(\text{stat.}) \pm 0.013(\text{sys.})^{+0.030}_{-0.035}(\text{model})$ and an intercept for the sub-leading exchange of $\alpha_{I\!R}(0) = 0.5 \pm 0.11(\text{stat.}) \pm 0.11(\text{sys.})^{+0.09}_{-0.10}(\text{model})$. The sub-leading reggeon trajectory is therefore consistent with the ρ trajectory described in section 3.1.5. The pomeron intercept is significantly higher than the 'soft' pomeron intercept of 1.08. The reason for the stronger energy dependence, which may be compared with the strong rise of F_2 at low x, discussed in section 3.4.1, is still an unanswered question. Donnachie and Landshoff [33] have recently proposed that there may be two pomerons; a soft pomeron of intercept 1.08 and a hard pomeron of intercept 1.4, with Q^2 dependent coefficients describing the mixing between the two and therefore the overall energy dependence of the scattering process as a function of the photon virtuality. From a QCD viewpoint, it seems clear that the answer must depend to some extent on the structure of the photon itself. This will be discussed in the following section.

3.6 Photon Physics at HERA

Since the differential ep cross section contains a $1/Q^4$ term (equation (3.33)), the overwhelming majority of events at HERA involve the electron emitting an almost on shell photon which then interacts with the proton. For these events, HERA is really a γp collider, with centre of mass energy $W^2_{\gamma p} = ys$, and it is sensible to factor out a photon flux, and quote a γp cross section $\sigma_{\gamma p}$ where

$$\frac{\mathrm{d}^2\sigma_{\mathrm{ep}}(\mathrm{s})}{\mathrm{dQ}^2\mathrm{dy}} = \sigma_{\gamma p}(ys)F(y, Q^2) \tag{3.60}$$

The photon flux factor $F(y, Q^2)$ can be calculated using the Weizsacker-Williams approximation [34], (see section 6.7). The picture of the scattering process is, in this

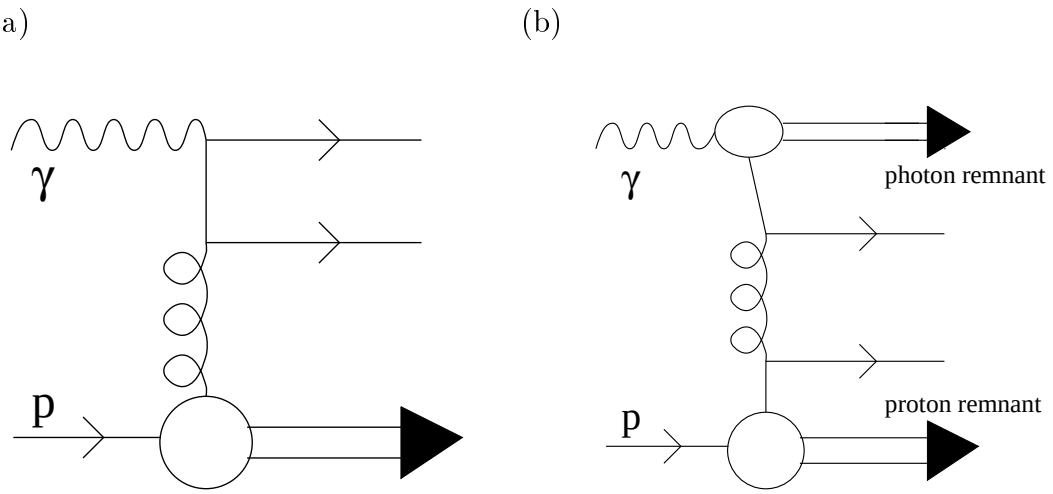

Figure 3.15: The leading order Direct (a) and Resolved (b) photon-proton collision processes.

case, different from that of DIS, in which a highly virtual photon probes the structure of the proton or pomeron. The photon can either interact as a point-like object, coupling directly to a quark in the boson-gluon fusion process shown in figure 3.15 (a), or the real photon-proton collision can look more like a hadron-hadron scattering process, in which the photon fluctuates into a quark-antiquark pair long before the interaction with the proton takes place. Subsequent QCD evolution of the $q\bar{q}$ pair may then occur, leading naturally to the concept of a photon structure function $F_2^\gamma(x_\gamma, Q^2)$ by analogy with the proton. The photon will then contain not only quarks but gluons, and the proton-photon interaction is viewed as a hard scatter between a parton in the proton and a parton in the photon. This process is termed the resolved process, and is shown in figure 3.15 (b). The energy dependence of the total photon-proton cross section is found to be the same as that for other hadron-hadron cross section, i.e. driven by pomeron exchange with intercept 1.08 [35].

3.6.1 The Photon in Diffractive Interactions

In order for the photon to interact with a proton via pomeron exchange, it must of course fluctuate into a $q\bar{q}$ pair (which may evolve into some more complicated object) before the interaction with the proton. Historically, this process has been modelled using the vector dominance approach and its derivatives [36], in which the photon is considered as a linear superposition of all the meson states with the same quantum numbers. A ready analogy with optical diffraction presents itself [37]. Consider a beam of plane polarized light incident on a Polaroid with a non-zero angle between its polarization axis and that of the incoming beam. The component of the incoming light polarized parallel to the Polaroid will be absorbed, heating the Polaroid up. This is analogous to inelastic scattering. The light which passes through the Polaroid will necessarily emerge polarized along the same direction as the Polaroid, a different direction to the incoming beam. This light will contain two polarization states, one which was present in the incoming beam, corresponding to the true elastic diffractive process $\gamma p \to \gamma p$, and a new state, whose polarization is orthogonal to that of the incoming beam. These are the diffractive dissociation or 'quasi-elastic' process shown in figure 3.16, in which a new state is 'diffracted into existence' by the target, in this case the proton. Notice that this analogy relies upon the produced states being energy degenerate with the incoming states (which of course is true in the optical case). This is achieved in the γp case only if the centre of mass energy $s \gg$ all masses in the problem, i.e. the Regge limit, and this is why diffractive processes are characterised by large rapidity gaps.

The modern realisation of the vector meson dominance model, which attempts to incorporate the hadronic nature of the photon fluctuation, is the colour dipole model [38]. The photon state vector is written as the sum over diffractive eigenstates $|z, r\rangle$, where z describes the fraction of the photon energy carried by each quark in

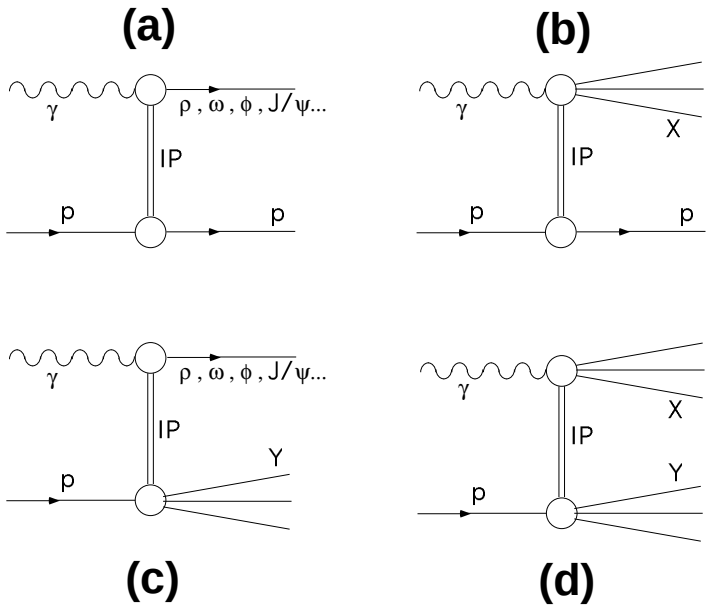

Figure 3.16: Diffractive interactions in γp collisions; (a) Quasi-elastic vector meson production. (b) Single photon dissociation (c) Single proton dissociation. (d) Double dissociation

the pair and r describes the transverse size of the fluctuation;

$$|\gamma\rangle = \int \mathrm{d}z\mathrm{d}^2r\ \psi_\gamma(z,r)\,|z,r\rangle \tag{3.61}$$

$\psi_\gamma(z,r)$ is then interpreted as the photon wavefunction in the 'diffractive basis', i.e. the probability to find a particular eigenstate of diffraction in the photon. One could then, for example, write the cross section for vector meson production as

$$\frac{\mathrm{d}\sigma}{\mathrm{d}t} = \frac{1}{16\pi}\left[\int \mathrm{d}z\mathrm{d}^2r\ \psi_V^*(z,r)\psi_\gamma(z,r)\sigma(s,r)\right]^2 \tag{3.62}$$

where ψ_V is the vector meson wavefunction and $\sigma(s,r)$ is a universal cross section for scattering a dipole of size r off a proton at centre of mass energy s.

The evolution of the parameters of the 'effective pomeron trajectory' with different scales in the interaction is nowhere more visible than in the quasi-elastic production of vector mesons, the process of figure 3.16 (a). Figure 3.17 shows the energy dependence of the total cross sections for the ρ, ω, ϕ and J/ψ, together with

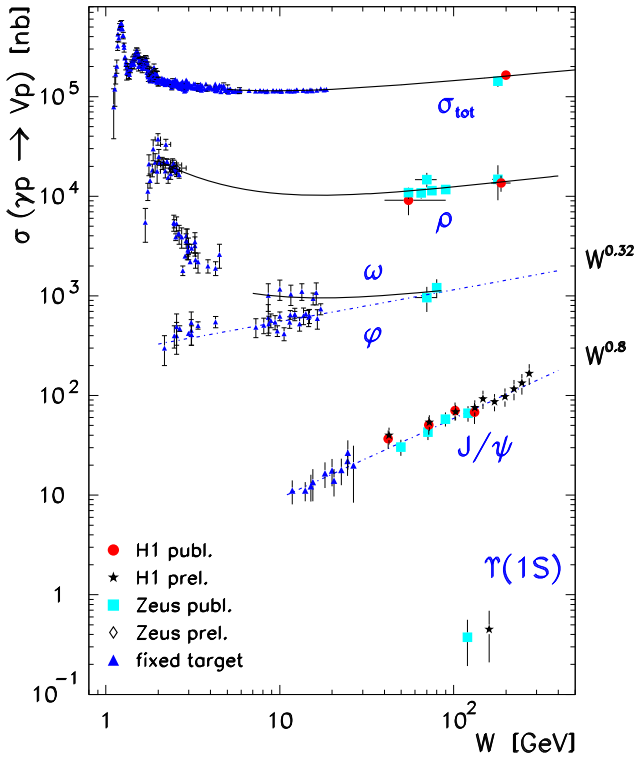

Figure 3.17: The energy dependence of the total cross sections for vector meson production at HERA and fixed target experiments, compared with the total γp cross section

the total γp cross section, whose energy dependence is driven purely by the soft pomeron. The energy dependence of the production cross sections is clearly seen to steepen with increasing meson mass, the only hard scale present in the process. Recent measurements of the energy dependence of the ρ production cross section in electroproduction by the H1 Collaboration [39] also provide clear evidence of an increasing effective pomeron intercept with Q^2, an effect suggested by the higher value of the intercept obtained from the total DIS cross section than that from the total γp cross section. [10]

[10] A complete review of the behaviour of diffraction and low x physics at different scales may be found in [40]

3.7 Concluding Remarks

There is now overwhelming evidence from HERA that the pomeron trajectory is not universal; that is, the energy dependence of cross sections in the Regge limit may depend on other scales present in the process, such as the virtuality of the photon or the mass of the produced vector meson. When hard scales are present, the use of perturbative QCD becomes possible, at least in principle, and the opportunity to probe the high energy behaviour of the strong interaction is no longer purely a matter for Regge phenomenology. The measurements presented in the following chapters are aimed at broadening the investigation of diffraction at different scales to include high momentum transfer processes, where the momentum transfer referred to is across the rapidity gap; the pomeron itself has a large virtuality. This will of course usually result in the proton breaking up, i.e. the double dissociation process of figure 3.16 (d). The very existence of such events is unexpected within conventional Regge phenomenology. Recall from section 3.1.5 that the cross section for any process involving a pomeron with a sloping trajectory ($\alpha' \neq 0$) must fall very rapidly with increasing $|t|$, since

$$\frac{\mathrm{d}\sigma}{\mathrm{dt}} \simeq s^{2\alpha(0)+2\alpha' t-2} \tag{3.63}$$

This effect is known as shrinkage, and it would suppress any high $|t|$ diffractive events if the only pomeron were that suggested by Donnachie and Landshoff, with $\alpha' \sim 0.25$. The observation of events in just such a region is the subject of the following chapter.

Chapter 4

Rapidity Gaps Between Jets

4.1 The Experimental Signature of High $|t|$ Diffraction

The aim of the study in this thesis is to isolate a class of events which are likely to be diffractive, in the sense that the scattering process is mediated by the exchange of a strongly interacting colour singlet object, and driven by short distance physics, allowing the use of pQCD. Such events would have a very clear experimental signature. Colour singlet exchange events will of course be characterised by the presence of a large rapidity gap in the hadronic final state. When the 4-momentum transfer, $|t|$, across the rapidity gap is sufficiently large, the gap producing mechanism will be driven by short distance physics [41]. In this kinematic region, the long distance physics can be factorised into the parton distribution functions of the beam particles, and the gap is assumed to be produced by a single elastic parton-parton scattering. The scattered partons will be knocked out of the beam hadrons with $p_T^2 \sim -t$, and for very high $|t|$ this will result in the formation of jets in the detector (the definition of a jet and the jet finding algorithm used is discussed in detail in

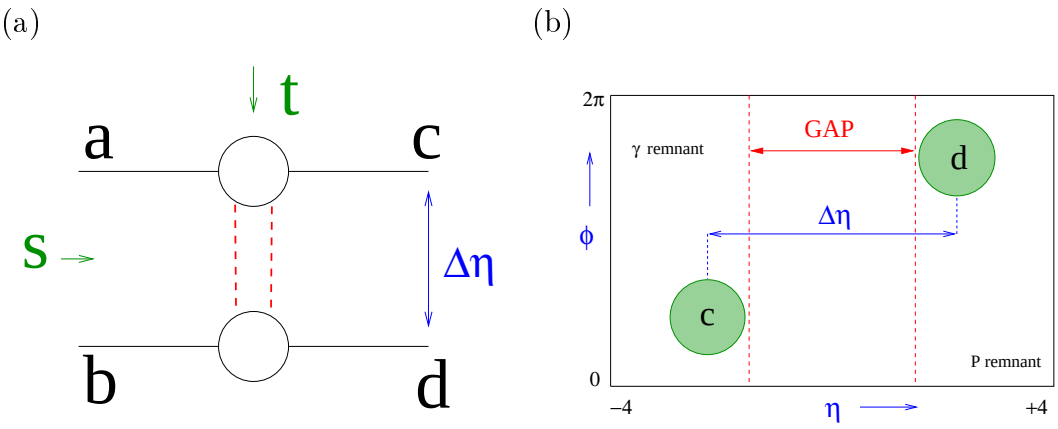

Figure 4.1: The underlying hard scattering process at parton level (a) and its signature at detector level (b). Parton 'a' originates from the incoming photon and parton 'b' from the proton.

appendix A). With this in mind, Mueller & Tang [42] suggested the study of dijet events in which there is a rapidity gap between the edges of the two highest E_T jets in the event. Of course, at HERA, this process can only occur in the resolved photoproduction process discussed in section 3.6, in which a parton from the photon scatters off a parton in the proton. The correlation between the hard scatter at the parton level and the experimental signature in the detector is shown schematically in figure 4.1.

Rapidity gaps can also be produced in events where the exchanged object carries net colour, i.e. a quark or a gluon, by multiplicity fluctuations in the hadronic final state. In order to distinguish between these events and genuine colour singlet mediated scattering events, the 'gap fraction' is introduced. The 'gap fraction', $f(\Delta\eta)$, is defined as the proportion of events containing two or more high E_T jets for which there is a gap in rapidity between the two highest E_T jets as a function of the jet - jet separation $\Delta\eta$. For processes involving the exchange of objects with

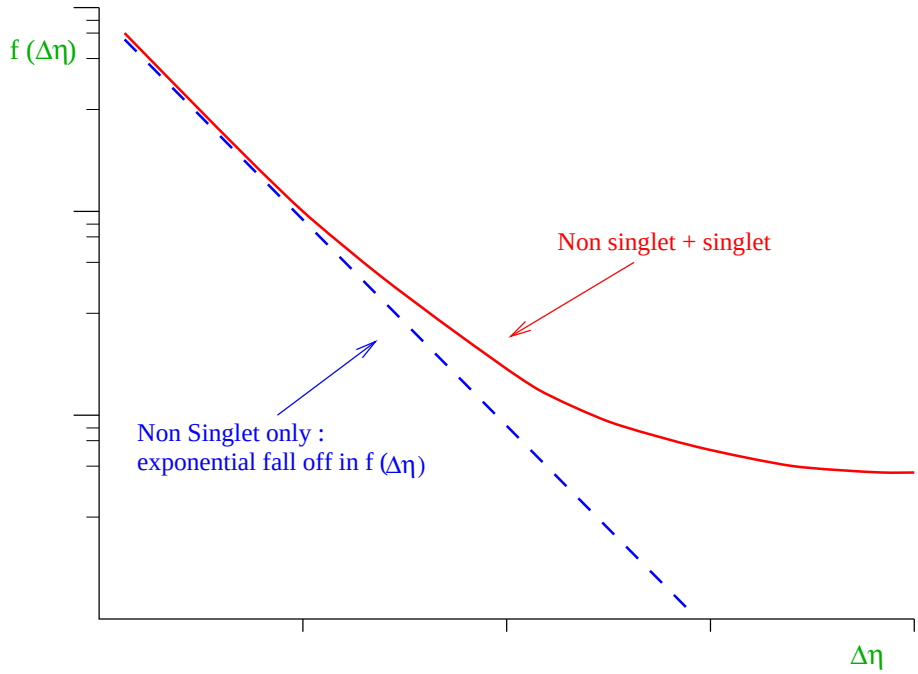

Figure 4.2: The expectations for the gap fraction $f(\Delta\eta)$ in the case of non-singlet exchange only (dashed line) and singlet+non-singlet exchange (solid line).

net colour, the naive expectation (the assumption that the multiplicity fluctuations obey simple Poisson statistics) is for $f(\Delta\eta)$ to decrease exponentially with increasing $\Delta\eta$. If colour singlet exchange also plays a role, then the gap fraction is expected to level off at some value of $\Delta\eta$. These expectations are shown in figure 4.2. The value of this level is interesting. It is related to the 'gap survival probability' of a colour singlet mediated scattering event. This issue will be discussed in section 4.7. If the gap survival probability were unity, the gap fraction would be expected to rise to 1.

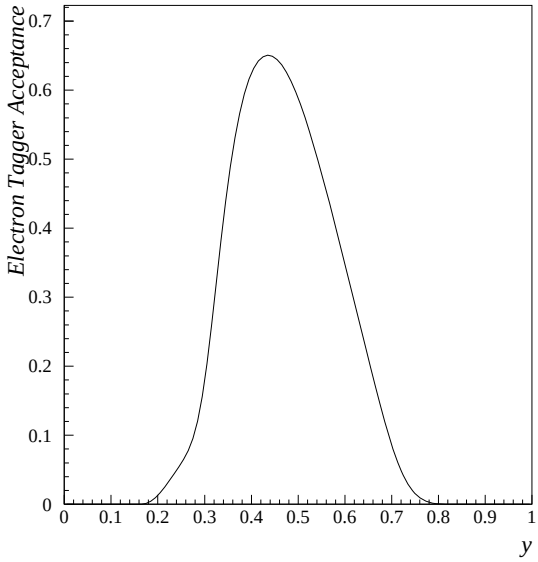

Figure 4.3: The acceptance of the 33 m electron tagger as a function of y for the 1996 running period. The trigger efficiency of the electron tagger trigger is folded into this plot (see section 6.3.2.)

4.2 Event Selection

4.2.1 Selection of Minimally Biased Photoproduction Events

The data used in this analysis were collected during the HERA 1996 running period, in which 27.6 GeV positrons were collided with 820 GeV protons. Events are selected in which the scattered positron is detected in the electron tagger, which also provides an energy measurement, E_{tagger}. This restricts the virtuality of the photon to $Q^2 < 0.01\text{GeV}^2$. The acceptance of the electron tagger as a function of y is shown in figure 4.3. [1]. The analysis is restricted to the range $0.28 < y < 0.65$, where

[1]The tagger acceptance is particularly sensitive to the HERA beam optics, and it changes from run to run. A weighting method is used whereby the acceptance is parameterised for each run and a weighted acceptance function is calculated for the period in which the data used in the analysis was taken. This procedure is described in detail in reference [35].

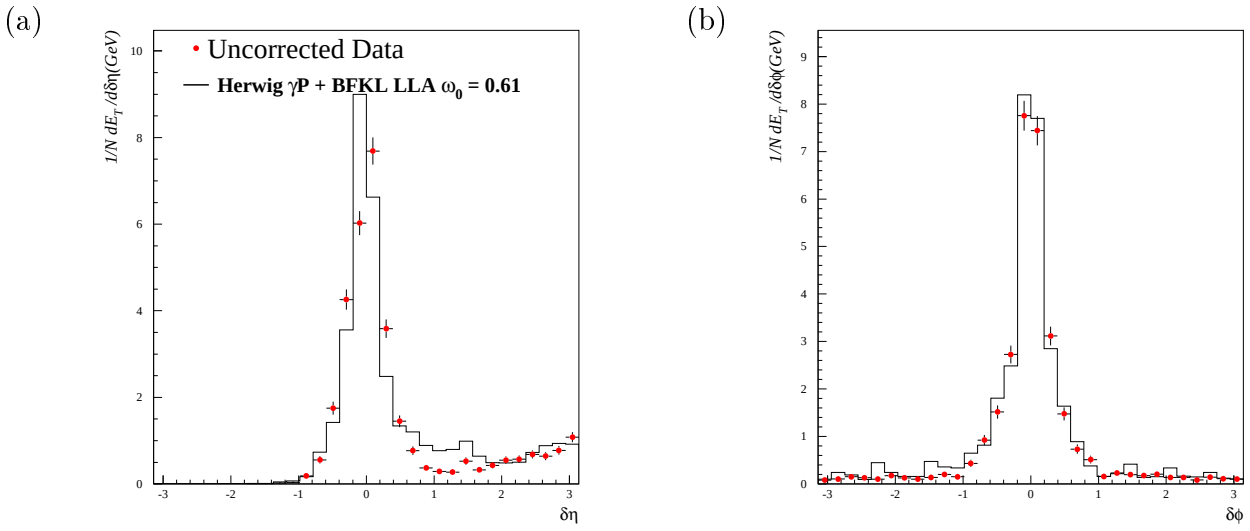

Figure 4.4: Jet profiles for jets with $\eta < -1.5$

y is calculated from the scattered positron energy, to avoid regions of low tagger acceptance. This corresponds to a γp centre of mass energy in the range $158 < W < 247$ GeV. Background from the Bremsstrahlung process is removed by requiring that the energy measured in the photon detector of the luminosity system, $E_{pd} < 2$ GeV.

4.2.2 Jet Finding

Jets are found using the CDF cone algorithm [43] with cone size 1.0 and $E_T^{jet} > 4.5$ GeV (see appendix A). Jet pseudorapidities are restricted to the range $-2.82 < \eta < 2.35$ in order to ensure that the jet cones are completely contained within the Liquid Argon and SPACAL calorimeters. [2] The pseudorapidity difference between the jets, $\Delta\eta$, is required to be greater than 2 units of rapidity, to ensure that the jet cones do not overlap. This analysis was one of the first to use the SPACAL calorimeter for jet finding, and as such, particular attention was paid to the reconstruction of jets in the backward region. The SPACAL begins at $\eta = -1.42$, and

[2] This leads to a fundamental restriction in the largest measurable rapidity gap size of $\simeq 2.5$. This problem will be addressed in chapter 5

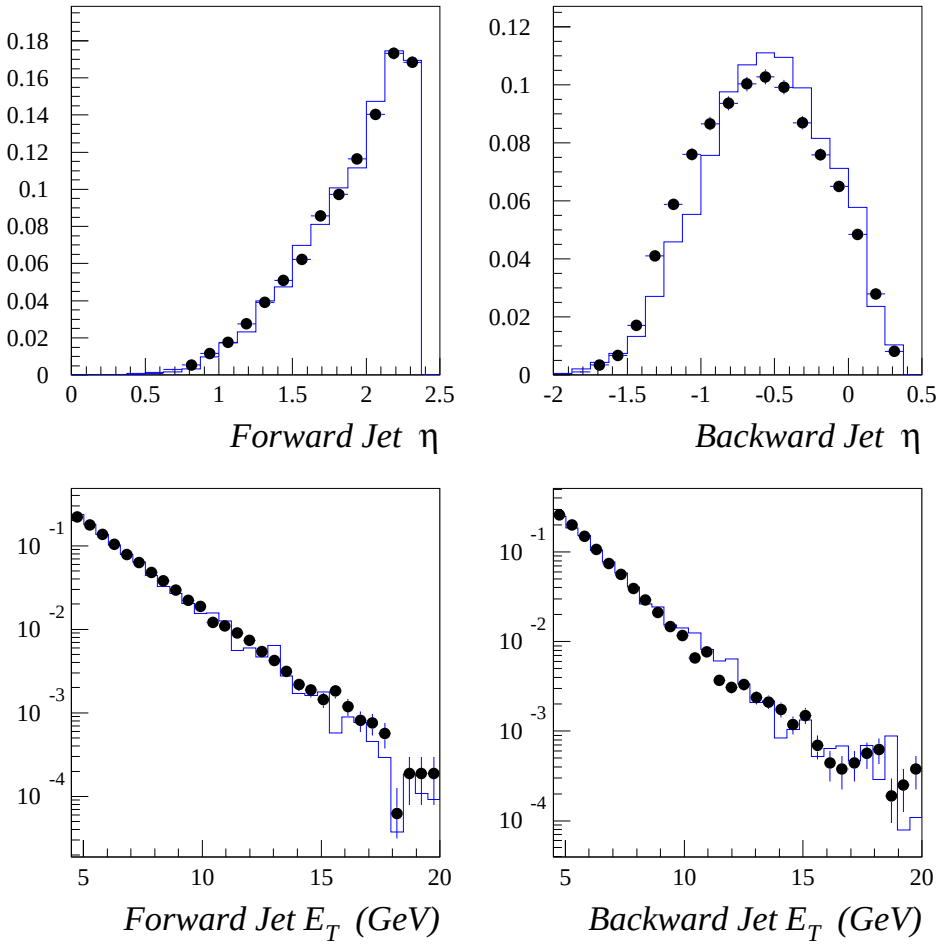

Figure 4.5: Control plots for the E_T and η distributions of the forward and backward jets. H1 data are shown as points. The histograms are the prediction of the HERWIG simulation. The area under each plot is normalised to unity.

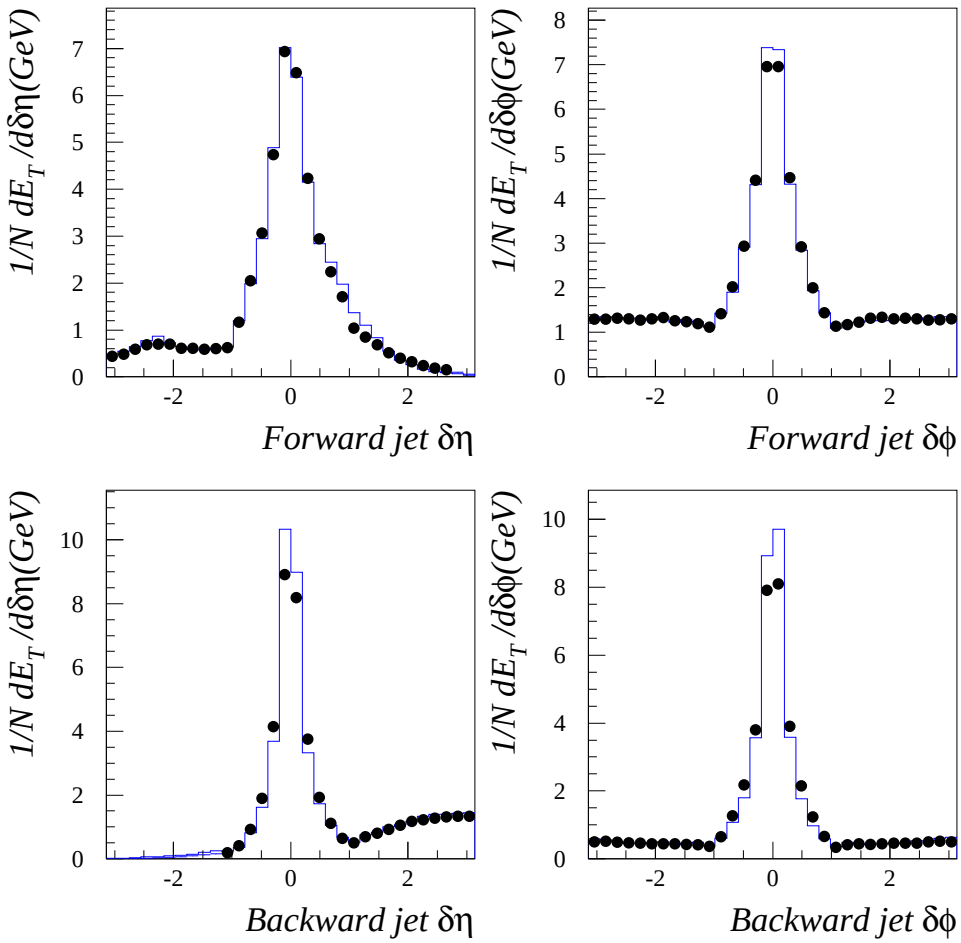

Figure 4.6: Jet profiles for the forward (proton direction) and backward jets. H1 data are shown as points. The histograms are the prediction of the HERWIG simulation.

(a) (b)

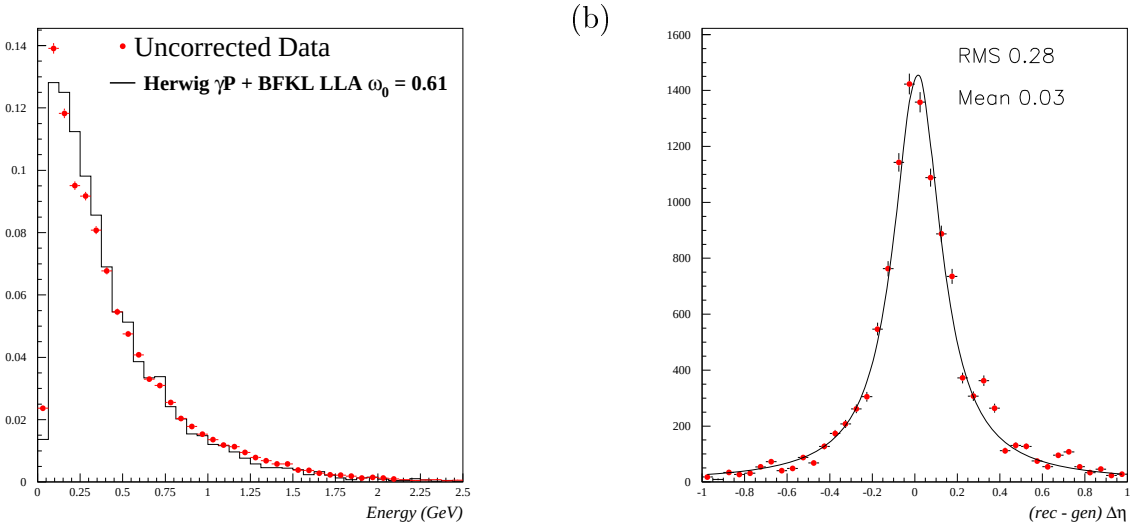

Figure 4.7: The energy flow between the edges of the jet cones (a) and the resolution in $\Delta\eta$ (b)

so jets with pseduorapidity of $\eta \sim -1.5$ will have at least half their cone contained within the SPACAL. Figure 4.4 [3] shows the jet profiles in the pseudorapidity region $\eta < -1.5$. [4] These should be compared with the backward jet profiles of figure 4.6. Both the average jet E_T and the energy flow outside the cone is consistent with the sample which includes the Liquid Argon η range. Furthermore, the Monte Carlo description of the profiles is good, which means that the detector simulation and therefore the acceptance corrections are well understood.

4.2.3 The Selection of Gap Events

A rapidity gap event is defined as an event in which there is no calorimeter cluster of energy $E > 400$ MeV in the rapidity interval between the edges of the cones

[3] All plots in this chapter are made after the full analysis cuts detailed in table 4.1

[4] The η profile is made by plotting $\delta\eta = \eta^{cluster} - \eta^{jet}$, weighted by the cluster transverse energy E_T, for clusters within one radian in ϕ of the centre of the jet. The ϕ profile is similarly defined for clusters within 1 unit of rapidity of the jet centre.

(a) (b)

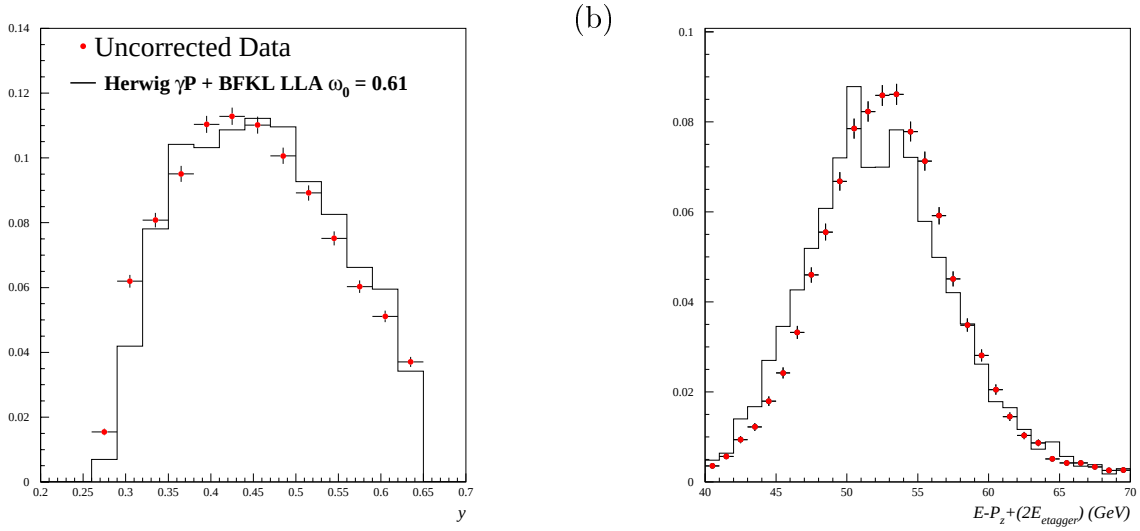

Figure 4.8: Control plots showing y as measured in the electron tagger (a) and total $(E - P_z)$ which should peak at 55 GeV (b)

containing the two highest E_T jets. This definition is designed to avoid the rejection of genuine rapidity gap events due to detector noise, and has been used in previous H1 diffractive analyses [13]. The gap fraction at the hadron level is defined in the same way; that is to say, the quoted gap fraction is corrected back to the case where, at the hadron level, there is no hadron outside the jet cones of energy $E > 400$ MeV. The energy flow between the edges of the jet cones is shown for both data and Monte Carlo in figure 4.7 (a). The resolution in $\Delta\eta$ is shown in figure 4.7 (b). The rms value of 0.28 from this plot leads to the choice of 4 bins in the range $2 \leq \Delta\eta \leq 4$.

4.2.4 Background Rejection

The requirement of observing two high E_T jets in the detector is a very clear signal and it has little non-collision background. In particular, the requirement that an electron is seen in the tagger effectively removes the potentially difficult problem of a DIS electron 'faking' a jet in the backward direction. Even so, to be safe, the requirement that a vertex is reconstructed in the region of the bunch crossing

$0.28 < y < 0.65$
$E_{tagger} > 6$ GeV
$E_{pd} < 2$ GeV
-25 cm $< zvtx < 35$ cm
1 vertex-linked track
$E_T^{jet} > 4.5$ GeV
$-2.82 < \eta^{jet} < 2.35$
$\lvert\eta_1^{jet} - \eta_2^{jet}\rvert > 2$
40 GeV $< \sum(E - P_z) + 2E_{tagger} < 70$ GeV

Table 4.1: The complete set of kinematic and background rejection cuts used in the rapidity gaps between jets analysis

point, with at least one track linked to the vertex from the central or forward tracker, is made. One source of non collision background is found to be a problem, however. The electron beam at HERA is 'shadowed' by so called 'beam halo muons', which pass through the detector parallel to the beam pipe. An example of such an event is shown in figure 6.10. If such a muon event overlays a well reconstructed photoproduction event, then the energy deposited in the forward and backward calorimeters by the muon can fake a photoproduction dijet event with a large rapidity gap. Such events were found to be rejected by requiring that 40 GeV $< \sum(E-P_z)+$ $2E_{tagger} < 70$ GeV, where $E-P_z$ is summed over the total hadronic final state. The distribution in both data and Monte Carlo is shown in figure 4.8 (b). All events in the largest $\Delta\eta$ bin were scanned visually for further background sources and none were found.

The complete set of analysis cuts is detailed in table 4.1.

4.3 Monte Carlo Models

The HERWIG 5.9 [44] Monte Carlo event generator was used to correct the data for detector acceptance and bin migration effects. HERWIG incorporates the BFKL LLA colour singlet exchange cross section for the elastic scattering of two partons as computed by Mueller & Tang [42]. For the elastic scattering of a pair of quarks, carrying momentum fraction x_i of beam particle i, in the asymptotic limit $x_\gamma x_h W^2 \gg -t$, the t distribution of the cross section $\hat{\sigma}$ is given by

$$\frac{\mathrm{d}\hat{\sigma}(qq \to qq)}{\mathrm{d}t} = (\alpha_s C_F)^4 \frac{2\pi^3}{t^2} \frac{e^{2\omega_0 Y}}{(7\alpha_s N_c \zeta(3) Y)^3} \tag{4.1}$$

where

$$Y = \ln\left(\frac{x_\gamma x_h W^2}{-t}\right)$$

and

$$\omega_0 = N_c \; 4 \ln 2 \; \frac{\alpha_s}{\pi}$$

N_c is the number of active colours, ζ is the Riemann zeta function and C_f is the colour factor. Y is the rapidity difference between the outgoing partons from the hard scatter. The values of α_s in equation (4.1) are free parameters in the LLA, and are chosen to be 0.23.[5] This corresponds to a choice of $\omega_0 = 0.61$.

A sample of standard HERWIG photoproduction events was also generated and combined with the BFKL sample in order to provide the best description of the data. In photoproduction interactions, the photon and the proton remnants are known to play an important role in the description of the energy flow between jets [46]. In HERWIG, remnant interactions can be simulated by the addition of soft processes underlying the hard scattering. The inclusive jet profiles (figures 4.4 and 4.6) and the energy flow between the jets (figure 4.7 (a)) are found to be best described when 20% of events contain an additional soft underlying process. This matches

[5]Note that only 2 of the 3 α_s values in equation (4.1) are actually independent, however. Both values in the fraction should be the same, whereas α_s in the pre-factor may take a different value.

the optimal mixture found for other recent H1 dijet studies [47]. All HERWIG simulations use the GRV-HO parton distributions for the photon and proton [48]

An important point should be made here about the use of Monte Carlo in correcting for detector effects. The generated, or 'hadron level' Monte Carlo sample is passed through a simulation of the H1 detector. This 'reconstructed' sample is then used to calculate the acceptance corrections which are applied to the final result (this process will be described in detail in section 4.4). It is certainly true that the HERWIG soft underlying event process has essentially no physical basis (better models are now becoming available, however [49]). It is also the case that the mechanism which causes any excess of rapidity gap events may not be the BFKL pomeron. This does not matter, however, for the correction process. The important point is that the reconstructed Monte Carlo sample accurately matches the uncorrected data distributions. The comparisons between the data and the reconstructed Monte Carlo sample are shown figures 4.4 to 4.8.

4.4 Acceptance and Efficiency Corrections

The gap fraction measured by the H1 apparatus includes the effects of finite detector acceptance and resolution which must be removed. Many of the acceptance effects, which are associated with the finite geometrical extent of the detector and the inefficiencies of individual detector components, will cancel, because the gap fraction is a ratio of two jet rates. The effect of the finite detector resolution, however, is more complicated. The gaps between jets measurement is effectively binned in 3 kinematic variables: the E_T of the two jets and the rapidity separation between the jets. The finite detector resolution will cause migrations into and out of each bin in $\Delta\eta$, across the jet E_T cuts, and into and out of the gap sample. These must be corrected for. The data are corrected using the smeared acceptance, calculated from

(a) (b)

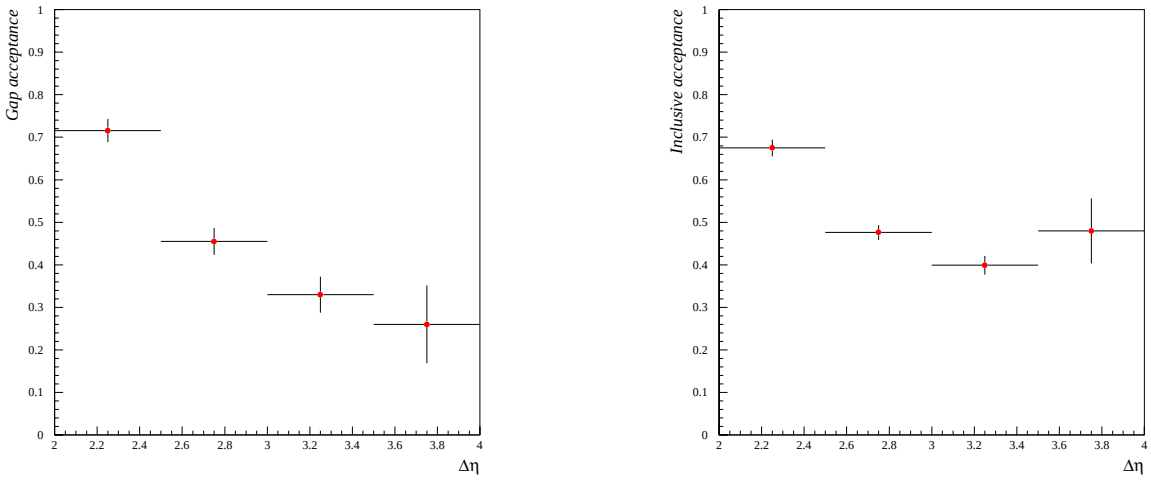

Figure 4.9: The smeared acceptance for the rapidity gap sample (a) and the inclusive sample (b)

Monte Carlo and defined as

$$A = \frac{N^r}{N^g} \tag{4.2}$$

where N^g is the number of events generated in a particular bin and N^r is the number of events reconstructed in that bin. This quantity is shown in figure 4.9 (a) for the inclusive sample and in figure 4.9 (b) for the gap sample. The ratio of these two smeared acceptances is used to correct the gap fraction, and is shown in figure 4.11 (b). The errors quoted on the acceptance, which are propagated through to the systematic error in this measurement, were estimated by dividing the sample into three independent samples as shown in figure 4.10. The 'gen+rec' sample are events which are generated and reconstructed in a bin, 'rec not gen' are events reconstructed in a bin which were not generated in that bin, i.e. migrations into the bin, and 'gen not rec' are events which were generated in a bin which are not reconstructed in that bin, i.e. migrations out of the bin. In this notation, the smeared acceptance can be written as

$$A = \frac{gr + r}{gr + g} = \frac{\sum_{gr} W_{gr} + \sum_r W_r}{\sum_{gr} W_{gr} + \sum_g W_g} \tag{4.3}$$

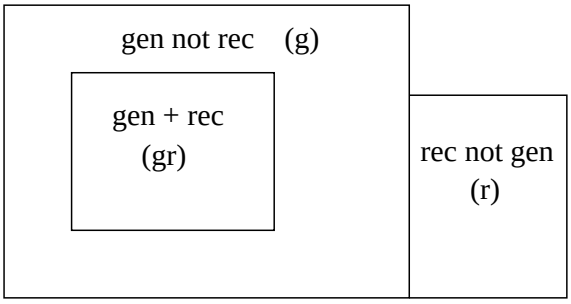

Figure 4.10: The three independent samples used in the calculation of the smeared acceptance

where W_x is the weight of the event in sample x. Hence the error on the acceptance can be written

$$\sigma^2(A) = \sum_{gr} \left(\frac{\partial A}{\partial W_{gr}} \right)^2 \sigma^2(W_{gr}) + \sum_{r} \left(\frac{\partial A}{\partial W_r} \right)^2 \sigma^2(W_r) + \sum_{g} \left(\frac{\partial A}{\partial W_g} \right)^2 \sigma^2(W_g) \quad (4.4)$$

where

$$\sigma^2(x) = \sum_{x} W_x^2 \quad (4.5)$$

Figure 4.11 (a) shows the bin purity. This quantity is defined as the fraction of events in a bin after detector simulation which were in the bin at the hadron level. The purity in the highest $\Delta\eta$ bin is seen to be particularly poor. The purity falls with increasing $\Delta\eta$ because events with a large rapidity difference between the jets necessarily have both jets towards the edges of the LAr (in the forward direction) and SPACAL (in the backward direction) calorimeters, where the jet energy resolution becomes poor. The origin of the low purities is migrations across the jet E_T cuts, not the important $\Delta\eta$ cut. The jet E_T migrations are of course the same for both the gap and the inclusive sample, and do not therefore affect the gap fraction as a function of $\Delta\eta$. This means that, whilst such a low purity should be cause for concern, the actual measurement presented in figure 4.12 is not meaningless. This problem was overcome in the measurement of chapter 6, and is discussed in section 6.7.2.

(a) (b)

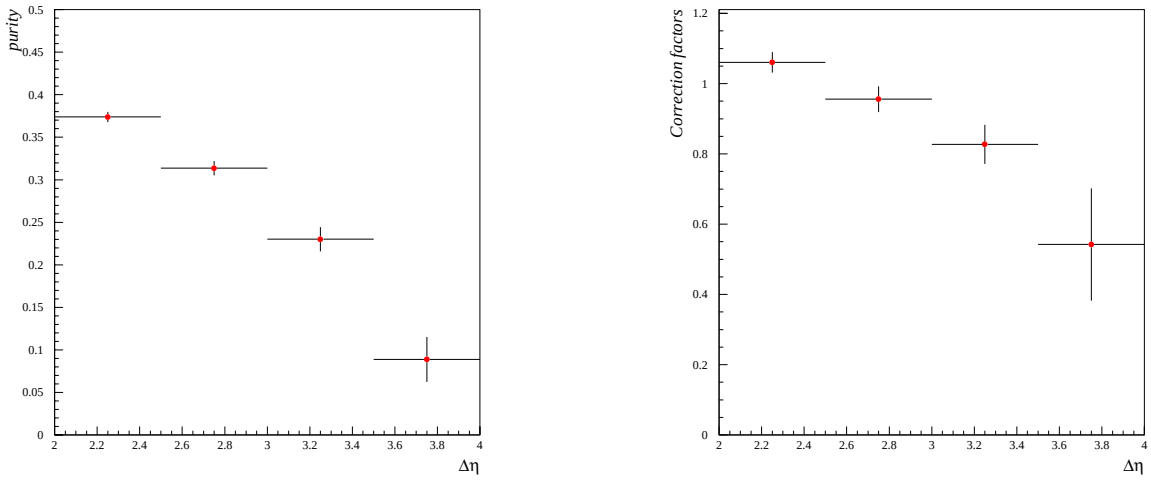

Figure 4.11: The purity for the inclusive sample (a) and the ratio of the gap and inclusive smeared acceptances (b)

4.5 Evaluation of Errors

The statistical error on each point is determined by the number of events in the sample.

Systematic errors are estimated on a bin by bin basis and added in quadrature. The first group of errors originates from the uncertainty in the energy scales of the detectors. They are estimated by varying the energy scale by the known uncertainty and recalculating the gap fraction. The percentage change in the gap fraction in each bin is then the systematic error in that bin. The energy scale uncertainties in the relevant detectors are:

- Liquid Argon Calorimeter Energy Scale
  The hadronic energy scale of the LAr Calorimeter is known to 4%
- SPACAL Calorimeter Energy Scale
  The hadronic energy scale of the SPACAL Calorimeter is known to 10%

The major contribution to the systematic error was from the limited Monte Carlo statistics used to calculate the smeared acceptance. The error was estimated as described in section 4.4. [6]

4.6 The Gap Fraction

The gap fraction, corrected to the case in which there is no hadron in the rapidity region between the jets with energy greater than 400 MeV, is shown in figure 4.12. Also shown is the prediction from standard photoproduction (direct and resolved contributions) using the HERWIG Monte Carlo event generator. Within the errors, the data are well described without any colour singlet exchange contribution throughout the region $2.0 < \Delta\eta < 3.5$, whereas an excess of events with a rapidity gap between the jets is observed for $3.5 < \Delta\eta < 4.0$. Integrated over this latter interval, the measured value of $f(\Delta\eta)$ lies more than two standard deviations above the prediction of the simulation without a colour singlet exchange contribution.

In order to check that the observed excess at large $\Delta\eta$ of events with rapidity gaps between the jets is not dependent on the definition of the gap fraction, the analysis has also been performed with a number of slightly different gap definitions. The maximum hadron energy between the jets was varied between 350 MeV and 450 MeV. The effective cone radius was increased from 1.0 to 1.1, allowing particles to escape from the edges of the jet cones without destroying the rapidity gap. These changes were found to affect the overall normalisation of the $f(\Delta\eta)$ distribution by up to 25% without significantly affecting the shape. The conclusion that a colour singlet exchange is required in the large $\Delta\eta$ region is therefore not affected by the details of the definition of the gap between the jets.

[6] This error could of course be easily reduced. The reasons for not pursuing this analysis method will be discussed in section 4.7

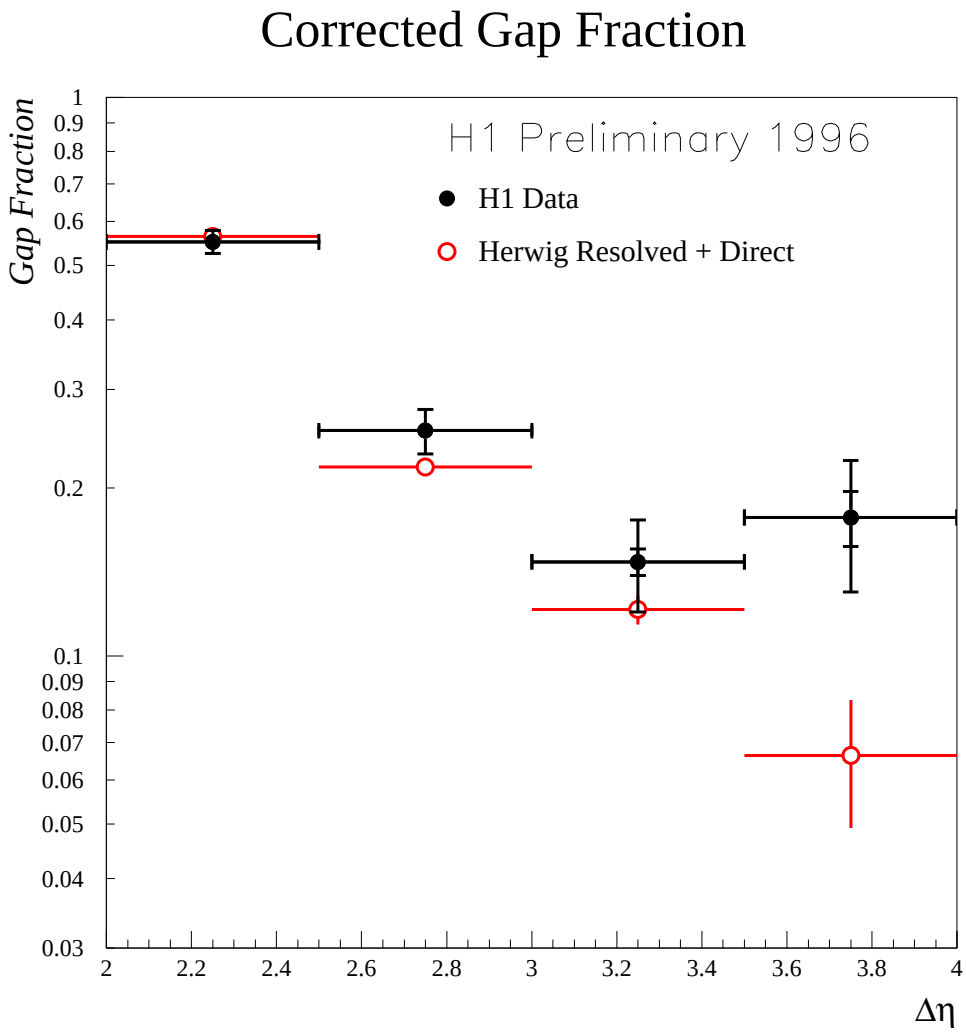

Figure 4.12: The corrected gap fraction $f(\Delta\eta)$. H1 data are solid points. The inner error bars show the statistical errors and the outer error bars show the sum in quadrature of the statistical and systematic errors. The prediction of the HERWIG simulation without a colour singlet exchange component is shown, together with statistical errors, as the open points.

4.7 Discussion

Whilst the gap fraction shown in figure 4.12 shows a signal for an excess of rapidity gap events in the largest $\Delta\eta$ bin, the results are far from conclusive. The difficulties posed by jet finding at the edges of the detector result in poor bin purities and therefore large uncertainties in the quantitative features of the measurement. More importantly, the largest accessible gap size is limited by the requirement that two jets are completely contained within the detector. Since the rapidity coverage of the main H1 calorimeters is ~ 7 units of rapidity, and the jet cones have a diameter of 2 units of rapidity, there is an 'in principal' limit on the size of the observable rapidity gap between the jet centres of $\Delta\eta \sim 5$, corresponding to an actual gap in rapidity between the edges of the two hadronic systems of ~ 3. This is a severe limitation for both theoretical and experimental reasons. The key feature in the LLA BFKL cross section (equation (4.1)) is the exponential rise with Y, the rapidity separation of the outgoing partons from the hard scatter. This means that, in order to access the interesting physics and really test the theory, data must be collected with the largest possible rapidity gaps.[7] The two jet requirement severely restricts the accessible rapidity reach, and therefore restricts access to the most interesting rapidity region. [8] Experimentally, rapidity gaps of less than 2 units of rapidity between the jet edges are difficult to identify correctly (see the discussion in section 6.5.4), again resulting in low bin purities due to mis-identified gap events. Furthermore, the requirement of two jets with $E_T > 4.5$ GeV (jet finding becomes unreliable below this energy) restricts the measurable t range to $|t| \geq 20$ GeV^2, which imposes a severe restriction on the available statistics. pQCD calculations are expected to hold down to $|t| \sim 1$ GeV^2, and therefore the experimental goal should be to gather data as low in $|t|$

[7] The need for this test is all the more pressing given the recent next to leading log BFKL calculations which suggest very large corrections to the leading order result [30]

[8] Similar conclusions were reached by the H1 workshop study of Butterworth et. al. [50]. after the ZEUS collaboration rapidity gaps between jets measurement

as possible. Given these restrictions, however, it is still true that the rapidity gaps between jets approach has given a first glimpse of the very high t diffractive process.

The restrictions on accessible gap size and the experimental difficulties associated with jet finding strongly suggest that a new approach to the observation of high t diffraction is necessary. In the following chapter, a new approach is presented which avoids all of the above problems.

Perhaps the most interesting observation to be made comes from a comparison of the gap fractions measured at HERA in γp collisions, by both the ZEUS and H1 (this thesis) collaborations [51], and in pp collisions by the D0 and CDF collaborations at the TEVATRON [52] [53]. The HERA measurements both show a gap fraction of order 10% in the highest $\Delta\eta$ bin, whereas the TEVATRON results show a gap fraction of order 1% at centre of mass energy 1800 GeV, and $\sim 3\%$ at 630 GeV. This difference is certainly related to the issue of gap survival probability; the fact that events in which a colour singlet object is exchanged may not have a rapidity gap in the hadronic final state due to additional soft or hard interactions between the beam remnants which cause the gap to be destroyed. This effect may also be responsible, or a contributing factor to, the apparent breakdown of diffractive factorisation between HERA and the TEVATRON; diffractive parton distribution functions and pomeron flux factors extracted at HERA in the diffractive DIS process described in section 3.5 give incorrect results when applied to TEVATRON measurements [54]. Models of gap survival are at present in their infancy, but the comparison provided by the gaps between jets measurements is generating much theoretical and phenomenological interest [55].

Chapter 5

Double Diffraction Dissociation at Large $|t|$

5.1 Introduction

It is possible to avoid many of the drawbacks discussed in the previous chapter by studying the more inclusive process where the incoming beam particles each dissociate, producing systems X and Y which are far apart in rapidity, in the presence of a large momentum transfer. The gaps between jets process forms a subset of this measurement.

The hadronic final state is split by the largest rapidity gap in the event into two hadronic systems X and Y as shown in figure 5.1. In terms of the jet measurement, system X is the backward, or photon side jet and Y is the forward or proton side jet. The scattered electron is tagged in the electron tagger, limiting Q^2 to < 0.01 GeV^2. The entire kinematics of the event are constrained by the measurement of the scattered electron (giving the 4-vector of the photon) and the 4-vector of the X system, which at HERA is boosted into the detector and hence well measured. This method has the advantage that the Y system can now be allowed to move completely outside

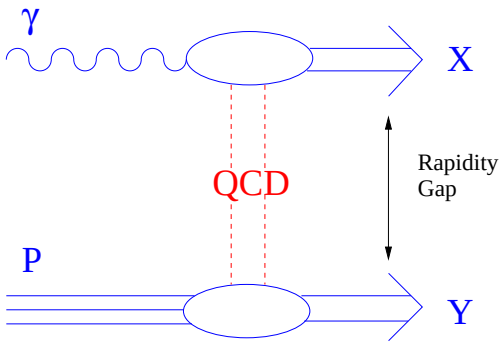

Figure 5.1: The double diffraction dissociation process.

the detector, since the event kinematics are constrained without it, increasing the largest accessible gap size to over seven units of rapidity. Notice that the gap size, $\Delta\eta$, is not a measured variable in this approach. The largest gap in the event is used only to define the systems X and Y, i.e. all particles backward of the gap go into system X and all those forward of the gap go into system Y. Events with gaps are characterised by $M_X, M_Y \ll W$ and so a large rapidity gap sample is selected by insisting that $M_Y \leq M_{Y\,\mathrm{cut}}$. This way of defining the sample has the very important advantage that it is easy to implement theoretically and is quite insensitive to hadronisation effects which define the edges of the systems X and Y. This procedure has been used before in the H1 $F_2^{D(3)}$ analysis [13] described in section 3.5.

In section 5.2, the relevant cross section formulae are derived. Section 5.3 contains a Monte Carlo analysis of the proposed measurement in order to examine issues relating to non-colour-singlet exchange and possible non-perturbative effects. The chapter ends with a discussion of gap survival effects in relation to this measurement.

5.2 Kinematics and the Double Dissociation Cross Section

Let q_μ be the four-momentum transfer across the rapidity gap. It has the following Sudakov decomposition:

$$q_\mu = \beta P_\mu + \alpha Q_\mu + q_{t,\mu}$$

where P and Q label the four-momenta of the incoming proton and photon. (It is assumed that $P^2 = Q^2 = 0$.) In the Regge limit, $t \equiv q^2 \approx q_t^2$ [1] and hence

$$\begin{aligned} M_X^2 &\approx t - \beta W^2 \\ M_Y^2 &\approx t + \alpha W^2 \end{aligned} \tag{5.1}$$

where $W^2 = (P+Q)^2 = 2P \cdot Q$.

Now, in the limit $-t \gg \Lambda^2_{\mathrm{QCD}}$ the long distance physics can be factorised into parton distribution functions and it may be assumed that the rapidity gap is produced by a single elastic parton-parton scattering, i.e.

$$\frac{d\sigma(\gamma p \to XY)}{dx_\gamma dx_h dt} = F_\gamma(x_\gamma, -t) F_p(x_h, -t) \frac{d\hat{\sigma}(qq \to qq)}{dt} \tag{5.2}$$

where $F_i(x,\mu^2) = \frac{9}{4} g_i(x,\mu^2) + \Sigma_i(x,\mu^2)$ is a colour weighted sum over gluon and quark parton density functions for beam particle i. The fraction of the beam momentum carried by the struck parton is x and μ is the factorisation scale. The perturbative QCD dynamics lies in the cross-section for elastically scattering a pair of quarks: $d\hat{\sigma}(qq \to qq)/dt$. In the leading logarithm approximation, this is given by exchanging a pair of interacting reggeised gluons [29]. In the asymptotic limit $x_\gamma x_h W^2 \gg -t$, the cross-section can be computed analytically [42] (this equation has already been discussed in section 4.3):

$$\frac{d\hat{\sigma}(qq \to qq)}{dt} = (\alpha_s C_F)^4 \frac{2\pi^3}{t^2} \frac{e^{2\omega_0 Y}}{(7\alpha_s N_c \zeta(3) Y)^3} \tag{5.3}$$

[1] Note that in the Regge limit $\alpha\beta W^2$ may be neglected, since $\alpha \sim \frac{1}{W^2}$ and $\beta \sim \frac{1}{W^2}$

where

$$Y = \ln\left(\frac{x_\gamma x_h W^2}{-t}\right)$$

and

$$\omega_0 = N_c\ 4\ln 2\ \frac{\alpha_s}{\pi}.$$

An alternative model for the gap producing mechanism is to assume that two massive gluons are exchanged, in which case

$$\frac{d\hat{\sigma}(qq \to qq)}{dt} = \frac{\pi}{16t^2}\alpha_s^4 \frac{1}{\Delta^2}\ln^2\frac{\Delta+1}{\Delta-1}, \tag{5.4}$$

where

$$\Delta = (1 - 4M^2/t)^{1/2} \tag{5.5}$$

and M is the gluon mass. The incoming partons are collinear with the beam particles whilst, after the scatter, they carry transverse momentum $\sqrt{(-t)}$. These partons are the seeds of the jets which are produced in the gaps between jets measurement. Putting these outgoing partons on shell gives

$$\begin{aligned} x_\gamma = \frac{-t}{-\beta W^2} &= \frac{-t}{\tilde{M}_X^2} \\ x_h = \frac{-t}{\alpha W^2} &= \frac{-t}{\tilde{M}_Y^2}. \end{aligned} \tag{5.6}$$

with the definitions $\tilde{M}_X^2 \equiv M_X^2 - t$ and $\tilde{M}_Y^2 = M_Y^2 - t$. These kinematic relations between the parton momentum fractions and the physical observables lead to

$$\tilde{M}_X^2\tilde{M}_Y^2\frac{d\sigma}{\tilde{M}_X^2\tilde{M}_Y^2} = x_\gamma x_h \frac{d\sigma}{dx_\gamma dx_h}.$$

For the purposes of this study, it is assumed that M_Y is confined to be smaller than some value. Recall that the Regge limit demands that $W \gg M_X, M_Y$ and hence that there be a rapidity gap between the systems X and Y (This kinematic method of forcing a large rapidity gap will be discussed in some detail from an experimental point of view in chapter 6).[2] In particular for this study, $M_Y < 10$ GeV.

[2]The rapidity gap between systems X and Y is equal to $\ln(x_\gamma x_h W^2/(-2t))$.

The variable $x_{I\!P}$ is introduced (recall its use in the low t region in section 3.5)

$$x_{I\!P} \equiv -\beta = \frac{\tilde{M}_X^2}{W^2} \tag{5.7}$$

In which case

$$\frac{d\sigma(\gamma p \to XY)}{dx_{I\!P} dt} = \frac{1}{t^2} \int dM_Y^2 \; (x_\gamma x_h W)^2 F_\gamma(x_\gamma, -t) F_p(x_h, -t) \frac{d\hat{\sigma}(qq \to qq)}{dt}. \tag{5.8}$$

Sitting at fixed M_X^2 and t the $x_{I\!P}$ dependence is determined completely by the hard partonic scattering. For example, if

$$\frac{d\hat{\sigma}(qq \to qq)}{dt} \sim e^{2\omega_0 Y} \tag{5.9}$$

then

$$\frac{d\sigma(\gamma p \to XY)}{dx_{I\!P} dt} \sim \left(\frac{1}{x_{I\!P}}\right)^{2\omega_0 + 1}. \tag{5.10}$$

Alternatively, one can look at the $x_{I\!P}$ dependence at fixed W and t. In which case the $x_{I\!P}$ dependence is dependent upon the photon parton densities, i.e. if the hard scatter is given by (5.9) then it follows that

$$\frac{d\sigma(\gamma p \to XY)}{dx_{I\!P} dt} \sim \left(\frac{1}{x_{I\!P}}\right)^{2\omega_0 + 2} F_\gamma(x_\gamma, -t) \tag{5.11}$$

where $x_\gamma = -t/(x_{I\!P} W^2)$. In figure 5.2 the massive gluon and BFKL calculations of the γp cross-section are compared (all the cross-sections shown will be for γp interactions). For the massive gluon calculation, a gluon mass of 800 MeV is chosen. Decreasing the mass causes the cross-section to rise (it diverges at zero mass) but does not affect the shape of the $x_{I\!P}$ distribution; it remains significantly flatter than the BFKL calculation. The cross-sections are shown for two different values of the parameter α_s. Increasing α_s steepens the BFKL distribution (since $\omega_0 \sim \alpha_s$) but only affects the normalisation of the massive gluon distribution.

For all the plots in this chapter, $-t > 4$ GeV^2 and $M_Y < 10$ GeV. Unless otherwise stated, all results are derived at fixed $W = 250$ GeV using the BFKL calculation with $\alpha_s = 0.23$ and using the GRV-G HO parton distribution functions

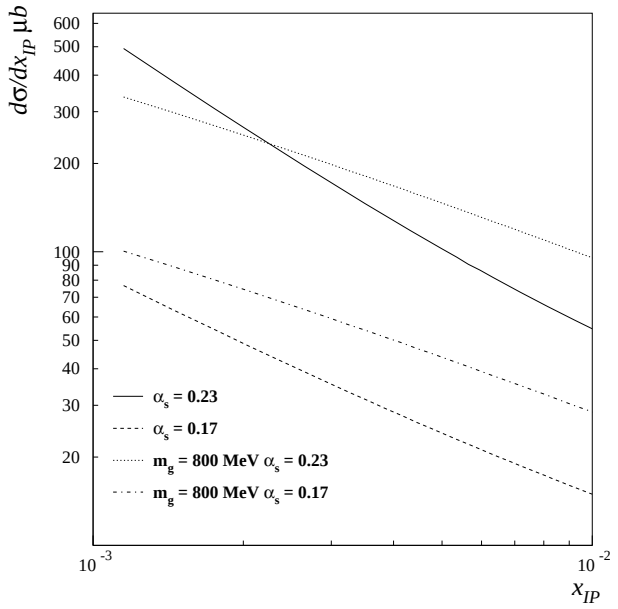

Figure 5.2: Comparison of the BFKL (solid and dashed lines) and massive gluon (dotted and dashed-dotted lines) predictions.

of the photon [58] and the GRV 94 HO DIS proton parton density functions [59] as implemented in PDFLIB [60]. In figure 5.3 the effect of varying the photon parton density functions [58, 61–63] is shown. Note that the primary effect of varying the photon parton density functions is to shift the normalisation. In fact, for the BFKL calculation, the $x_{I\!P}$ behaviour is quite close to $\sim (1/x_{I\!P})^{2\omega_0}$ independent of the photon parton density function (compare this with the expectation of (5.11)). Note that changing the proton parton density functions does not affect the shape of the $x_{I\!P}$ distribution, since x_h depends only upon t and M_Y.

5.3 Monte Carlo Simulation

The HERWIG Monte Carlo generator is used to generate 2.5 pb^{-1} of ep data with the photon energy fraction, y, in the range $0.28 < y < 0.65$. This range in y corresponds to $\langle W \rangle \approx 200$ GeV and is the same as that used in the previous chapter

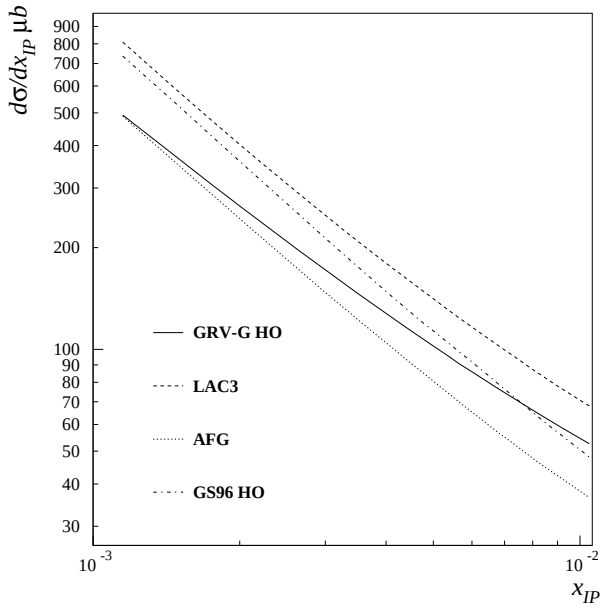

Figure 5.3: Effect of varying the photon parton density functions.

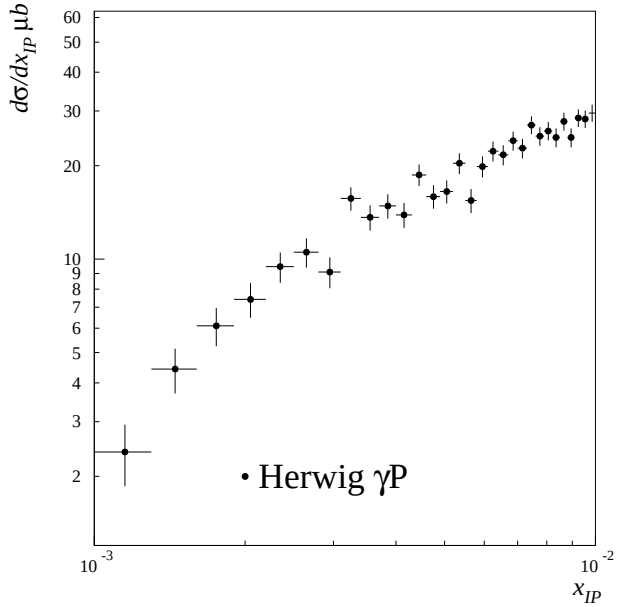

Figure 5.4: The $x_{I\!P}$ distribution of the background due to non-colour-singlet exchange.

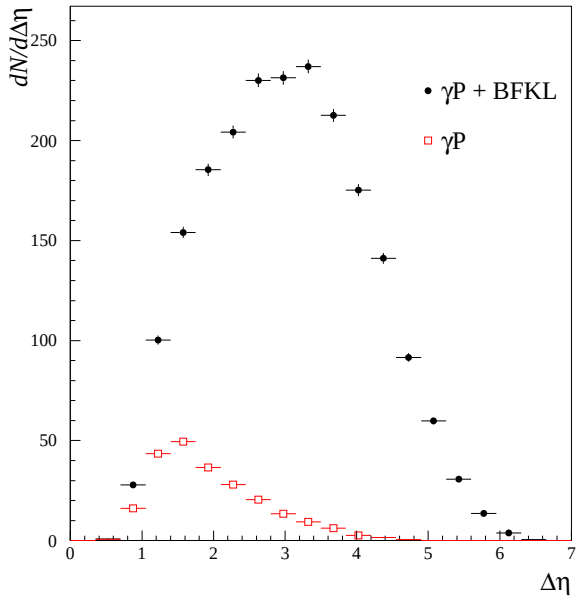

Figure 5.5: Distribution of events in rapidity.

for the gaps between jets analysis. For each event with a tagged electron, the largest rapidity gap in the event is sought and this is used to define the systems X and Y. The kinematic cuts described in the previous section are then applied.

In figure 5.5 the distribution of events as a function of the rapidity gap is shown (only events which have $10^{-3} < x_{I\!P} < 10^{-2}$ are included). Those events which originate from non-colour-singlet exchange processes are also shown and can be seen to constitute a small fraction of the total. This effective depletion of the non-colour-singlet exchange contribution arises directly as a consequence of insisting that $M_Y < 10$ GeV and $10^{-3} < x_{I\!P} < 10^{-2}$, i.e. that $M_X, M_Y \ll W$. In particular, no rapidity gap cut is needed to select rapidity gap events. Since the system Y is not required to be in the detector, it is now possible to select events with very large gaps. Also, since jet finding is no longer necessary, many more events enter the sample than entered the gaps between jets measurement (this arises primarily because most events lie at the lowest values of $-t$). The magnitude of the gain in both statistics and reach in rapidity should be emphasised. In particular, note

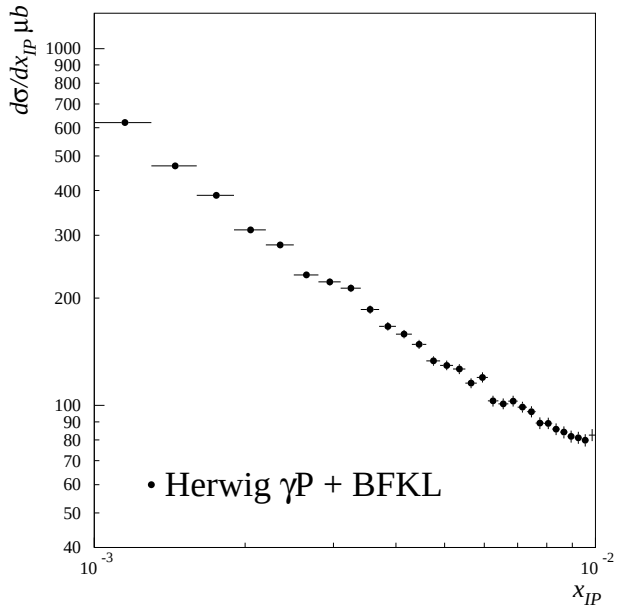

Figure 5.6: The $x_{I\!P}$ distribution at fixed W.

that the gaps between jets data populate the $\Delta\eta < 2$ region and that, even in this restricted region, they constitute only a small fraction of the total number of events.

In figure 5.6 the $x_{I\!P}$ distribution at fixed W is shown. The errors are typical of the statistical errors to be expected from analysis of 1996 HERA data. The small contribution from non-colour-singlet exchange processes is included. This is shown separately in figure 5.4 and, as expected, it falls away exponentially as $x_{I\!P}$ falls. In figure 5.7 the theoretical calculation is compared with the output from HERWIG at $W = 250$ GeV. The open circles correspond to the cross-section obtained when t is constructed at the level of the hard scatter, i.e. it is the t of the hard BFKL subprocess. Of course this value of t should be unique and equal to the value extracted by summing the four-momenta of all outgoing hadrons in system X and subtracting from the four-momenta of the incoming photon. The solid circles in figure 5.7 show the effect of reconstructing t at the hadron level and clearly there is a significant shift relative to the hard scatter points (which agree well with the theoretical calculation). The squares denote the cross-section obtained by computing

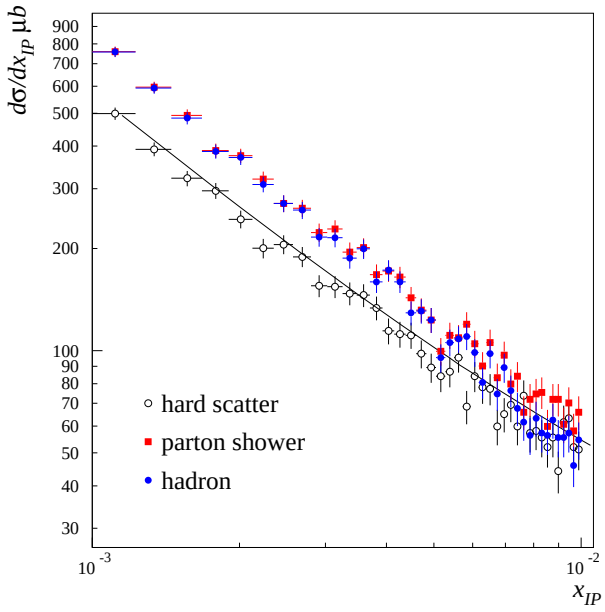

Figure 5.7: Comparison of theory (solid line) with the Monte Carlo output from HERWIG.

t after parton showering but before hadronisation. The fact that the reconstructed t values are not all the same is clearly demonstrated in figure 5.8. The number of events is plotted as a function of the difference in t between the value extracted after parton showering, t_{ps}, and the value obtained from the hard scatter, t_{hs}. Note that there is no shift in t for those events labelled 'valence'. These are events in which the parton entering the hard scatter from the proton is either an up or a down quark and from the photon is not a gluon. All other events are in the 'non-valence' sample and it is here that the systematic shift to larger values of $-t$ is seen, i.e. $-t_{ps} > -t_{hs}$. This shift is a consequence of the way HERWIG develops the final state from the seed partons in the hard scatter. In particular, since HERWIG generates the complete final state it necessarily has some model for the photon and proton remnants. For the proton, it will always evolve backwards from the hard scatter to a valence quark, whereas for the photon evolution terminates with a quark–anti-quark pair. Hence, in the 'non-valence' sample at least one parton must be emitted off an incoming

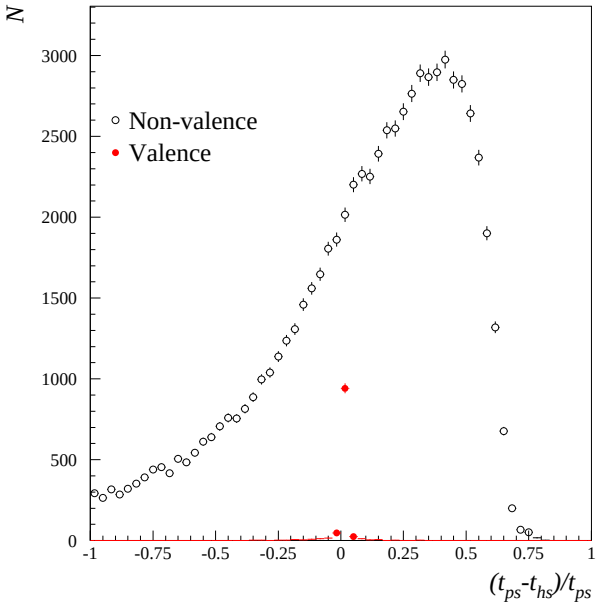

Figure 5.8: Deviation of the reconstructed t from the true value.

parton. This is the source of the shift in t.

A shift to large $-t$ has the immediate consequence of systematically shifting the $x_{I\!P}$ distribution to the right, as is clearly seen in figure 5.7. This is easy to see since $x_{I\!P} = (M_X^2 - t)/W^2$, so events which are generated with some t_{hs} are reconstructed, after parton showering, to have a larger $-t$ and hence larger $x_{I\!P}$. In essence therefore, the difference between the theory and hadron level results can be attributed to non-perturbative effects. The primary feature of the effect is to systematically shift the $x_{I\!P}$ distribution without significantly affecting its shape.

5.4 Discussion

In this chapter a new way of studying short distance diffraction has been developed. Although the approach has focused primarily on HERA, it may also be possible to carry out such a measurement at the TEVATRON, although the advantage of the

asymmetric beam energies is of course lost.

Again, the issue of gap survival is important and may be studied within this framework. The $x_{I\!P}$ at fixed M_X and $x_{I\!P}$ at fixed W distributions will provide complementary information. Most of the phenomenology in this chapter (and the subsequent measurement presented in the following chapter) has focused on the $x_{I\!P}$ distribution at fixed W where gap survival effects are expected to affect the overall normalization but not the shape since the gap survival probability is expected to depend primarily on the centre-of-mass energy, e.g. see [64]. Theoretically one expects a decrease of gap survival with increasing centre-of-mass energy since the probability for secondary partonic interactions, which would destroy the gap, increases as the number density of partons increases and since the parton density is largest at small x, i.e. high W [49]. In addition the data on the gaps between jets process analysed by the TEVATRON ($\sqrt{s}$ = 630 and 1800 GeV) [53] and the HERA ($\sqrt{s} \approx 200$ GeV) [51] collaborations discussed in section 4.7 also suggest a strong decrease of the gap survival probability with increasing centre-of-mass energy. With sufficient statistics, therefore, any difference in the slopes of the $x_{I\!P}$ at fixed M_X and the $x_{I\!P}$ at fixed W distributions, other than that from trivial kinematics, should provide information on the gap destruction process.

Chapter 6

The Double Dissociation Cross Section at Large $|t|$

6.1 Introduction

In the previous chapter a new framework for the analysis of high $|t|$ diffraction was developed. In this chapter the first experimental realisation of this approach is presented, in the form of the double dissociation differential cross section $\mathrm{d}\sigma/\mathrm{d}x_{I\!P}(\gamma P \to XY)$ at fixed W.

6.2 The Choice of kinematic Variables

As discussed in the previous chapter, the double dissociation process shown in figure 5.1 is fully described by the differential cross section $d^4\sigma/(dWdt\ dM_X dM_Y)$. It is also shown that the natural variable for the process, in terms of making contact with the pQCD elastic parton-parton scattering calculation of Mueller & Tang [42], is $x_{I\!P}$. From the experimentalists standpoint, the choice of the kinematic variables

and kinematic range in which to measure the cross section must be made on the basis of experimental resolution, i.e. what variables are well measured, and in what range? Fortunately, it is $x_{I\!P}$ again which proves to be the appropriate variable from an experimental standpoint. $x_{I\!P}$ is defined in terms of the Sudakov co-efficient β in equation (5.7). An equivalent definition can be given in terms of the four vectors of the photon, proton, X and Y systems γ, P, X and Y respectively;

$$x_{I\!P} = \frac{\gamma.(P-Y)}{\gamma.P} = \frac{Q^2 + M_X^2 - t}{Q^2 + W^2 - m_p^2} \simeq \frac{M_X^2 - t}{W^2} \tag{6.1}$$

where Q^2 is the virtuality of the photon, here restricted to be < 0.01 GeV^2 and m_p is the proton mass, both of which can be neglected. A further simplification is now possible, since

$$t = (\gamma - X)^2 \simeq M_X^2 - 2(\gamma.X) = M_X^2 - 2E_\gamma \Sigma(E + p_z)_X \tag{6.2}$$

where E_γ is the energy of the photon, and $\Sigma(E + p_z)_X$ is summed over all hadrons reconstructed backward of the largest rapidity gap in the event. This quantity has the property that it is insensitive to losses down the beam pipe, for which $E \simeq -p_z$. Using equations (6.1) and (6.2)

$$x_{I\!P} \simeq \frac{\Sigma(E + p_z)_X}{2E_p} \tag{6.3}$$

where E_p is the proton beam energy. Figure 6.1 (a) shows the correlation between the reconstructed and generated values of $x_{I\!P}$ in the HERWIG simulation (to be described in detail in section 6.4). It is particularly well reconstructed for all values in the measurement. This is due to the large Lorentz boost of the CMS system, which draws the X system into the main calorimeters, as discussed in the previous chapter, coupled with the insensitivity to losses down the beam pipe of the reconstruction method described above.

The same $\Sigma(E + p_z)$ structure, which enables a good reconstruction of $x_{I\!P}$, can be exploited in the measurement of the Y system, by introducing the analogous $y_{I\!P}$

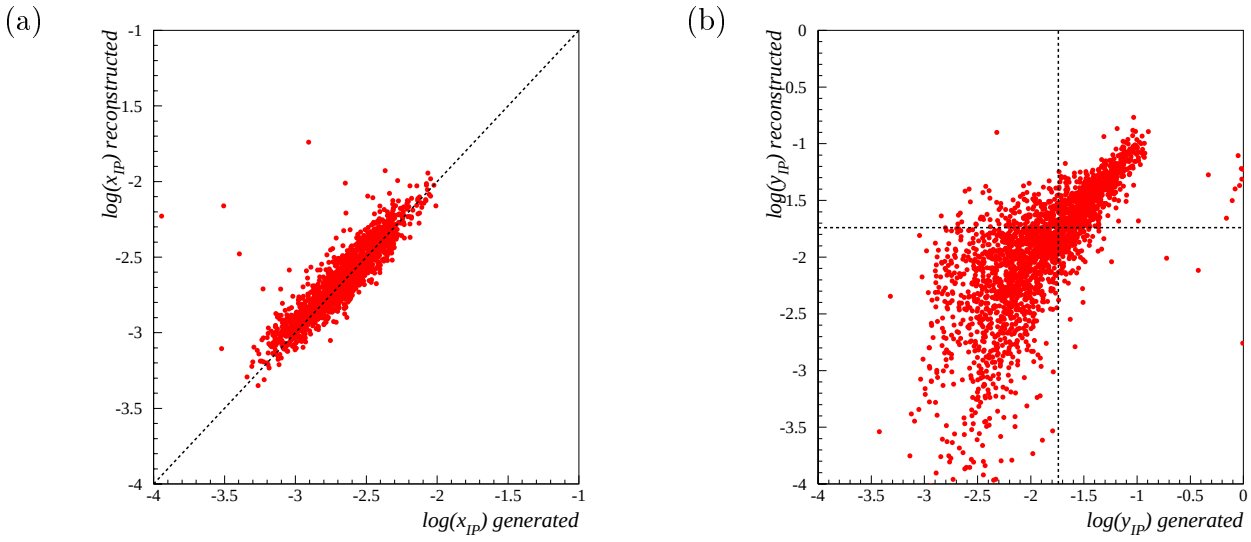

Figure 6.1: Correlation between reconstructed and generated values of (a) $x_{I\!P}$ and (b) $y_{I\!P}$ in the HERWIG simulation. The dashed lines in (b) show the position of the kinematic cuts.

variable;

$$y_{I\!P} = \frac{P.(\gamma - X)}{\gamma.P} \simeq \frac{M_Y^2 - t}{W^2} \tag{6.4}$$

This expression can similarly be simplified to

$$y_{I\!P} \simeq \frac{\Sigma(E - p_z)_Y}{2E_\gamma} \tag{6.5}$$

where now $\Sigma(E - p_z)_Y$ is summed over all hadrons forward of the largest rapidity gap in the event. Again, due to the change of sign, this quantity is insensitive to losses down the forward beam pipe, for which $E \simeq +p_z$. With the 'Y system' variable redefined in this way, the measured hadron level cross section is simply defined for $y_{I\!P} < y_{I\!P\,cut}$ rather than for $M_Y < M_{Y\,\mathrm{cut}}$ as in the previous chapter. Figure 6.1 (b) shows the correlation between the reconstructed and generated values of $y_{I\!P}$ in the HERWIG simulation. In this case, the Lorentz boost of the CMS system is disadvantageous, and measurements corresponding to low values of M_Y are not possible. For these events, however, the reconstructed $y_{I\!P}$ tends to underestimate the true value, and such events therefore do not migrate out of the sample. For larger

values of $y_{I\!P}$ an accurate reconstruction becomes possible. This effect must be taken into account in defining the $y_{I\!P}$ range for which to measure the cross section, and will be discussed in detail in section 6.5.

The double dissociation cross section of this study is therefore presented in terms of the 4 kinematic variables $x_{I\!P}$, $y_{I\!P}$, t and W

6.3 Event Selection

6.3.1 Selection of Minimally Biased Photoproduction Events

The data sample used for this analysis is the same as that used in the Rapidity Gaps Between Jets analysis of chapter 4, i.e. the 1996 sample. As before, events are selected in which the scattered positron is detected in the electron tagger. In the case of this analysis, however, a cross section measurement is being made and therefore much closer attention must be paid to the triggering of the events and the acceptance of the electron tagger. Also, since this analysis has a rather less well defined topological signature than in the case of the dijet sample, it will turn out that non-ep background is more of a problem, and more careful cuts are necessary.

6.3.2 The Trigger

The H1 trigger has been described in section 2.8. For the purposes of this analysis, the most important property of the events is that they have an electron in the 33m tagger. The efficiency of this part of the trigger is well known, and included in the acceptance curve shown in figure 4.3. An electron in the tagger is not sufficient for an event to be written directly to tape at H1, however, since the rate would be prohibitively high. Two different subtriggers were used to keep the events in this analysis, one based on tracking and vertex requirements, hereafter called the track

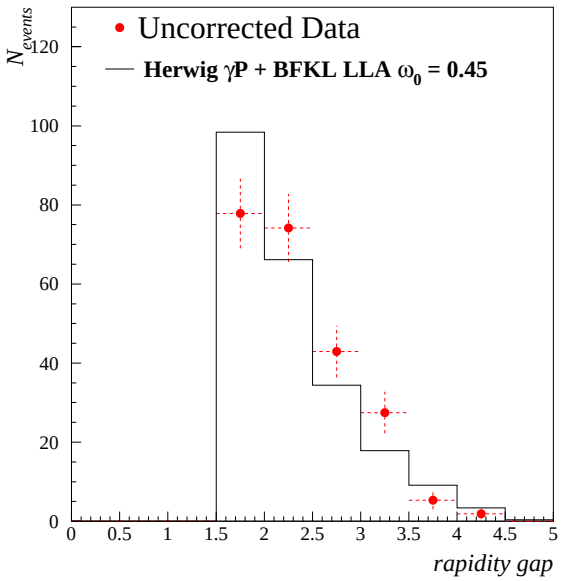

Figure 6.2: The rapidity gap between the edges of the X and Y systems.

trigger, and the other on energy deposited in the SPACAL calorimeter, hereafter called the spacal trigger [1]. If either of the subtriggers fired, the event was used. Both require an electron in the tagger. In addition, the track trigger requires a well reconstructed z-vertex and at least 3 charged tracks flagged by the $DCRPh$ trigger element, and the spacal trigger requires a hit in the electromagnetic spacal, flagged by the $SPCLe$ trigger element (see section 2.8). Only runs in which both subtriggers were not prescaled are used in this analysis. This results in a final data sample of 121 events (after all cuts and background removal, see section 6.6), corresponding to an integrated luminosity of 6.7 pb^{-1}. The large gain in statistics over the gaps between jets analysis of chapter 4 should be emphasised. All the events in this data sample have rapidity gaps between the edges of the X and Y systems of at least 1.5, shown in figure 6.2 (see section 6.5.4). The events would therefore all populate

[1] In H1 terminology, the track trigger is s83 and the spacal trigger is s50

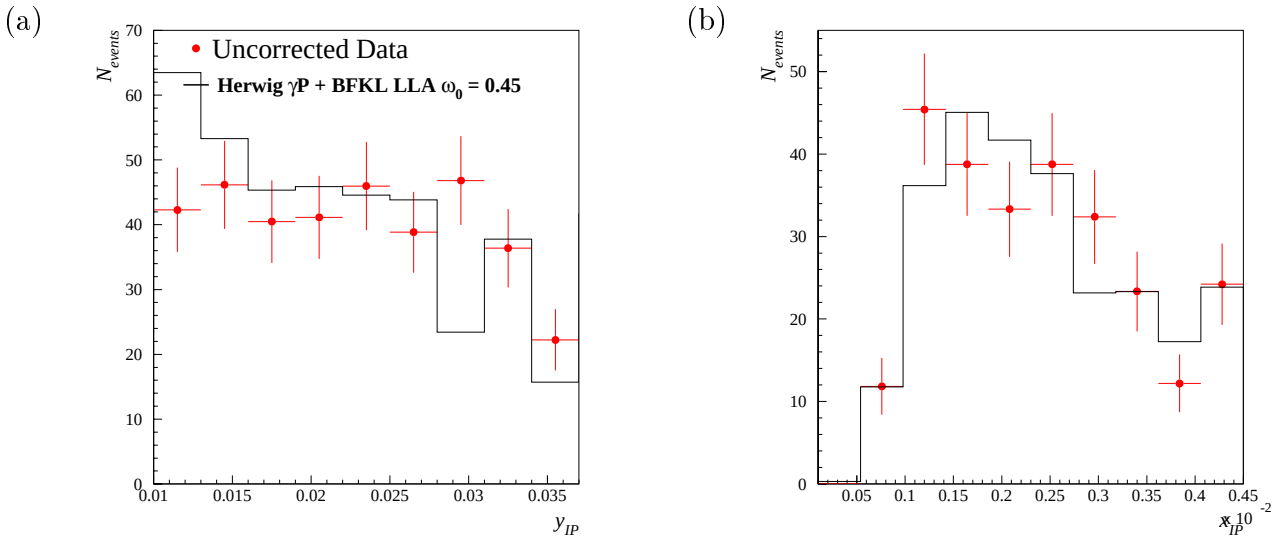

Figure 6.3: Comparison between H1 data and HERWIG generator distributions of (a) $y_{I\!P}$ and (b) $x_{I\!P}$.

the $\Delta\eta > 3.5$ region in figure 4.12, which contains only 21 gap events [2].

6.4 Monte Carlo Simulation

In setting the kinematic range for the cross section measurement, as well as correcting the data for detector effects, the Monte Carlo techniques described in chapter 4 for the rapidity gaps between jets analysis are again employed. As before, it is essential that the Monte Carlo sample used for the analysis describes the data as closely as possible. In this section, after describing the Monte Carlo sample used, generated distributions in the relevant kinematic quantities are compared with data.

[2]Recall that in the gaps between jets analysis, $\Delta\eta$ is defined between the jet centres. Since the jet cones have a radius of 1 unit of rapidity, $\Delta\eta = 3.5$ corresponds to a rapidity gap between the jet edges of 1.5

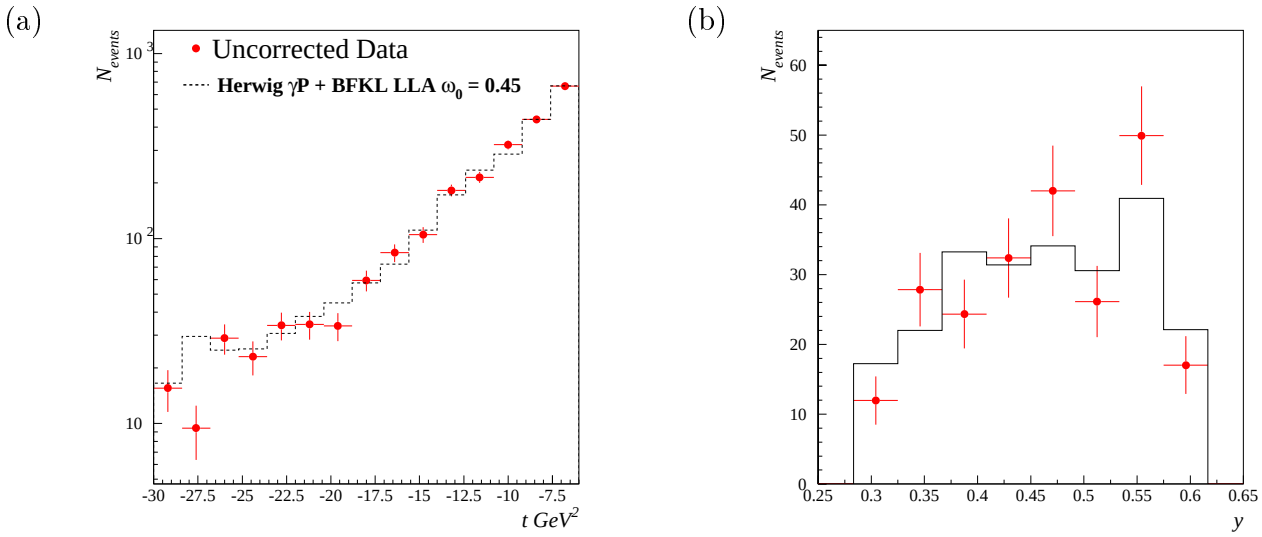

Figure 6.4: Comparison of the H1 data and HERWIG generator distributions for (a) t and (b) y

6.4.1 The HERWIG Generator Sample

The HERWIG generator, described in detail in chapter 5, was used to generate 23 pb^{-1} of BFKL LLA colour singlet exchange events, and 7 pb^{-1} of standard photoproduction events, which were combined according to the generated luminosities. This sample was then passed through a full simulation of the H1 detector, and is used in all subsequent plots. The BFKL sample was generated with $\alpha_s = 0.17$ (corresponding to $\omega_0 = 0.45$).

6.4.2 Comparison of Monte Carlo and Data

Figures 6.3 and 6.4 show the comparisons between the H1 data and HERWIG generator samples after detector simulation for the 4 kinematic variables used in the measurement. Also shown in figure 6.5 is the simulation of the position of the upper and lower edges of the rapidity gap. For each plot, the full set of analysis cuts detailed in table 6.1 is applied, other than the cut on the displayed variable. In each

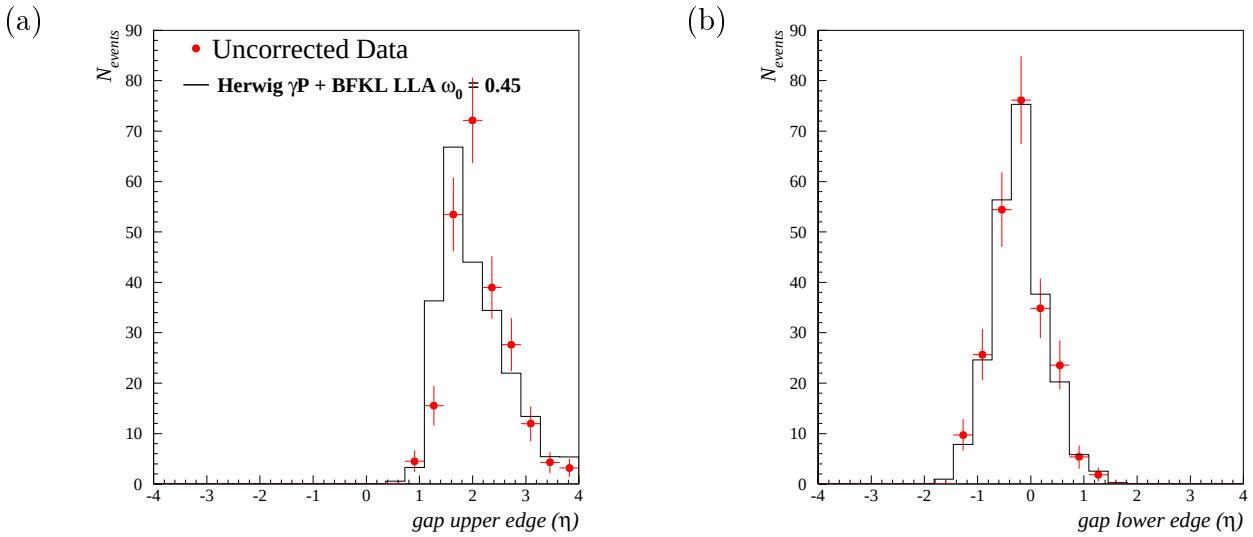

Figure 6.5: Comparison of the H1 data and HERWIG generator distributions for the upper (a) and lower (b) edges of the largest rapidity gap in the event as a function of η.

case, a good agreement is seen between data and Monte Carlo.

6.5 The Kinematic Range of the Cross Section

It is particularly important in the measurement of any cross section to define precisely what is being measured in terms of lorentz invariant quantities. This statement is particularly important in diffractive measurements, where it is often tempting to define event samples in terms of rapidity gaps. In this measurement the choice of the ranges of the four kinematic quantities $x_{I\!P}$, $y_{I\!P}$, t and W forces the presence of large rapidity gaps between the X and Y systems. This is shown graphically in figure 6.5. [3] The choice of the kinematic range of the cross section must therefore be a balance between the forcing of large rapidity gaps, and the range for each vari-

[3]The kinematics shown in figure 6.5 are of course calculated at the parton level, and ignore hadronisation effects

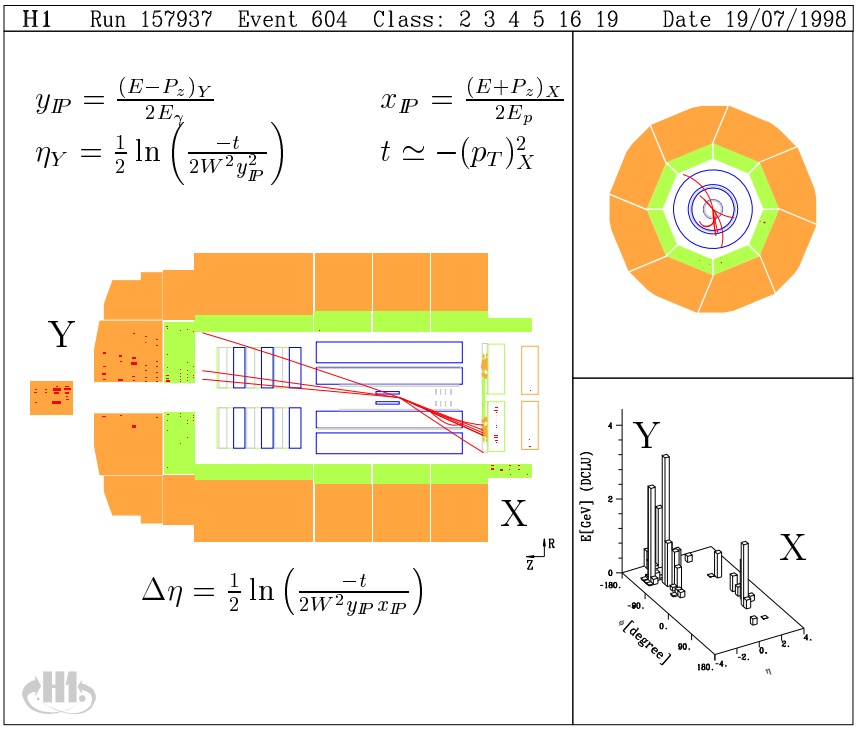

Figure 6.6: A typical double diffractive dissociation event. The proton dissociation system is labelled Y, and the photon dissociation system is labelled X. $\Delta\eta$ is the rapidity separation at the parton level between the struck parton from the proton (whose rapidity η_Y is also shown) and the struck parton from the photon.

able that can reliably be measured by the H1 detector. Each of the 4 quantities will be discussed in turn. The resolutions quoted are determined by comparing the HERWIG generator sample before and after the H1 detector simulation.

6.5.1 Measurement of t

The reconstruction of t proves to be the most problematic of the 4 kinematic variables. It is measured as the negative squared transverse momentum of the X system, $-(p_t)_X$, and is sensitive to losses down the backward beam pipe, particularly for low

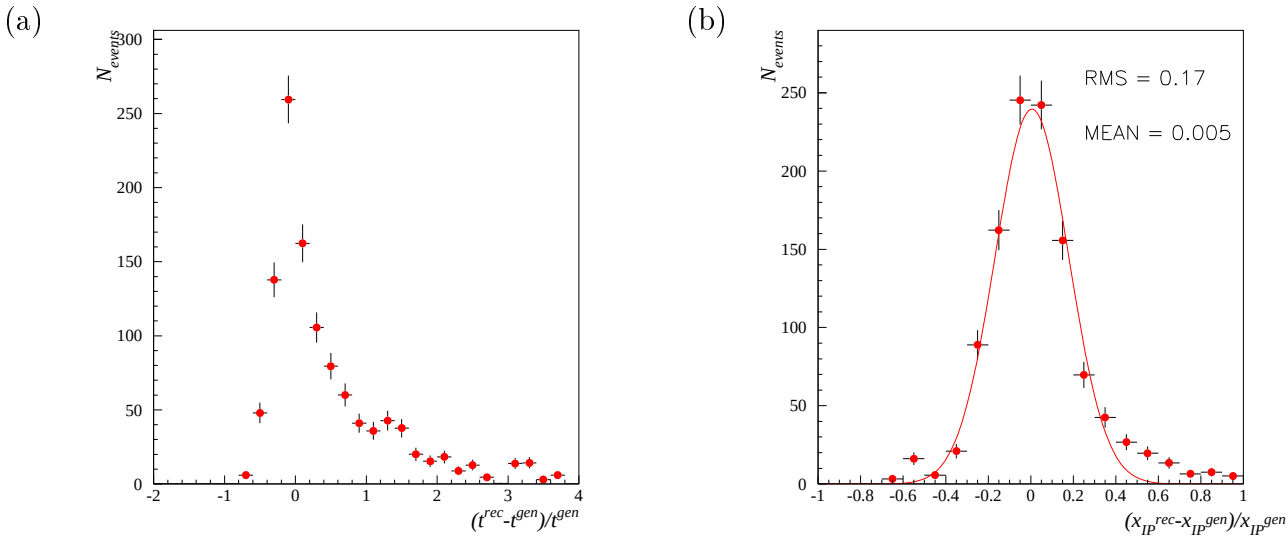

Figure 6.7: Fractional resolutions in t (shown after the +4 GeV^2 shift described in section 6.5.1) (a) and $x_{I\!P}$ (b)

values of $|t|$. The fractional resolution in t is shown in figure 6.7 (a). It was found necessary to apply a constant shift of +4 GeV^2 to the measured t value in order to centre this distribution on 0. This shift was applied to both the data and reconstructed Monte Carlo samples. Given the large tail in figure 6.7 (a), it is essential to be sure that that the large rapidity gap events in the sample have not migrated from very low $|t|$, i.e. the Regge region. For this reason, the cross section is measured for $|t| > 20$ GeV^2. The percentage of events which migrate into the sample from below $|t| = 20$ GeV^2 is found to be less than 30% in each bin of $x_{I\!P}$, and remains approximately constant from bin to bin.

6.5.2 Measurement of $y_{I\!P}$

The reconstruction method for $y_{I\!P}$ has been described in section 6.2. It is clear from figure 6.1 (b) that the $y_{I\!P}$ cut must be made in the range where it is possible to make an accurate measurement of $y_{I\!P}$, i.e. high $y_{I\!P}$. The ideal from the point of view of forcing a large rapidity gap, however, is to have $y_{I\!P}$ as low as possible. The choice of

the $y_{I\!P}$ range in which to measure the cross section is therefore a compromise; too low a cut will mean that large migrations across the $y_{I\!P}$ cut occur, and this will be reflected in low bin purities. These events are those in the bottom left quadrant of figure 6.1 (b). The best compromise was found to be to set the $y_{I\!P}$ cut at $y_{I\!P} < 0.018$, shown as the dashed lines in figure 6.1 (b).

6.5.3 Measurement of W

The γp centre of mass energy W is measured by the electron tagger as for the rapidity gaps between jets measurement (section 4.2.1). More care must be taken in the choice of W range in this case, however, since the measurement is more susceptible to non-collision background due to the different topology. In particular, electron beam-gas interactions can give rise to an X system and an electron in the tagger, and a large rapidity gap which will of course extend to the forward edge of the Liquid Argon Calorimeter. These events are characterised by low electron energies in the tagger, and for this reason the lower cut in y is set at $y = 0.3$, corresponding to $W_{\gamma P} = 165$ GeV. The upper y cut is set at $y = 0.6$, corresponding to $W_{\gamma P} = 233$ GeV to avoid the low acceptance region of the tagger. The electron tagger acceptance curve is shown in figure 4.3. A further cut is made on the local x-coordinate in the tagger of the centre of gravity of the electron cluster, $|x_{tag}| < 6.5$cm. This ensures that the electron shower is at least 1.5 cm from the edge of the detector, and is hence fully contained.

6.5.4 Measurement of $x_{I\!P}$

The reconstruction of $x_{I\!P}$ has been described in section 6.2. The resolution in $x_{I\!P}$ is $\sim 17\%$, as shown in figure 6.7 (b). This in fact proves not to be the limiting factor in the choice of the bin widths in the final result. Far more important is the lack of statistics for the determination of the trigger efficiency, to be described in section

6.3.2, which leads to larger $x_{I\!P}$ bins than experimental resolution would permit (see the discussion in section 6.10).

The choice of the $x_{I\!P}$ range of the measurement is more complicated. As previously discussed, the largest rapidity gap in an event is set (up to hadronisation effects) by the values of the 4 kinematic variables $x_{I\!P}$, $y_{I\!P}$, t and W. The t, W and $y_{I\!P}$ ranges have essentially been forced by detector effects, as described above. This leaves the $x_{I\!P}$ range to force the minimum rapidity gap size, and again detector effects play a role. For events with rapidity gaps smaller than ~ 1.5, the chance of incorrectly separating the X and Y systems, and hence reconstructing the wrong event kinematics, is greatly increased. This is reflected in lower bin purities and larger acceptance corrections. The sample is therefore restricted to events with rapidity gaps > 1.5. It must be emphasised, however, that this is NOT part of the hadron level cross section definition. That is to say, the cut is made only on the data sample and will be accounted for in the smeared acceptance. The choice of the upper bound in the $x_{I\!P}$ range is therefore forced by this gap size requirement to be $x_{I\!P} < 4 \times 10^{-3}$. The lower bound is set by the kinematic limit $x_{I\!P} > -t/W^2$. In fact, detector acceptance falls rapidly at very low M_X, and hence the lower bound is set somewhat higher, at $x_{I\!P} > 7 \times 10^{-4}$. Two typical events are shown in figures 6.5 and 6.8. In the event shown in Figure 6.5, most of the forward or Y system has been lost down the beam pipe, as is evident from the 'lego' plot. This is the type of event which would have been lost in the dijet approach. In Figure 6.8, there is much more forward activity, although the rapidity gap between the two systems is still strikingly visible.

The complete set of analysis cuts is shown in table 6.1.

$0.3 < y < 0.6$
$E_{tagger} > 6$ GeV
$E_{pd} < 2$ GeV
$\|x_{tag}\| < 6.5$ cm
-25 cm $< zvtx < 35$ cm
1 vertex-linked track
$7 \times 10^{-4} < x_{I\!P} < 4 \times 10^{-3}$
$y_{I\!P} < 0.018$
$\|t\| > 20$ GeV^2
$\|\eta_X - \eta_Y\| > 1.5$
40 GeV $< \sum(E - P_z) + 2E_{tagger} < 70$ GeV

Table 6.1: The complete set of kinematic and background rejection cuts used in the double dissociation analysis

6.6 Sources of Background

As has already been mentioned in section 6.5, non-collision background is a problem in this measurement. The standard background rejection cuts are applied as for the rapidity gaps between jets measurement. 40 GeV $< \sum(E - P_z) + 2E_{tagger} < 80$ GeV reduces beam halo contamination, and a good z-vertex is required with at least one track linked to the vertex, reducing the beam-gas contamination. Given the small number of events in the sample, however, every event was scanned visually for other possible backgrounds. 7 events were rejected by this visual search. These events comprised background of 4 different types. An example of each is shown in figures 6.9, 6.10, 6.11 and 6.12. Figure 6.9 is a cosmic ray muon, which has travelled vertically through the detector, in coincidence with a good photoproduction event. Figure 6.10 is a beam halo muon which has escaped the anti-background cuts. It's path through the lower half of the Liquid Argon calorimeter is clearly visible. Figure

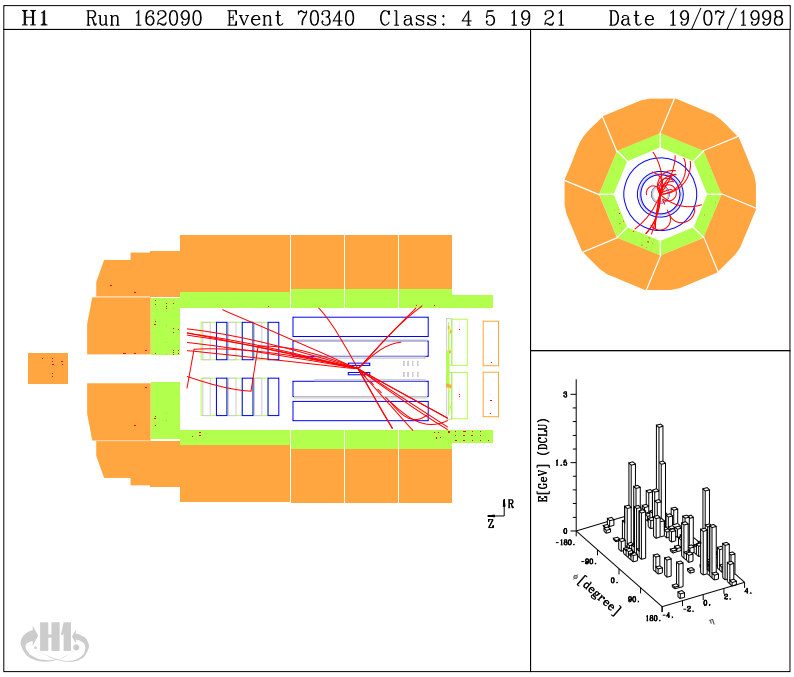

Figure 6.8: An event from the final sample

6.11 is a QED Compton event. Figure 6.12 is a coherent noise event, where one region of the electromagnetic section of the Liquid Argon calorimeter has fired due to a readout problem.

6.7 Evaluation of the Cross Section $\frac{\mathrm{d}\sigma}{\mathrm{d}x_{I\!P}}(\gamma p \to XY)$

The cross section $\frac{\mathrm{d}\sigma}{\mathrm{d}x_{I\!P}}(ep \to XY)$ is extracted in four bins of $x_{I\!P}$ using

$$\frac{\mathrm{d}\sigma}{\mathrm{d}x_{I\!P}}(ep \to XY) = \frac{\mathcal{N}}{A\mathcal{L}b\epsilon} \tag{6.6}$$

where $\mathcal{N}$ is the number of events passing the analysis cuts in the bin, A is the smeared acceptance, $\mathcal{L}$ is the integrated luminosity of the measurement, b is the bin width in $x_{I\!P}$ and ϵ is the trigger efficiency. In order to convert this ep cross section to a γp cross section, the flux of quasi-real photons is estimated using the

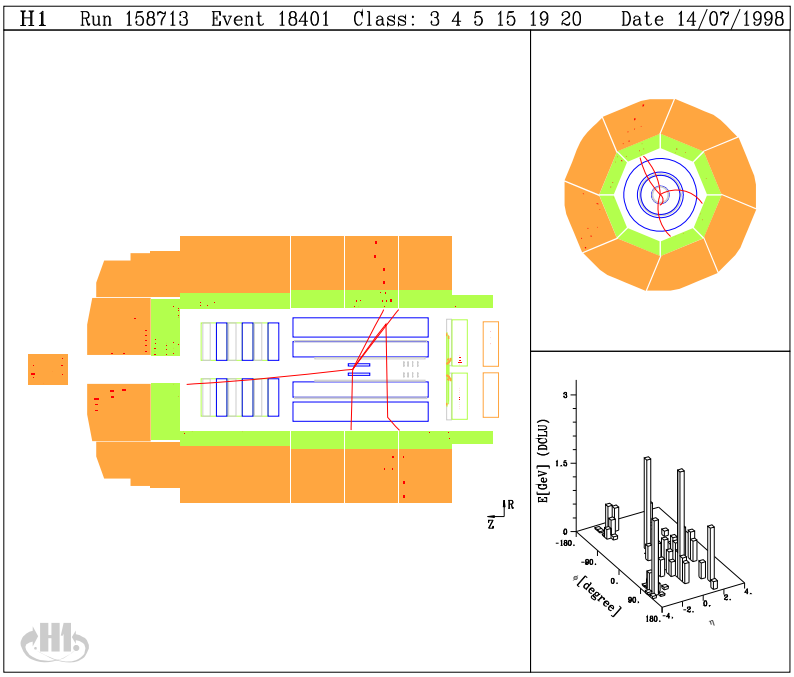

Figure 6.9: A cosmic ray muon event

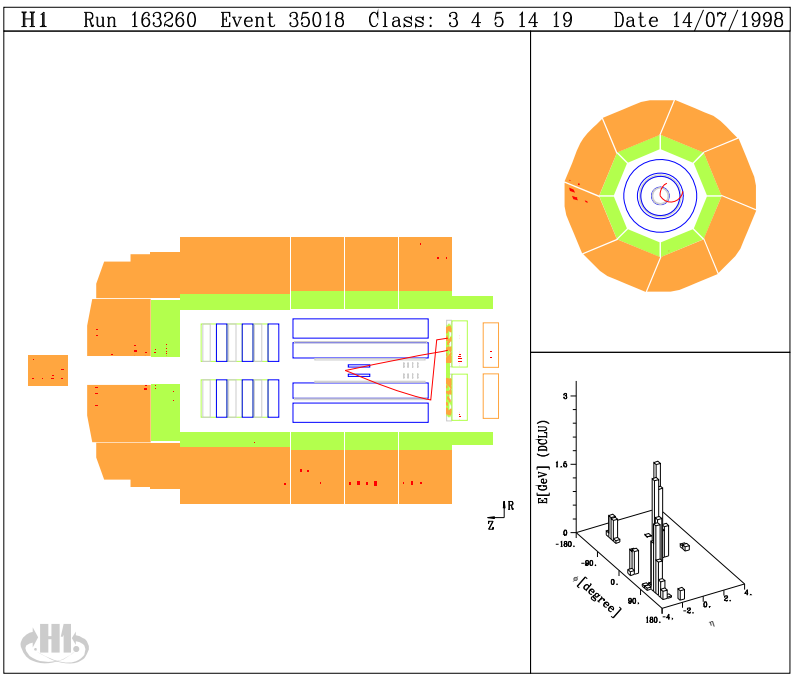

Figure 6.10: A beam halo muon event

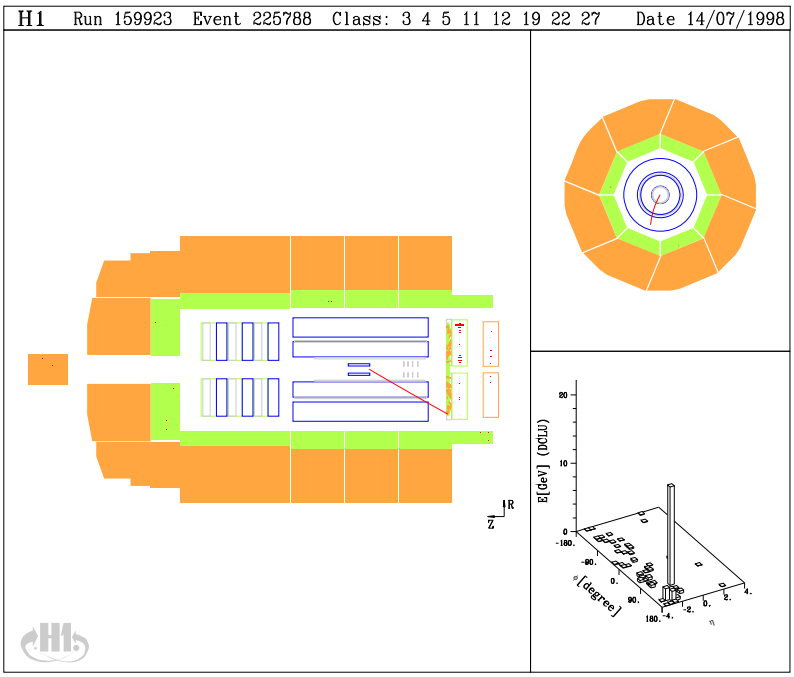

Figure 6.11: A QED Compton event

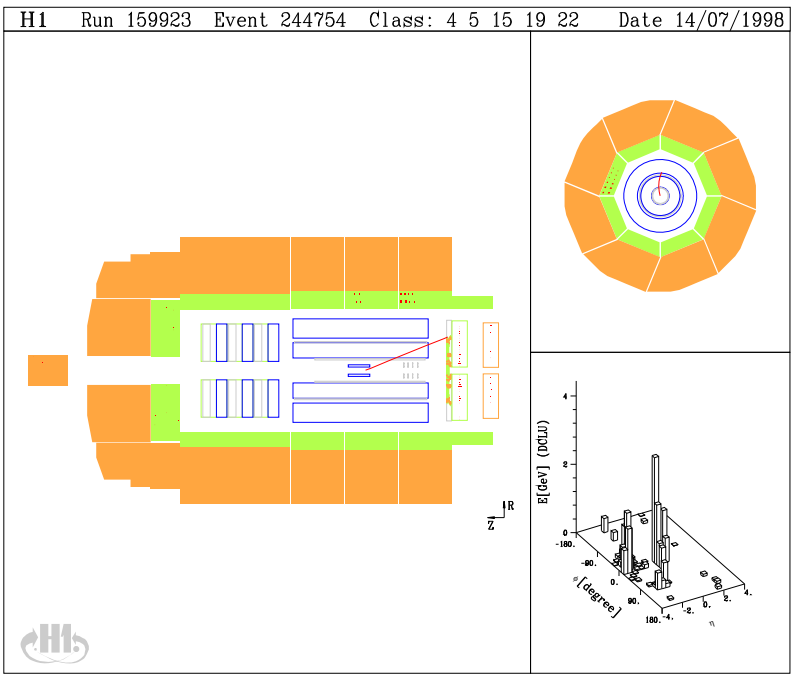

Figure 6.12: A coherent noise event

Weizsacker-Williams approximation [34] as described in section 3.6;

$$\frac{\mathrm{d}^2\sigma_{ep}(s)}{\mathrm{d}Q^2\mathrm{d}y} = \sigma_{\gamma p}(ys)F(y,Q^2) \tag{6.7}$$

The photon flux is given by

$$F(y,Q^2) = \frac{\alpha_e m}{2\pi Q^2}\left(\frac{1+(1-y)^2}{y} - \frac{2(1-y)}{y}\frac{Q^2_{min}}{Q^2}\right) \tag{6.8}$$

where

$$Q^2_{min} = \frac{(m_e y)^2}{(1-y)} \tag{6.9}$$

In the measured range $0.3 < y < 0.6$, the resulting flux, integrated over y and Q^2 is found to be

$$f = \int F(y,Q^2)\mathrm{dydQ}^2 = 9.66 \times 10^{-3} \tag{6.10}$$

6.7.1 Evaluation of the Trigger Efficiency

As described in section 6.3.2, two independent subtriggers were used to collect the data sample used in this analysis. The efficiency of each trigger was evaluated separately, by using the other trigger as a reference. This procedure is possible because the two triggers are independent of each other; the probability for the track trigger to fire is not correlated with the probability for the spacal trigger to fire. [4] The procedure can be visualised as shown in figure 6.13. The efficiency of the track trigger is given by the number of events in which it fired in coincidence with the spacal trigger, divided by the number of events in which only the spacal trigger fired, and vice-versa for the efficiency of the spacal trigger. That is;

$$\epsilon_{\mathrm{track}} = \frac{c}{b+c} \tag{6.11}$$

$$\epsilon_{\mathrm{spacal}} = \frac{c}{a+c} \tag{6.12}$$

[4] Of course both triggers also have the electron tagger requirement; this efficiency is included in the acceptance corrections for the tagger

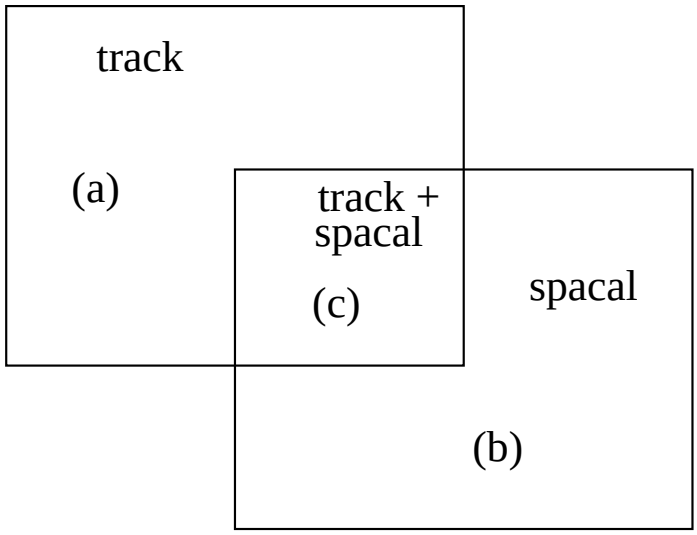

Figure 6.13: The trigger efficiency calculation

Then the efficiency for the combination of both triggers is

$$\epsilon = 1 - (1 - \epsilon_{\text{track}})(1 - \epsilon_{\text{spacal}}) \tag{6.13}$$

The individual trigger efficiencies for the track and spacal triggers are shown in figures 6.14 (a) and (b) respectively. The track trigger is less efficient at low $x_{I\!P}$, that is for events with the largest rapidity gaps. This is to be expected, since both the z-vertex and $DCRPh$ trigger elements rely on activity in the central tracking detectors, and are not as effective when there is little activity in the central rapidity region. The spacal trigger should not be affected by the size of the rapidity gap, since it relies only on activity in the far backward region. The spacal trigger efficiency is indeed flat across the measured $x_{I\!P}$ range, although much lower than the track trigger in all bins. The combined trigger efficiency is shown in figure 6.15. The error bars shown on the combined efficiency are those propagated through to the final systematic error on the cross section, described in section 6.8. They are large because of the small number of events in the sample, particularly in region c of figure 6.13, that is the events in which both triggers fired. This error is in fact the dominant systematic error in the measurement. It will of course be improved in the

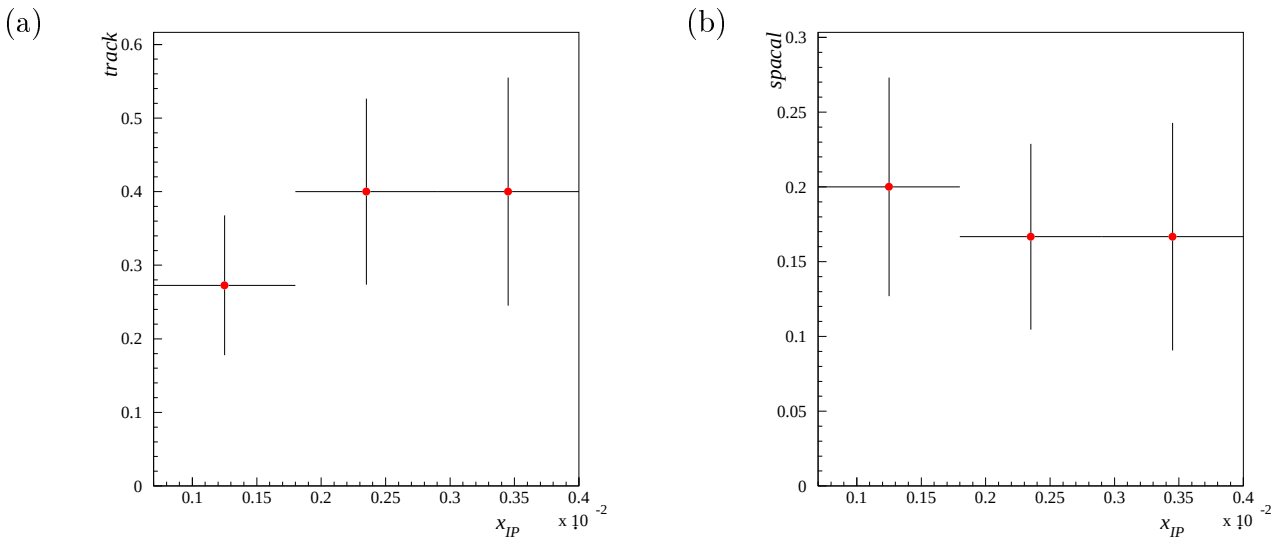

Figure 6.14: The trigger efficiency for the track trigger (a) and spacal trigger (b)

future with higher luminosities, and by the design of triggers optimised to this type of measurement. [5] The error on the combined trigger efficiency was estimated by

$$\sigma^2(\epsilon) = \left(\frac{\partial\epsilon}{\partial a}\right)^2 \sigma^2(a) + \left(\frac{\partial\epsilon}{\partial b}\right)^2 \sigma^2(b) + \left(\frac{\partial\epsilon}{\partial c}\right)^2 \sigma^2(c) \tag{6.14}$$

where in general

$$\sigma^2(a,b,c) = \sum_i W_i^2 \tag{6.15}$$

and W_i is the weight of event i, and the sum runs over all events in samples a,b and c. Of course in the case of the data sample, each event has a weight of 1, but this general formula may also be used for the Monte Carlo sample, when events can carry different weights.

6.7.2 The Smeared Acceptance

As described in section 4.4, the data are corrected for detector acceptance and resolution effects using the Monte Carlo event sample. The smeared acceptance A

[5] Since this measurement is the first of its kind, the triggering at H1 was not optimised during the 1996 running period for this unusual event topology. This will be improved in future years

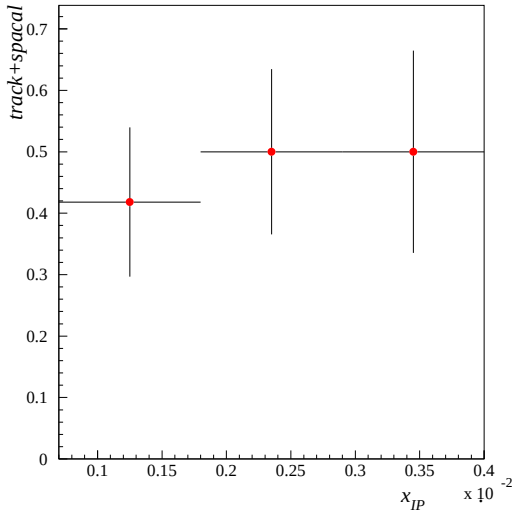

Figure 6.15: The combined trigger efficiency

is shown in figure 6.16 (a). The errors on the acceptance are estimated as for the rapidity gaps between jets analysis (section 4.4).

The bin purities are shown in 6.16 (b). An interesting comparison between the purities in this analysis and those in the gaps between jets analysis (figure 4.11 (a)) should be made here. In the gaps between jets case, the 'important' bin, that is the bin which corresponds to the largest rapidity gaps, has the lowest purities, because of the difficulties in jet finding at the edges of the calorimeters. In this case, large rapidity gaps correspond to low $x_{I\!P}$, that is the bins with the highest purities. The reason is that this measurement relies on the accurate separation of the X and Y systems, and this is most successfully achieved for events which have the largest rapidity gaps, that is lowest $x_{I\!P}$.

6.8 Evaluation of Errors

The largest contribution to the statistical error on each measured point comes from the limited number of events in the sample. A further small contribution from

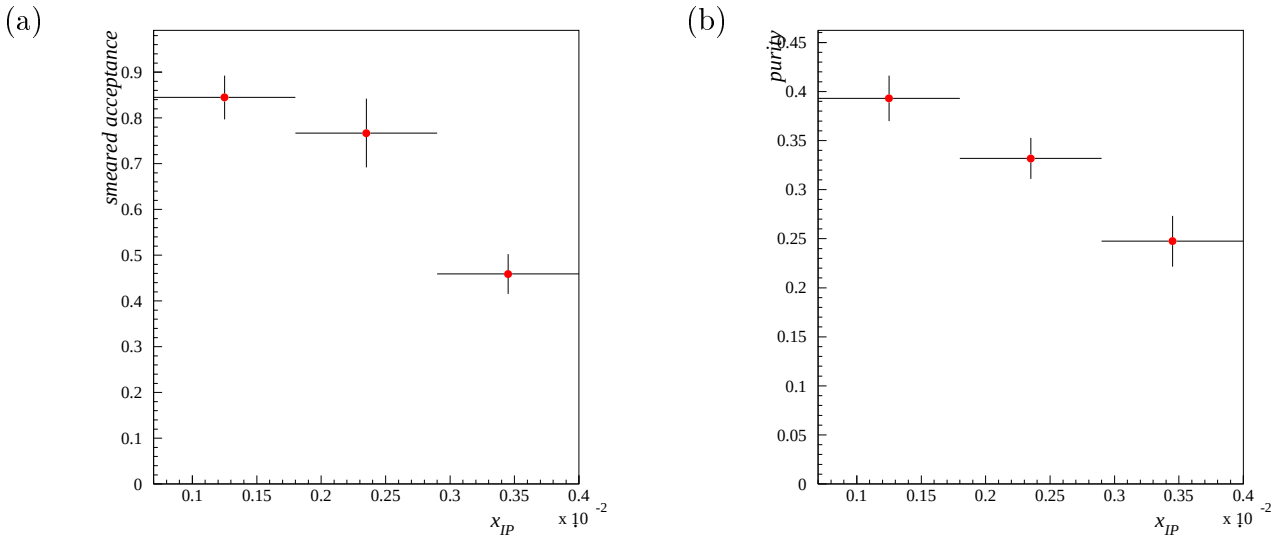

Figure 6.16: The smeared acceptance (a) and bin purity (b)

the statistical error on the acceptance corrections, $\sigma(A)$ estimated in section 6.7.2, is included. The total statistical error on the cross section can be written (from equation 6.6)

$$\sigma^2 = \left(\frac{1}{A\mathcal{L}b}\right)^2 \sigma^2(N) + \left(\frac{N}{-A^2\mathcal{L}b}\right)^2 \sigma^2(A) \tag{6.16}$$

Systematic errors are estimated on a bin by bin basis. The first group of errors originate from the uncertainty in the energy scales of the detectors. They are estimated by varying the energy scale by the known uncertainty and recalculating the acceptance corrections from Monte Carlo. The percentage change in the acceptance correction to each bin is then the systematic error in that bin. This Monte Carlo based procedure is used because of the far better statistics available in the Monte Carlo sample than in the data. The uncertainties in the relevant detectors are:

- Liquid Argon Calorimeter Energy Scale

  The hadronic energy scale of the LAr Calorimeter is known to 4%

- SPACAL Calorimeter Energy Scale

  The hadronic energy scale of the SPACAL Calorimeter is known to 7%

- Uncertainty on Track Measurements The momentum scale of the track measurements is varied by 3%

- Acceptance of the Electron Tagger

  A figure of 5% is assumed for the systematic error on the acceptance of the electron tagger in the measured y range.

- Luminosity Measurement

  The Luminosity of the 1996 data is known to 2%

The largest systematic uncertainties come from two sources. Already discussed in section 6.7.1 is the large uncertainty in the determination of the trigger efficiency. The other large uncertainty comes form the Monte Carlo model dependence of the acceptance corrections, particularly since HERWIG is at present the only generator which incorporates the BFKL colour singlet exchange model. The errors were estimated by reweighting the Monte Carlo t distribution by the factors $e^{\pm 0.04t}$.

6.9 The Differential Cross Section $\frac{\mathrm{d}\sigma}{\mathrm{d}x_{I\!P}}(\gamma p \to XY)$

The cross section $\frac{\mathrm{d}\sigma}{\mathrm{d}x_{I\!P}}$, corrected for detector effects, is shown in figure 6.17. The inner error bars are statistical and the outer error bars are the quadratic sum of the statistical and systematic errors. The solid line is the prediction from the HERWIG generator for all non-singlet exchange photoproduction processes. A significant excess above the expectation from the standard photoproduction model is observed. The dashed line shows the HERWIG prediction with the LLA BFKL prediction added. Good agreement is observed in both normalisation and shape. Care must be taken, however, in the interpretation of this result. There is a large theoretical uncertainty in the overall normalisation of the LLA BFKL cross section prediction shown in equation (5.3). The agreement in normalisation may well therefore be fortuitous. It should also be noted that the shape of the $x_{I\!P}$ distribution in this

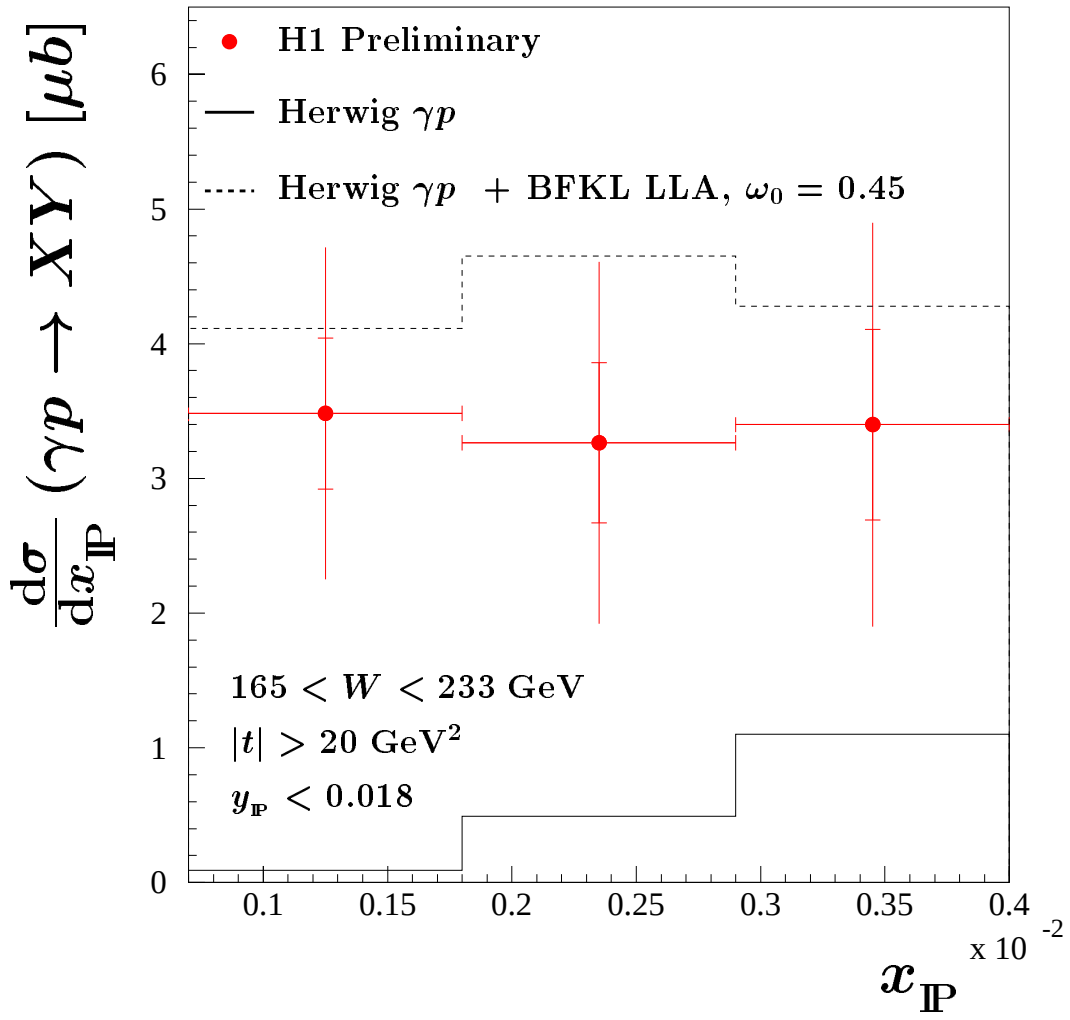

Figure 6.17: The Differential cross section $\frac{d\sigma}{dx_{I\!P}}$

region of phase space is not only determined by the underlying dynamics of the interaction, but also by kinematic effects. There is a kinematic limit on the lowest possible value of $x_{I\!P}$, set by the requirement that $|t| > 20\text{GeV}^2$ and $165 < W < 233$ GeV, of $x_{I\!P} \simeq 7 \times 10^{-4}$ (see equation (6.1)). This forces the cross section down in the lowest $x_{I\!P}$ bin. The good agreement in shape with the BFKL Monte Carlo prediction, however, implies that the data are consistent with a value of $\omega_0 \simeq 0.45$ within this model.

6.10 The Outlook for the Future

Despite the limitations discussed in the previous section, the outlook for the future is promising. This measurement has demonstrated that it is possible to greatly increase the reach in rapidity allowed by the gaps between jets approach at HERA. With the higher luminosity already on tape from the 1997 running period and improved triggering, a much more precise measurement of the double diffraction dissociation cross section will be possible. This will lead to a precise determination of the energy dependence of the process, allowing much more rigorous tests of the theory of diffraction in the perturbative region.

Chapter 7

Summary

The two analyses presented in chapters 4 and 6 clearly show an excess of events with large rapidity gaps at high momentum transfer over the expectation from standard photoproduction processes. It is argued that these events cannot be explained by pure Regge phenomenology unless α' for the hard pomeron is very close to zero. The fraction of dijet events with rapidity gaps between the jets is larger in γp collisions at HERA than in pp collisions at the TEVATRON. This breakdown in diffractive factorisation may be interpreted as the result of a gap destruction mechanism, dependent on the total centre of mass energy in the collision and possibly the structure of the beam particles themselves.

The differential cross section $\frac{\mathrm{d}\sigma}{\mathrm{d}x_{I\!P}}(\gamma p \to XY)$ has been measured in the kinematic range $165 < W < 233$ GeV, $|t| > 20$ GeV^2, $y_{I\!P} < 0.018$ and $7 \times 10^{-4} < x_{I\!P} < 4 \times 10^{-3}$. A pQCD model for colour singlet exchange calculated within the leading logarithmic approximation of BFKL provides a good description of the data in both normalisation and shape. Conclusions are, however, difficult to draw, due to the large uncertainties in the BFKL formalism. The process has a steep energy dependence, equivalent to $\omega_0 = 0.45$ within the BFKL formalism.

Future measurements with improved statistics and triggering within the frame-

work developed in this thesis will allow a very precise determination of the energy dependence of the diffractive process at large momentum transfer, and may help in the understanding of the breakdown of diffractive factorisation between HERA and the TEVATRON.

Appendix A

Jet Finding

The choice of jet finding algorithm in an analysis depends very much on the purpose of the analysis. In the case of rapidity gaps between jets, the jets are required primarily to reflect the rapidity of the outgoing partons from the hard scatter, and to provide some position in η from which to define a rapidity gap. For this purpose, the simple geometric properties of a cone-type algorithm are preferable to the more complicated, if theoretically more desirable properties of cluster type algorithms. (For a detailed review see, for example [65]).

The algorithm used in this analysis is the CDF cone algorithm [43]. Each calorimeter cluster in the event is taken in turn as the 'seed' direction, beginning with the highest E_T cluster in the event. Each cluster i which lies within radius R in the $\eta - \phi$ plane of the seed cluster, where

$$R^2 \leq (\eta_i - \eta_s)^2 + (\phi_i - \phi_s)^2 \tag{A.1}$$

is used to calculate a jet transverse energy and direction;

$$E_{TJ} = \sum_i E_{Ti} \tag{A.2}$$

$$\eta_i = \frac{1}{E_{TJ}} \sum_i E_{Ti}\eta_i \tag{A.3}$$

$$\phi_J = \frac{1}{E_{TJ}} \sum_i E_{Ti}\phi_i \tag{A.4}$$

If the jet and seed directions are not equal, then the jet direction is defined to be the seed direction, and the process is repeated. If, after this iteration process, the jet is not the same as any already found, then it is defined to be a 'protojet'. The midpoint of every pair of protojets is taken as a seed direction, and the iteration process is repeated again. Every protojet which has more than 75% of its E_T contained within a higher E_T protojet is then deleted. Finally, all clusters which lie in more than one protojet are assigned to the jet whose centre is nearest in η and ϕ, and the jet transverse energy and direction are recalculated using equations (A.2) to (A.4). The remaining protojets are then called jets.

Bibliography

[1] B. E. Cox and J. R. Forshaw, Phys. Lett. **B434** (1998) 133-140.

[2] H1 Collaboration; I. Abt et al., Nucl. Instr. and Meth. **A386** (1997) 310-348.

[3] H1 Calorimeter Group; B. Andrieu et al., Nucl. Instr. and Meth. **A336** (1993) 460.

[4] H. Wellisch, J. Kubenka, H. Oberlack, P.Schacht, Hadronic Calibration of the H1 LAr Calorimeter using Software Weighting Techniques, **H1-02/94-346** (1994).

[5] H1 SPACAL group, R.D. Appuhn et al., Nucl. Instr. and Meth. **A386** (1997) 397.

[6] S. Burke et al., RAL **95-037**. DESY **95-132**

[7] J. Burger et al., NIM. **A279** (1989) 217.

[8] S. Egli et al., NIM. **A283** (1989) 487.

[9] K. Muller et al., NIM. **A312** (1992) 457.

[10] H. Bethe, W. Heitler, Proc. Roy. Soc. **A146** (1934) 83.

[11] J. Heatherington et al., Studies on TOF FTDC data. H1 Internal Note **93-307**
J. Heatherington et al., Analysis of TOF FTDC data. H1 Internal Note **94-362**

[12] H. Cronstrom et al., NIM. **A340** (1990) 304.

[13] H1 Collaboration: C.Adloff et al., Z.Phys. **C74** (1997) 221.

[14] E. Elsen, The H1 Trigger and Data Acquisition. Proc. of the International Symposium on Electronic Instrumentation in Physics, Dubna, May 1991. H1 Internal Note **93-262**

F. Sefkow et al., Experience with the First Level Trigger of H1. Proc. of the 1994 IEEE Nuclear Science Symposium, Norfolk, Virginia. H1 Internal Note **94-407**

[15] P. D. B. Collins, Introduction to Regge Theory and High Energy Physics, Cambridge University Press (1977)

[16] A. Donnachie and P. V. Landshoff, hep-ph/9806344v2.

[17] Cutkosky, R.E. J. Math. Phys. **1**, (1960) 429.

[18] A. Sommerfeld, Partial Differential Equations in Physics, Academic Press (1949).

G. N. Watson, Proc. Roy. Soc **95** (1918) 83.

[19] J.R. Forshaw and D. A. Ross, Quantum Chromodynamics and the Pomeron, Cambridge University Press (1997).

[20] G. F. P. Chew and S. C. Frautschi, Phys. Rev. Lett. **7** (1961) 394.

G. F. P. Chew and S. C. Frautschi, Phys. Rev. Lett. **8** (1962) 41.

[21] A. V. Barnes et al. Phys. Rev. Lett. **37** (1976) 76.

[22] L. B. Okun and I. Y. Pomeranchuk, Sov. Phys. JETP **3** (1956) 307.

I. Y. Pomeranchuk, Sov. Phys. **3** (1956) 306

[23] L. F. Foldy and R. F. Peierls, Phys. Rev. **130** (1963) 1585.

[24] I. Y. Pomeranchuk, Sov. Phys. **7** (1958) 499.

[25] A. Donnachie and P. V. Landshoff, Phys. Lett. **B296** (1992) 227.

[26] H1 Collaboration, Nucl. Phys. **439** (1995) 471.

[27] C. Callen and D. Gross, Phys. Rev. Lett. **21** (1968) 311.

[28] V. Gribov et al., Sov. J. Nucl. Phys. **15** (1972) 438.
G. Alterelli, G. Parisi, Nucl. Phys. **B126** (1977) 298.

[29] E.A.Kuraev, L.N.Lipatov and V.S.Fadin, Sov.Phys.JETP **45** (1977) 199.
Ya.Ya.Balitsky and L.N.Lipatov, Sov.J.Nucl.Phys **28** (1978) 822.
L.N.Lipatov, Sov.Phys.JETP **63** (1986) 904.

[30] L.N.Lipatov and V.S.Fadin, Sov.J.Nucl.Phys. **50** (1989) 712; JETP Lett. **89** (1989) 352.
V.S.Fadin and R.Fiore, Phys.Lett. **B294** (1992) 286.
V.S.Fadin and L.N.Lipatov, Nucl.Phys. **B406** (1993) 259; **B477** (1996) 767; hep-ph/9802290.
V.S.Fadin, R.Fiore and A.Quartarolo, Phys.Rev. **D50** (1994) 2265; **D50** (1994) 5893; **D53** (1996) 2729.
V.S.Fadin, R.Fiore and M.I.Kotsky, Phys.Lett. **B387** (1996) 593; Phys.Lett. **B359** (1995) 181.
V.S.Fadin, M.I.Kotsky and L.N.Lipatov, hep-ph/9704267.
V.S.Fadin et al., hep-ph/9711427.
G.Camici and M.Ciafaloni, Phys.Lett. **B386** (1996) 341; Nucl.Phys. **B496** (1997) 305.
M.Ciafaloni and G.Camici, Phys.Lett. **B412** (1997) 396 and erratum; hep-ph/9803389.

[31] ZEUS Collaboration, Phys. Lett. **B315** (1993) 481.
H1 Collaboration, Nucl. Phys. **B429** (1994) 377.

[32] ZEUS Collaboration: M. Derrick et al., Z. Phys. **C70** (1996) 391.
ZEUS Collaboration, hep-ex/9807010.

[33] A. Donnachie and P. V. Landshoff, hep-ph/9806344v2.

[34] C. Weizsacker, Z. Phys. **88** (1934) 612.
E. Williams, Phys. Rev. **45** (1934) 729.

[35] H1 Collaboration, Z. Phys. **C69** (1995) 27.

[36] J. J. Sakurai, Ann. Phys. **11** (1960) 1.
J. J. Sakurai and D. Schildknecht, Phys. Lett. **B40** (1972) 121.
M. Greko, Nucl. Phys. **B63** (1973) 398.

[37] M. L. Good and W. D. Walker, Phys. Rev. **120** (1960) 1857.

[38] For a review see ref [19] Chapter 8.

[39] H1 Collaboration, "Elastic Electroproduction of ρ Mesons for $1 < Q^2 < 60\text{GeV}^2$ at HERA", contribution to The 29th International Conference on High-Energy Physics ICHEP98, Vancouver, Canada, July 1998.

[40] B. E. Cox "Experimental Results on Small-x Physics and Diffraction", Proceedings from Workshop on HERA Physics, Durham, England, September 1998, to be published in J. Phys. G.

[41] J.R.Forshaw and P.J.Sutton, Eur.Phys.J. **C1** (1998) 285.

[42] A.H.Mueller and W.-K.Tang, Phys.Lett. **B284** (1992) 123.

[43] CDF Collaboration, F. Abe et al., Phys. Rev. **D45** 1448 (1992).

[44] G.Marchesini et al., Comp.Phys.Comm. **67** (1992) 465.

[45] M.E.Hayes, Bristol University, PhD Thesis (1998).

[46] H1 Collaboration, Z. Phys **C70** (1996), 17.

[47] H1 Collaboration, Phys. Lett. **B415** (1997) 418.

[48] M. Glück, E. Reya, A. Vogt, Z. Phys. **C67** (1995) 433.

[49] J.M.Butterworth, J.R.Forshaw and M.H.Seymour, Z.Phys. **C72** (1996) 637.

[50] J. M. Butterworth et. al. hep-ph/9609227

[51] ZEUS Collaboration: M.Derrick et al., Phys.Lett. **B369** (1996) 55.
H1 Collaboration: "Rapidity Gaps Between Jets in Photoproduction at HERA" contribution to The International Europhysics Conference on High Energy Physics, August 1997, Jerusalem, Israel.

[52] D0 Collaboration: S.Abachi et al., Phys.Rev.Lett. **72** (1994) 2332; Phys.Rev.Lett. **76** (1996) 734.
CDF Collaboration: F.Abe et al., Phys.Rev.Lett. **74** (1995) 855.

[53] K.Borras, for the CDF Collaboration, CDF/PUB/JET/PUBLIC/4590.
D0 Collaboration, hep-ex/9809016

[54] L. Alvero, J. C. Collins and J. J. Whitmore, hep-ph/9806340.

[55] E. Gotsman, E. Levin and U. Maor, hep-ph/9804404.

[56] I.F.Ginzberg, S.L.Panfil and V.G.Serbo, Nucl.Phys. **B284** (1987) 685.
J.R.Forshaw and M.G.Ryskin, Z.Phys. **C68** (1995) 137.
J.Bartels, J.R.Forshaw, M.Wüsthoff and H.Lotter, Phys.Lett. **B375** (1996) 301.
D.Yu.Ivanov, Phys.Rev. **D53** (1996) 3564.
I.F.Ginzburg and D.Yu.Ivanov, Phys.Rev. **D54** (1996) 5523.

[57] H1 Collaboration: "Production of J/ψ Mesons with large $|t|$ at HERA" contribution to The International Europhysics Conference on High Energy Physics, August 1997, Jerusalem, Israel.

ZEUS Collaboration: "Study of Vector Meson Production at Large $|t|$ at HERA" contribution to The International Europhysics Conference on High Energy Physics, August 1997, Jerusalem, Israel.

[58] M.Glück, E.Reya and A.Vogt, Phys.Rev. **D45** (1992) 3986.

[59] M.Glück, E.Reya and A.Vogt, Z.Phys. **C67** (1995) 433.

[60] H.Plothow-Besch: PDFLIB Users Manual, W5051 PDFLIB, 1997.07.02, CERN-PPE; Int.J.Mod.Phys. **A10** (1995) 2901.

[61] H.Abramowicz, K.Charchula and A.Levy, Phys.Lett. **B269** (1991) 458.

[62] P.Aurenche, M.Fontannaz and J.Ph.Guillet, Z.Phys. **C64** (1994) 621.

[63] L.E.Gordon and J.K.Storrow, Nucl.Phys. **B489** (1997) 405.

[64] E.Gotsman, E.Levin and U.Maor, TAUP 2485-98, hep-ph/9804404.

[65] M. H. Seymore "Jet Phenomenology", Proceedings of Les Rencontres de la Vallee d'Aoste, La Thuile, Italy, March 1997.

Acknowledgements

This thesis would not have been possible without the contributions and support of many people.

First and foremost, I would like to thank my supervisor Robin Marshall. I would certainly not have achieved what I have without his help, support, encouragement and friendship during my time at Manchester. I would also like to thank Jeff Forshaw for sharing his wonderful view of physics with me. I enjoyed immensely our collaboration on the work in chapter 5 of this thesis, and look forward to more of the same in the future.

My time in Hamburg would not have been so profitable (and so much fun) without Paul Bate (Othmarschen Bar), Chris Hilton, Mike McAndrew, Andy Mehta, Dave Milstead (Vodka), Paul Newman, Julian Phillips (Fine Wine), Eram Rizvi, Mark Smith (*?@!), Paul Sutton, Paul Thompson, Ben Waugh, Rob Waugh and countless others. I can't list them all!

Thanks also to Keith Stephens for helping me with all that detector stuff, Martin McDermott for many discussions, Andy Walkden and Simon Bird for spending 6 years at Manchester with me, Duncan Brown and all in the Manchester HEP group.

Finally, I'd like to thank T.J. for putting up with a very long distance relationship, and of course my family and friends in Oldham for subsidising my eccentric career choices all these years.